

Advanced Nuclear Technology: Integrated Pressurized Water Reactor (iPWR) Containment Aerosol Deposition Behavior

Phase 2b: Results and Analysis

2018 TECHNICAL REPORT

Advanced Nuclear Technology: Integrated Pressurized Water Reactor (iPWR) Containment Aerosol Deposition Behavior

Phase 2b: Results and Analysis

3002013032

Final Report, March 2018

EPRI Project Manager
R. King

All or a portion of the requirements of the EPRI Nuclear
Quality Assurance Program apply to this product.

YES



ELECTRIC POWER RESEARCH INSTITUTE

3420 Hillview Avenue, Palo Alto, California 94304-1338 • PO Box 10412, Palo Alto, California 94303-0813 • USA
800.313.3774 • 650.855.2121 • askepri@epri.com • www.epri.com

DISCLAIMER OF WARRANTIES AND LIMITATION OF LIABILITIES

THIS DOCUMENT WAS PREPARED BY THE ORGANIZATION(S) NAMED BELOW AS AN ACCOUNT OF WORK SPONSORED OR COSPONSORED BY THE ELECTRIC POWER RESEARCH INSTITUTE, INC. (EPRI). NEITHER EPRI, ANY MEMBER OF EPRI, ANY COSPONSOR, THE ORGANIZATION(S) BELOW, NOR ANY PERSON ACTING ON BEHALF OF ANY OF THEM:

(A) MAKES ANY WARRANTY OR REPRESENTATION WHATSOEVER, EXPRESS OR IMPLIED, (I) WITH RESPECT TO THE USE OF ANY INFORMATION, APPARATUS, METHOD, PROCESS, OR SIMILAR ITEM DISCLOSED IN THIS DOCUMENT, INCLUDING MERCHANTABILITY AND FITNESS FOR A PARTICULAR PURPOSE, OR (II) THAT SUCH USE DOES NOT INFRINGE ON OR INTERFERE WITH PRIVATELY OWNED RIGHTS, INCLUDING ANY PARTY'S INTELLECTUAL PROPERTY, OR (III) THAT THIS DOCUMENT IS SUITABLE TO ANY PARTICULAR USER'S CIRCUMSTANCE; OR

(B) ASSUMES RESPONSIBILITY FOR ANY DAMAGES OR OTHER LIABILITY WHATSOEVER (INCLUDING ANY CONSEQUENTIAL DAMAGES, EVEN IF EPRI OR ANY EPRI REPRESENTATIVE HAS BEEN ADVISED OF THE POSSIBILITY OF SUCH DAMAGES) RESULTING FROM YOUR SELECTION OR USE OF THIS DOCUMENT OR ANY INFORMATION, APPARATUS, METHOD, PROCESS, OR SIMILAR ITEM DISCLOSED IN THIS DOCUMENT.

REFERENCE HEREIN TO ANY SPECIFIC COMMERCIAL PRODUCT, PROCESS, OR SERVICE BY ITS TRADE NAME, TRADEMARK, MANUFACTURER, OR OTHERWISE, DOES NOT NECESSARILY CONSTITUTE OR IMPLY ITS ENDORSEMENT, RECOMMENDATION, OR FAVORING BY EPRI.

THE FOLLOWING ORGANIZATIONS, UNDER CONTRACT TO EPRI, PREPARED THIS REPORT:

Pittsburgh Technical LLC.

The Hastings Group, LLC

LPI, Inc.

THE TECHNICAL CONTENTS OF THIS PRODUCT WERE **NOT** PREPARED IN ACCORDANCE WITH THE EPRI QUALITY PROGRAM MANUAL THAT FULFILLS THE REQUIREMENTS OF 10 CFR 50, APPENDIX B. THIS PRODUCT IS **NOT** SUBJECT TO THE REQUIREMENTS OF 10 CFR PART 21.

NOTE

For further information about EPRI, call the EPRI Customer Assistance Center at 800.313.3774 or e-mail askepri@epri.com.

Electric Power Research Institute, EPRI, and TOGETHER...SHAPING THE FUTURE OF ELECTRICITY are registered service marks of the Electric Power Research Institute, Inc.

Copyright © 2018 Electric Power Research Institute, Inc. All rights reserved.

ACKNOWLEDGMENTS

The following organizations, under contract to the Electric Power Research Institute (EPRI), prepared this report:

Pittsburgh Technical LLC.
9687 Babcock Blvd.
Allison Park, PA 15101

Principal Investigator
Sola Talabi Ph.D.

The Hastings Group, LLC
1915 Ewing Avenue, Suite 3
Charlotte, NC 28203

Principal Investigator
Peter Hastings

LPI, Inc.
36 Main Street
Amesbury, MA 01913

Principal Investigator
Gregory Zysk

Acknowledgment:

This material is based upon work supported by the Department of Energy under Award Number DE-NE0008468.

Disclaimer:

“This report was prepared as an account of work sponsored by an agency of the United States Government. Neither the United States Government nor any agency thereof, nor any of their employees, makes any warranty, express or implied, or assumes any legal liability or responsibility for the accuracy, completeness, or usefulness of any information, apparatus, product, or process disclosed, or represents that its use would not infringe privately owned rights. Reference herein to any specific commercial product, process, or service by trade name, trademark, manufacturer, or otherwise does not necessarily constitute or imply its endorsement, recommendation, or favoring by the United States Government or any agency thereof. The views and opinions of authors expressed herein do not necessarily state or reflect those of the United States Government or any agency thereof.”

This publication is a corporate document that should be cited in the literature in the following manner:

Advanced Nuclear Technology: Integrated Pressurized Water Reactor (iPWR) Containment Aerosol Deposition Behavior: Phase 2b – Results and Analysis. EPRI, Palo Alto, CA: 2018. 3002013032.

ABSTRACT

Under assumed severe accident conditions, a nuclear reactor's containment vessel provides a defense-in-depth function by preventing radionuclide particle release. This is achieved by creating a physical barrier and by decontaminating aerosols produced during the accident. Decontamination occurs through active mechanical systems (where applicable) and passive natural occurring phenomena. Due to their comparatively higher containment surface area to volume ratios when compared to large light water reactors (LWRs), the integrated pressurized water reactor (iPWR) subcategory of small modular reactors (SMRs) has design features that increase the significance of the passive decontamination factors, due to the following natural occurring phenomena: gravitational settling, thermophoresis, diffusiophoresis, and impaction due to convective flows. The purpose of this study is to provide estimates for the decontamination associated with these phenomena. Specifically, this report provides decontamination factors associated with the thermal-hydraulic and geometric parameters that characterize iPWRs, based on the experimental work documented in this report.

Keywords

Integrated pressurized water reactor (iPWR)

Small modular reactor (SMR)

Aerosol

Decontamination

Passive containment

Phoresis

Deliverable Number: 3002013032

Product Type: Technical Report

Product Title: Advanced Nuclear Technology: Integrated Pressurized Water Reactor (iPWR) Containment Aerosol Deposition Behavior: Phase 2b – Results and Analysis

PRIMARY AUDIENCE: iPWR designers and safety analysis professionals.

SECONDARY AUDIENCE: Regulatory agencies.

KEY RESEARCH QUESTION

Due to their comparatively higher containment surface area to volume ratios when compared to large light water reactors (LWRs), the integrated pressurized water reactor (iPWR) subcategory of small modular reactors (SMRs) has design features that increase the significance of the passive decontamination factors, due to the following natural occurring phenomena: gravitational settling, thermophoresis, diffusiophoresis, and impaction due to convective flows. The increase in potential decontamination factors opens the possibility for a reduced public exposure in accident scenarios.

EPRI released a Phase I study in 2014, EPRI 3002004218, *Advanced Nuclear Technology: Integrated Pressurized Water Reactor (iPWR) Containment Aerosol Deposition Behavior, Phase 1 – Test Plan Development*, that identified the critical natural deposition mechanisms and examined the potential for reduced source terms.

EPRI released an additional study in January 2018, EPRI 3002010491, *Advanced Nuclear Technology: Integrated Pressurized Water Reactor (iPWR) Containment Aerosol Deposition Behavior – Phase 2a: Technical Basis and Test Plan for Experimental Testing and Computational Fluid Dynamics Analysis*. This study provided the requirements definition and technical basis for examining iPWR aerosol deposition mechanisms and estimating decontamination factors using experimental data and CFD simulations.

This Phase 2b report provides results for the final phase, which includes an estimation of iPWR decontamination factors based on a series of experiments and CFD simulations.

RESEARCH OVERVIEW

This study builds on the Phase 1 and Phase 2a studies, with an objective to develop estimates of the decontamination factors associated with natural deposition mechanisms. Estimation of the decontamination factors is performed by experimentally measuring the aerosol decontamination rates associated with the natural deposition mechanisms along with simulation of these mechanisms with a computational fluid dynamics (CFD) code. This final report provides the iPWR decontamination factors, along with the process by which they are determined, which includes details for experimental tests conducted and CFD simulations.

KEY FINDINGS

The results of this study indicate that the iPWR decontamination factors are significantly higher compared to larger, more traditional containments, and in the range of decontamination factors for containment vessel spray systems in large reactors.

This important finding is substantiated by additional findings related to the significance of deposition mechanisms that contribute to the higher decontamination factor. Specifically, convective flow was identified as an additional and significant particle transport and deposition mechanism, while thermophoresis and diffusiophoresis are also shown to be more significant for iPWRs due to higher thermal and steam concentration gradients, respectively.

WHY THIS MATTERS

This work will assist the nuclear industry by providing improved analytical correlations to model aerosol decontamination for iPWR-specific, post-accident, thermal-hydraulic environments and design configurations. Improved correlations are expected to result in a more realistic calculation of containment aerosol natural deposition.

HOW TO APPLY RESULTS

Users may apply the results of this work by modification of existing methods or development of CFD models to estimate design specific aerosol decontamination factors.

LEARNING AND ENGAGEMENT OPPORTUNITIES

EPRI performed this work in collaboration with the U.S. Department of Energy.

EPRI CONTACTS: Ron King, Program Manager, rking@peri.com

PROGRAM: Advanced Nuclear Technology

IMPLEMENTATION CATEGORY: Reference - Technical Basis

CONTENTS

ABSTRACT	v
EXECUTIVE SUMMARY	vii
1 REPORT SUMMARY	1-1
A EXPERIMENTAL VERIFICATION OF POST-ACCIDENT INTEGRATED PRESSURIZED WATER REACTOR (IPWR) AEROSOL BEHAVIOR – RESULTS AND ANALYSIS (PR-PIT-3-18-1).....	A-1

1

REPORT SUMMARY

The United States Nuclear Regulatory Commission (USNRC) and the International Atomic Energy Agency (IAEA) acknowledge that radiological source terms associated with a Small Modular Reactor (SMR) may be significantly different from that associated with a Large Light Water Reactor (LLWR). Source terms are influenced by radionuclide inventory in the core, and the in-containment vessel environment, including the geometry. SMR designs with an integrated containment vessel (CV), called Integrated Pressurized Water Reactors (iPWR) have CV volumes that are significantly smaller than LLWRs. Currently in the US, there are four major iPWR designs that have been advertised, i.e., by NuScale, BWX Technologies (mPower), Westinghouse, and Holtec. International designs include SMART (Korea) and CAREM (Argentina).

A typical iPWR CV volume is about an order of magnitude smaller than that of LLWRs and consequently, this creates a larger deposition surface area to volume ratio, which is a parameter that supports in-vessel particle deposition, for higher ratios. The surface deposition is further enhanced for iPWRs immersed in water, due to the creation of a thermal gradient and condensation on the CV wall surface. The thermal gradient creates three effects that enhance deposition mechanisms: thermophoresis due to a difference in temperature, diffusiophoresis due to a difference in steam concentration, and convective flows due to the temperature difference between the hotter reactor vessel (RV) wall and the cooler CV wall. Gravitational settling as a deposition mechanism has also been identified as potentially being more significant for iPWR designs with relatively clean stainless-steel CVs, which may result in higher aerosol densities due to reduced or eliminated interaction with concrete and debris in the vessel. These identified deposition mechanisms are passive in nature, and are particularly significant for iPWRs because these designs have largely eliminated some of the active mechanical systems such as containment vessel sprays.

Prior studies (EPRI 3002004218) suggest that these passive mechanisms are likely to result in higher post-accident decontamination factors (DF) as compared with those assumed for LLWRs. The objective of this study, performed in collaboration with the U.S. Department of Energy, is to develop estimates of the aerosol removal rates associated with the passive deposition mechanisms for an expected range of geometric and thermal-hydraulic parameters that are characteristic of iPWR designs. These aerosol removal rates are used to calculate DFs. To capture a wide range of thermal-hydraulic and design parameters for iPWR designs, the aerosol removal rates are determined with the use of an experimental test loop and CFD simulations. The experimental test loop provides an estimate of range of iPWR design parameters and also benchmarks the CFD model, which is then used to provide estimates for a wider range of parameters.

The study has two major parts, which include: 1) Development of the technical basis to estimate iPWR aerosol decontamination factors with experiments and CFD simulations, and 2) Development of iPWR aerosol decontamination factor estimates based on execution of experiments and CFD simulations. The first part of the current study has been completed and reported (EPRI 3002010491). This report provides the final documentation of results and analysis for the second part.

A

EXPERIMENTAL VERIFICATION OF POST-ACCIDENT INTEGRATED PRESSURIZED WATER REACTOR (IPWR) AEROSOL BEHAVIOR – RESULTS AND ANALYSIS (PR-PIT-3-18-1)

Notice: The following attached document was prepared in accordance with the EPRI Nuclear Quality Assurance Program as an output of an augmented quality project.

EXPERIMENTAL VERIFICATION OF POST-ACCIDENT INTEGRATED PRESSURIZED WATER REACTOR (IPWR) CONTAINMENT AEROSOL BEHAVIOR

RESULTS AND ANALYSIS

TECHNICAL REPORT


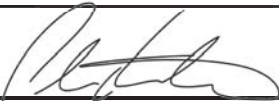

PR-PIT-3-18-1

March 2018

VERSION HISTORY

Version #	Implemented By	Revision Date	Comments
0	Rohan Biwalkar Kenneth Redus Teffik Gemci Ph.D. Paul Fischbeck Ph.D. Sola Talabi Ph. D.	TBD	Original Version

Revision Approvals

Name	Role	Signature	Date
Sola Talabi Ph.D.	Project Manager, Pittsburgh Technical		3/26/2018
Peter Hastings	Technical Project Manager, EPRI (Acting on behalf of EPRI)		03/26/2018
Ronald King	Project Manager, EPRI	 Ronald K, King 2018.03.27 07:57:01 -07'00'	

Contents

1	Introduction	8
2	Potential Impact of Research: Comparison of iPWR Decontamination Factors based on Current findings and Prior Art	13
3	Experimental Data and CFD Simulation Results	15
3.1	Comparison of Baseline Cases and Establishing the Significance of Convective Flow	19
3.2	Comparison of the Effects of Varying Temperature Gradient in the Absence of Steam (TGC) ..	22
3.3	Comparison of the Effects of Varying Temperature Gradient in the Presence of Steam (TGCD) 24	
3.4	Comparison of the Effects of Variation of Pressure in the Absence of Steam (TGC)	25
3.5	Comparison of the Effects of Variation of Pressure in the Presence of Steam (TGCD)	25
3.6	Comparison of the Effects of Varying A/V ratio in the Absence of Steam (TGC)	26
3.7	Comparison of the Effects of Varying A/V ratio in the Presence of Steam (TGCD)	27
3.8	Additional Estimates of Aerosol Deposition Rates Performed by CFD Simulations	28
3.9	Comparison of Decontamination Rates with Varying Particle Diameter	29
3.10	Comparison of Experimental and CFD Results	31
4	Discussion of results	34
4.1	Establishing the Significance of Convective Flow	34
4.2	Effects of Varying Temperature Gradient in the Absence of Steam	35
4.3	Effects of Varying Temperature Gradient in the Presence of Steam	36
4.4	Comparison of Effects of Varying Pressure	36
4.5	Effects of Varying A/V Ratio	36
4.6	Comparison of Decontamination Rates with Varying Particle Diameter	37
4.7	Comparison of Experimental and CFD Results	37
4.8	CFD Model Comparison with Results from Relevant Prior Experiments	38
4.9	In-line Loss Characterization Test	39
4.10	Vessel Wall Impaction Test	39
5	Application of Results: Scaling	40
5.1	Aerosol Scaling	41
5.1.1	Scaling Factors for Critical Parameters	42
5.1.2	Inclusion of the Effects of Convective Flow with Aerosol Removal Rates for Turbulence and Impaction	43
5.1.3	Implementation Approach	43

5.2	Thermal-Hydraulic Scaling	43
6	Application of Results: Estimation of iPWR Decontamination Factors.....	45
7	Conclusions and Recommendations	49
8	References	51
Appendix A: Statistical Analysis		53
	Data Collection and Processing.....	60
	Power Analysis	64
	Summary Statistics for T80, T90, and T95.....	64
	Effects of Test Conditions on T80, T90, and T95.....	66
	Probability Functions for T80, T90, and T95	68
Appendix B: Summation of Aerosol Decontamination Parameters		71
	CFD-Specific Considerations	72
Appendix C: Experimental Data		74
Appendix D: Sensitivity study of experimental and CFD geometry		90
	Simulation Setup.....	90
	Results and Discussion	91
	Conclusions	94
Appendix E: Application of Results – Supplemental Requirements for Aerosol Deposition Estimation Codes.....		95
	Particle Distribution Modeling	95
	Diffusiophoresis Deposition Models Using Stefan Flow and Slip Coefficient Correction Factor	96
	Gravitational Settling Calculations with Actual Particle Sizes.....	98
	Modeling the Variations in the Thermal-hydraulic Environment and Accurate Calculations of Thermal-hydraulic Parameters	98
	Modeling Phenomena Fluctuations due to Changing Thermal-Hydraulic Parameters	100
	Modeling Convective Flow as a Particle Transport Mechanism	100
	Modeling of Turbulent Inertial Impaction	103
Appendix F: Additional Research Questions		104

List of Figures

Figure 1: Decontamination Factor for LLWR and iPWR (Prior Art and Current Study).....	14
Figure 2: Actual and mean experimental results for the G baseline case (case 1).....	19
Figure 3: Actual and mean experimental results for the TGC baseline case (case 2).....	20
Figure 4: Actual and mean experimental results for the TGCD baseline case (case 5)	20
Figure 5: Comparison of experimentally-obtained decontamination curves for baseline cases	21
Figure 6 Comparison of decontamination curves for baseline cases obtained from CFD simulations	21
Figure 7: Comparison of effects of varying temperature for TGC cases obtained from experiments	22
Figure 8: Temperature effects for ABCOVE tests (SNL, 1994)	23
Figure 9: Comparison of Temperature gradient effects (without steam) obtained from CFD simulations	23
Figure 10: Comparison of Temperature gradient effects (with steam) obtained from experiments	24
Figure 11: Comparison of Temperature gradient effects (with steam) obtained from CFD simulations...	24
Figure 12: Comparison of effects of varying pressure for TGC cases obtained experimentally.....	25
Figure 13: Comparison of effects of varying pressure for TGCD cases obtained from experiments.....	26
Figure 14: Comparison of effect of varying pressures obtained from CFD	26
Figure 15: Comparison of effects of varying A/V ratio for TGC cases.....	27
Figure 16: Comparison of effects of varying A/V ratio for TGCD cases obtained experimentally.....	27
Figure 17: Comparison of effects of varying A/V ratio obtained from CFD	28
Figure 18: Comparison of effects of varying A/V ratio obtained from CFD simulations (TGCD, outside testing range).....	29
Figure 19: Comparison of CFD results for gravitational settling effectiveness vs. particle diameter.....	30
Figure 20: Comparison of CFD results for TGC effectiveness vs. particle diameter	30
Figure 21: Comparison of CFD results for TGCD effectiveness vs. particle diameter.....	31
Figure 22: Comparison of decontamination rate curves from Experiments and CFD Simulations for Case 1	32
Figure 23: Weighted average curve for gravitational settling	32
Figure 24: Comparison of decontamination rate curves from Experiments and CFD Simulations for Case 2 (TGC)	33
Figure 25: Comparison of decontamination rate Curves from Experiments and CFD Simulations for Case 5 (TGCD)	33
Figure 26: Aerosol deposition velocities associated with various phenomena and conditions (EPRI, 2014b)	35
Figure 27: Comparison of results from the current study and the Phebus test for similar particle diameters (NRC, 2014)	39
Figure 28: Normalized particle mass vs. time for Characteristic Case.....	47
Figure 29: Aerosol decontamination rate vs. time for Characteristic Case	47
Figure 30: DF vs. time for Characteristic Case	48
Figure 31: DE vs. time for Characteristic Case	48
Figure 32: Decontamination Factor at T(95/95) for the Characteristic Case and all TC	54
Figure 33: Normalized Mass Curve Fit for Characteristic Case and all TC	55
Figure 34: Decontamination Factor Curve Fit for Characteristic Case and all TC	55
Figure 35: Curve fit for experimental case 5.....	56
Figure 36: Curve fit for experimental case 6.....	56

Figure 37: Curve fit for experimental case 7.....	57
Figure 38: Curve fit for experimental case 10.....	57
Figure 39: Curve fit for experimental case 11.....	58
Figure 40: Curve fit for experimental case 13.....	58
Figure 41: Curve fit for experimental case 15.....	59
Figure 42: T80 Histogram and Summary Statistics	65
Figure 43: T90 Histogram and Summary Statistics	65
Figure 44: T95 Histogram and Summary Statistics	65
Figure 45: Effect of T_{RV} ($^{\circ}$ F) on T80, T90, and T95	66
Figure 46: Effect of P (psi) on T80, T90, and T95	67
Figure 47: Effect of A/V on T80, T90, and T95	68
Figure 48: Triangular Probability Functions for T80, T90, and T95 (with T95/95 = 69.16 minutes indicated)	69
Figure 49: Vectorial calculation of deposition velocities	72
Figure 50: Experimental decay curve for gravitational settling (Case 1)	75
Figure 51: Experimental decay curve for TGC case with $T_{RV} = 500^{\circ}$ F (Case 2).....	76
Figure 52: Experimental decay curve for TGC case with $T_{RV} = 450^{\circ}$ F (Case 3).....	77
Figure 53: Experimental decay curve for TGC case with $T_{RV} = 400^{\circ}$ F (Case 4).....	78
Figure 54: Experimental decay curve for TGCD case with $T_{RV} = 500^{\circ}$ F (Case 5)	79
Figure 55: Experimental decay curve for TGCD case with $T_{RV} = 450^{\circ}$ F (Case 6)	80
Figure 56: Experimental decay curve for TGCD case with $T_{RV} = 400^{\circ}$ F (Case 7)	81
Figure 57: Experimental decay curve for TGC case with A/V ratio = 0.6 ft^{-1} (Case 8).....	82
Figure 58: Experimental decay curve for TGC case with A/V ratio = 0.75 ft^{-1} (Case 9).....	83
Figure 59: Experimental decay curve for TGCD case with A/V ratio = 0.6 ft^{-1} (Case 10)	84
Figure 60: Experimental decay curve for TGCD case with A/V ratio = 0.75 ft^{-1} (Case 11)	85
Figure 61: Experimental decay curve for TGC case with P = 65 psi (Case 12)	86
Figure 62: Experimental decay curve for TGCD case with P = 65 psi (Case 13)	87
Figure 63: Experimental decay curve for TGC case with P = 20 psi (Case 14)	88
Figure 64: Experimental decay curve for TGCD case with P = 20 psi (Case 15)	89
Figure 65: Cut-plane section for (a) Simplified Geometry and (b) Actual Geometry	90
Figure 66: Simulation Setup for both cases	91
Figure 67: Temperature Comparison for Geometry Sensitivity Study	92
Figure 68: Pressure comparison for Geometry Sensitivity Study	92
Figure 69: Velocity profiles for (a) Simplified Geometry and (b) Dome Geometry	93
Figure 70: Sensitivity Study for actual and simplified experimental geometries	94
Figure 71: Distribution of particles inside the CV for (a) $1 \text{ }\mu\text{m}$ and (b) $10 \text{ }\mu\text{m}$ diameter particles (unitless, representing number density) (EPRI, 2017b).....	96
Figure 72: Knudsen Number Range for $1 - 10 \text{ }\mu\text{m}$ particles	97
Figure 73: Gravitational settling decontamination rates for experimental and simulated cases	98
Figure 74: Temperature [K] distribution inside the CV (EPRI, 2017b)	99
Figure 75: Steam concentration distribution inside the CV (EPRI, 2017b)	100
Figure 76: Convective flow shown by velocity field [m/s] inside the CV (EPRI, 2017b).....	101

List of Tables

Table 1: Phase 2b experimental and simulation parameters	15
Table 2: Considerations for Aerosol Model Development: Effects of thermal-hydraulic parameters on particle deposition and transport	17
Table 3: Presentation of experimental and CFD results	18
Table 4: Test parameters for the ABCOVE tests	22
Table 5: Experimental Parameters for the Phebus test	38
Table 6: Critical Scaling Parameters	40
Table 7: Values for N_m using Double Exponential Curve for Characteristic Case and each Test Case	46
Table 8: TCGD test conditions for T80, T90, and T95 test results	61
Table 9: TCGD Power Analysis for TGCD Test Cases	64
Table 10: Boundary and Initial Conditions for both cases	91
Table 11: Knudsen number values for particles 1-10 μm at different gas conditions	97

1 Introduction

The containment vessel in a nuclear power plant provides a physical barrier to prevent the release of radionuclide particles and also a decontamination mechanism to reduce the aerosolized radionuclide particle concentration following a postulated accident. Decontamination occurs through active mechanical systems (where applicable) and passive naturally-occurring phenomena. The integrated pressurized water reactor (iPWR) subcategory of small modular reactors (SMR) have a comparatively higher containment surface-area-to-volume ratio that improves decontamination associated with naturally-occurring phenomena when compared to large light water reactors (LWRs). These naturally-occurring phenomena are: gravitational settling, thermophoresis, diffusiophoresis and convective flows. The potential increase in decontamination factors supports the potential for reduced public and worker exposure in accident scenarios. The Electric Power Research Institute (EPRI) has conducted a series of studies to quantify the effects of iPWR thermal-hydraulic and geometric parameters on aerosol decontamination rates, which are typically characterized as decontamination factors. This report provides experimental data and Computational Fluid Dynamics (CFD) results that demonstrate the increase in decontamination factors associated with iPWR designs.

Aerosols are small airborne radionuclide particles that may be released from a nuclear reactor core in the event of an accident. These aerosols, when released into a containment vessel, will deposit on the vessel walls and floor at a time-scale dependent on the aerosol characteristics and the environment. The aerosol characteristics include particle size distribution and concentration. The environment includes the containment vessel geometry and the thermal-hydraulic conditions in the containment volume.

Aerosol deposition estimation is a well-established practice, which models aerosol behavior based on an assumed particle size distribution and known and stable thermal-hydraulic conditions, for which theoretical models have been developed. The nature of aerosol behavior and the variability in the post-accident environment of a nuclear reactor creates a significant amount of uncertainty and non-linear relationships between the various parameters. Hence, aerosol science requires a significant amount of experimental benchmarking of theoretical models to characterize aerosol behavior.

EPRI released a Phase 1 study in 2014, *Integrated Pressurized Water Reactor (iPWR) Containment Aerosol Deposition Behavior, Phase 1 – Test Plan Development* (EPRI 3002004218), which identified the potential for reduced source terms associated with natural deposition mechanisms for iPWRs.

In January 2018, EPRI released an additional study, *Advanced Nuclear Technology: Integrated Pressurized Water Reactor (iPWR) Containment Aerosol Deposition Behavior – Phase 2a: Technical Basis and Test Plan for Experimental Testing and Computational Fluid Dynamics Analysis* (EPRI 3002010491). This study provides the requirements definition and technical basis for examining iPWR aerosol deposition mechanisms and estimating decontamination factors using experimental data and CFD simulations, and is the underlying technical basis for the results reported in the current study.

A Phase 2b study was initiated to implement Phase 2a requirements. The Phase 2b results are presented here. The results summarize how utilizing a series of controlled experiments and CFD simulations support characterization of aerosol removal rates associated with a range of thermal-hydraulic and geometric parameters typical of iPWR post-accident conditions. This report also provides decontamination factors

associated with iPWR designs to demonstrate enhanced decontamination by aerosol deposition that occurs in the unique geometry and thermal-hydraulic conditions present in an iPWR containment during post-accident core damage aerosol generation and depletion.

The following objectives were accomplished in the Phase 2b study.

1. Perform experiments to establish aerosol deposition rates for key phenomena of interest: thermophoresis, diffusiophoresis, gravitational settling and convective flow.
2. Validate the performance of CFD models using experimental results.
3. Provide decontamination factor estimates for a range of post-accident iPWR geometries and thermal- hydraulic conditions.

This report is organized as follows:

Section 1	Introduction: Statement of Phase 2b study objectives and overview of aerosol deposition experimental and modeling requirements.
Section 2	Potential Impact of Research: Comparison between calculations of iPWR decontamination factors based on current findings and prior methods. A comparison is also made between decontamination factors for iPWRs and Generation III+ designs. ¹
Section 3	Experimental Data and CFD Simulation Results -The following results are presented: <ul style="list-style-type: none">• Experimentally determined aerosol deposition rates.• CFD estimates of aerosol deposition rates for test configurations.• CFD estimates of aerosol deposition rates for a range of iPWR containment vessel surface-area-to-volume ratios beyond the tested range.• Verification of the applicability of the aerosol deposition rates by comparison of experimental and CFD simulated results.
Section 4	Discussion of Results: Results are evaluated in the context of deposition mechanisms.
Section 5	Application of Results – Scaling: Scaling is described in the context of the similitude method. Specific opportunities to improve aerosol deposition estimation by including the effects of convective flow are addressed.
Section 6	Application of Results – Estimation of iPWR Decontamination Factors.
Section 7	Conclusions and Recommendations: A summary of the major findings and recommendations are identified to improve aerosol deposition estimation methods and modeling.
Appendix A	Statistical Analysis: Results from the statistical analysis of the experimental data includes an uncertainty analysis on the variability of results and establishes confidence levels associated with the experimental data.
Appendix B	Summation of Aerosol Decontamination Parameters: Vector summation as a combination approach is discussed using the methodology in an applicable Nuclear Regulatory Commission (NRC) guidance document (NUREG/CR-6189) and includes a description for CFD-specific implementation.
Appendix C	Experimental data charts.

¹ Generation III+ (Gen III+) refers to nuclear reactors with significant improvements in safety and economics over generation III designs. Examples include the Westinghouse AP1000 and Areva EPR.

- Appendix D Sensitivity study of experimental and simplified containment vessel geometry: A study to understand the effects of differences between dome-shaped geometry and simplified rectangular geometry in the CFD model.
- Appendix E Application of Results – Requirements for Aerosol Deposition Models: Key issues are identified and recommendations are provided to address the issues for enhanced deposition modeling:
- *Potential discontinuities and fluctuations occur in the deposition phenomena.* Diffusiophoresis stops due to a cessation of steam condensation as a result of a drop in pressure.
 - *Boundary layer fluctuations are associated with variations in the thermal-hydraulic radial domains from the reactor vessel (RV) wall to the containment vessel (CV) wall.* This includes the superheated, saturated and condensation domains. The fluctuations affect the time duration of the various domains. The fluctuations also affect thermal and steam concentration gradients subsequently impacting thermophoresis and diffusiophoresis respectively.
 - *Changes occur in deposition rates due to particle growth and agglomeration (in which the particle size is assumed to stay constant after growth) and due to particle growth due to steam condensation, in which the particle size may reduce due to evaporation.*
 - *Specific recommendations for the discrete method:* Modifications to the discrete method as currently used in the CFD model are needed. Roles of key parameters (such as the Knudsen number) are emphasized to properly represent the effects of the thermal-hydraulic environment and particle characteristics.
- Appendix F Additional Research Questions: A list of additional related research questions is presented. The list uses inputs from the NRC and an iPWR designer.

Conversion Factors:

Parameter	Conversion
Area	1 in ² = 6.45 cm ² 1 ft ² = 929 cm ²
Density	1 lb/ft ³ = 16 kg/m ³ 1 g/cm ³ = 0.036 lb/in ³
Distance	1 μm = 10 ⁻⁶ m = 0.00004 in. 1 mm = 0.0394 in. 1 ft = 0.305 m 1 in. = 2.54 cm
Energy	1 J = 0.738 lbf-ft
Flow	1 L/minute = 0.264 gpm
Gravity	32.2 ft/sec ² = 9.81 m/sec ²
Mass	1 g = 0.0353 oz 1 lb = 0.4536 kg
Pressure	1 psi = 6.89 kPa
Temperature	°C = (°F – 32) × 5/9 °C = K – 273.15 °C = (°R – 491.67) × 5/9 °F = (°C × 9/5) + 32 °F = K × 9/5 – 459.67 °F = °R – 459.67
Velocity	1 ft/sec = 0.3048 m/sec
Viscosity	1 lb/ft-sec = 1488.164 cP

Nomenclature:

Symbols used in this document are listed in this section, along with the relevant units. The symbol and subscript are listed separately for clarity. As an example, for an equation that contains the symbol 'd_p', referring to this list will indicate that 'd_p' means particle diameter, since the symbol 'd' refers to diameter and the subscript 'p' refers to particle.

Latin Alphabets: Uppercase

D:	Diffusion Coefficient [m ² /s]
DE:	Decontamination efficiency [-]
DF:	Decontamination factor [-]
K _o :	Agglomeration Kernel [-]
M:	Dimensionless particle mass density [-]
N:	Dimensionless particle concentration/mass [-]
P:	Reactor Thermal Power [MWth], Pressure (in velocity equations) [Pa]
Q:	Fluid Flow rate [m ³ /s]
T:	Temperature [K]
U:	Flow Velocity [m/s]
V:	Dimensionless Volume [-], Velocity (only in the context of particle deposition) [m/s]
V':	Dimensionless Volume [-]
Y:	Mass fraction [-]

Latin Alphabets: Lowercase

d:	Diameter [m]
g:	Acceleration due to gravity [m/s^2]
m:	Particle mass density [kg/m^3]
n:	Particle concentration (number density) [m^{-3}]
t:	Time [s]
u:	Velocity [m/s]
v:	Volume [m^3]
z^+ :	Dimensionless height [-]

Greek Symbols

γ :	Collision Shape Factor [-]
δ_Σ :	Uncertainty Indicator [-]
ϵ_0 :	Efficiency of gravitational coagulation [-]
θ :	Dimensionless coagulation coefficient [-]
Λ :	Dimensionless aerosol removal rate [-]
λ :	Aerosol removal rate [hr^{-1} , min^{-1} or s^{-1}], particle mean free path (in context of the Knudsen number) [μm]
μ :	Gas Phase Viscosity [kg/m-s]
Π :	Dimensionless time-scale [-]
ρ :	Density [kg/m^3]
σ :	Scattering Kernel [-]
τ :	Dimensionless time [-]
χ :	Particle Settling Shape Factor, Dynamic Shape Factor (diffusiophoresis) [-]

Subscripts

0:	Jet
bj:	Break (fluid jet entry)
c:	Turbulent Convection
d:	Diffusiophoresis, deposition
f:	Fluid
g:	Gravitational settling (for velocity), Gas (for fluid properties)
m:	Mass
o:	Other
p:	Particle
sf:	Stratified Fluid
T:	Total
t:	Thermophoresis

Constants

α_T :	Taylor Entrainment Constant
k_B :	Boltzmann Constant

Dimensionless numbers:

C_c :	Cunningham Correction Factor
Kn:	Knudsen Number
Ri:	Richardson Number

2 Potential Impact of Research: Comparison of iPWR Decontamination Factors based on Current findings and Prior Art

This report describes decontamination rates associated with iPWR containment vessel thermal-hydraulic and geometric parameters for passive aerosol removal mechanisms. The impact of this study can be described by comparing iPWR decontamination factors for passive mechanisms, calculated based on decontamination rates estimated in the current study, against decontamination factors for passive and active mechanisms, based on existing correlations described in NRC guidance documents (NRC, 1996). A characteristic iPWR decay curve (henceforth referred to as the ‘Characteristic Case’) was estimated based on the average of the test cases that represent the iPWR post-accident conditions, as described in the statistics section of this report. The passive decontamination mechanisms that are active in the iPWR include: thermophoresis, diffusiophoresis, gravitational settling and convective flow. A comparison is made between the characteristic iPWR decontamination factor and decontamination factors using the relationships for a large light water reactor (LLWR) with passive decontamination mechanisms and active decontamination mechanisms (containment sprays).

NUREG/CR-6189 provides a 90% confidence estimation correlation of the aerosol removal rate for ex-vessel release as follows (NRC, 1996):

$$\lambda (90) = 0.0754 + 184.9/P$$

Where λ is the aerosol removal rate and P is the reactor thermal power. For an assumed 160 MWth iPWR, the aerosol removal rate per NUREG/CR-6189 is calculated as 1.23 hr^{-1} . The decontamination factor (DF) can be expressed in terms of the aerosol removal rate λ , given by the following equation (Zhao, Zhang, & Tong, 2015):

$$DF(t) = \frac{1}{e^{-\int_0^t \lambda(t) dt}}$$

Using the NUREG/CR-6189 relationship for a 160 MWth reactor provides a decontamination factor of approximately 4.04.² This represents the decontamination factor that may have been calculated for iPWRs based on NUREG/CR-6189 guidance, prior to performance of this study. Section 6 and Appendix A of this report provide greater detail on estimation of the decontamination factor for the characteristic iPWR thermal-hydraulic and geometric conditions as a value of approximately 19.3.

Using the NUREG/CR-6189 correlations, the decontamination factor for a 3415 MWth generation III+ PWR is estimated at approximately 1.20.³ Using guidelines provided in NUREG/CR-5966, the decontamination factor associated with containment vessel sprays for a 3415 MWth PWR is calculated as approximately 15 (Zhao, Zhang, & Tong, 2015). Hence, it should be noted that the decontamination factor for iPWR containment vessels is in a range similar to larger PWRs with containment sprays.

² Note that this DF is based on ex-vessel release, to match the period and conditions of the experiments in the current study.

³ The Westinghouse AP1000 is a 3314MWth generation III+ PWR design.

Figure 1 shows a comparison of decontamination factor estimates for iPWRs based on prior art and the current study. It also shows the LLWR estimates with and without containment vessel sprays. Hence, the effect of the iPWR thermal-hydraulic environment and geometry on aerosol decontamination may be equivalent to the effect of containment sprays in large reactors.

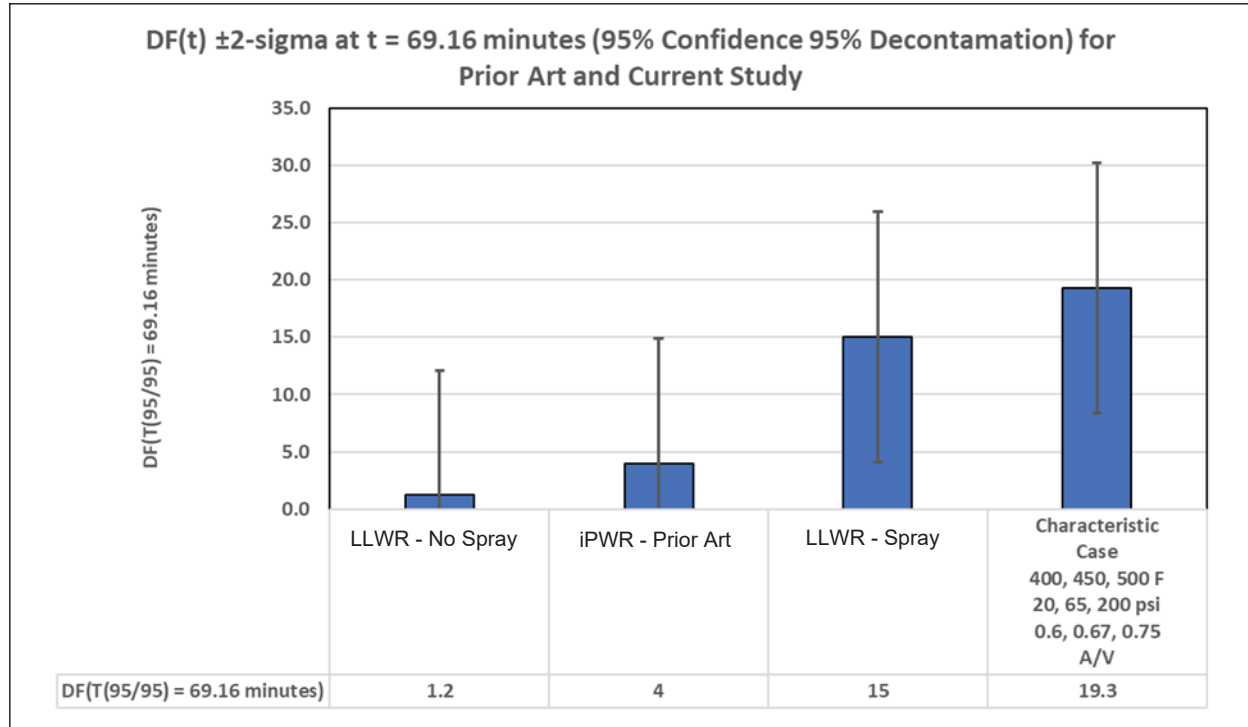


Figure 1: Decontamination Factor for LLWR and iPWR (Prior Art and Current Study)

3 Experimental Data and CFD Simulation Results

This section presents experimental results using the test cases defined in the Phase 2a test plan report (EPRI, 2017a) and compares these results to CFD simulations. Prior to performing the CFD simulations, the CFD model was calibrated and validated against prior results (EPRI, 2017b).

Table 1 identifies Phase 2b test cases to include the test case (TC) number, the type of test which identifies the aerosol deposition phenomena examined for the test case and input conditions (i.e. the initial conditions) associated with test case parameters. Table 1 also includes the surface-area-to-volume ratios which are representative of US iPWR designs. Section 4 provides a discussion of the results.

Each TC was run three times to achieve greater confidence in the test results. The average of the three runs is used to represent the test case. The test duration was 80 minutes. Details associated with the experimental parameters are further defined in the Phase 2a test plan report (EPRI, 2017a).

The experimental data was smoothed by a process called moving average filtering. In this process, several data points are taken and the noise in the data is bounded. Each data point is then replaced by a calculated average of the neighboring data points defined within the span (range of the neighboring data points). The span is typically optimized (in this case about 20 points); a broader span produces a smoother curve and the span is taken to be the minimum range beyond which the smoothed curve remains unchanged. This process is similar to low-pass filtering.

Table 1: Phase 2b experimental and simulation parameters

Test Case (TC) No.	Type	Reactor Vessel (RV) Wall temperature (T_{RV})	Containment Vessel (CV) Wall temperature (T_{CV})	Pressure (P)	Surface Area to Volume (A/V) ratio	Steam Mass Fraction (y)
		[°F]	[°F]	[psi]	[ft ⁻¹]	[-]
1 (Base)	G	500	500	200	0.67	0
2 (Base)	TGC	500	220	200	0.67	0
3		450	220	200	0.67	0
4		400	220	200	0.67	0
5 (Base)	TGCD	500	220	200	0.67	0.7
6		450	220	200	0.67	0.7
7		400	220	200	0.67	0.7
8	TGC	500	220	200	0.6	0
9		500	220	200	0.75	0
10	TGCD	500	220	200	0.6	0.7
11		500	220	200	0.75	0.7
12	TGC	500	220	65	0.67	0
13	TGCD	500	220	65	0.67	0.7
14	TGC	500	220	20	0.67	0
15	TGCD	500	220	20	0.67	0.7

(Base) denotes the base case for the test type: G (gravitational settling), TGC (thermophoresis (T), gravitational settling and convective flow (C)), TGCD (thermophoresis, gravitational settling, convective flow, and diffusiophoresis (D))

A roadmap for the remainder of this section is presented as follows:

- Section 3.1 Comparison of baseline cases and establishing the significance of convective flow examines TC 1, 2, 5
- Section 3.2 Comparison of the effects of varying temperature gradient in the absence of steam (TGC) examines TC 2, 3, 4; results from previous experiments are also examined (SNL, 1994)
- Section 3.3 Comparison of the effects of varying temperature gradient in the presence of steam (TGCD) examines Cases 5, 6, 7
- Section 3.4 Comparison of the effects of variation of pressure in the absence of steam (TGC) examines Cases 2, 12, 14
- Section 3.5 Comparison of the effects of variation of pressure in the presence of steam (TGCD) examines Cases 5, 13, 15
- Section 3.6 Comparison of the effects of varying A/V ratio in the absence of steam (TGC) examines Cases 2, 8, 9
- Section 3.7 Comparison of the effects of varying A/V ratio in the presence of steam (TGCD) examines Cases 5, 10, 11
- Section 3.8 Examines additional estimates of aerosol deposition rates performed by CFD simulations for a wider range of geometries beyond the range of geometries tested
- Section 3.9 Comparison of decontamination rates with varying particle diameter
- Section 3.10 Comparison of CFD and experimental results.

Each section includes (1) the decay curve for actual and mean experimental results, (2) an examination of results obtained when using calibrated CFD models for the case input conditions, and, (3) where applicable, an examination of results from previous experiments not part of Phase 2b scope. Note that the raw data plots from the data collection system are included in Appendix C of this report. From the CFD results, the overall normalized particle mass vs. time curve for particles of all diameters (1-10 μm), which gives a measure of the decontamination factor, was obtained by normalizing with respect to the initial mass of all the particles.

Table 2 summarizes the parameters and their effects on particle transport and deposition. This information is provided to place the aerosol deposition function and the transport function for the experimental parameters in context when comparisons are performed.

Table 2: Considerations for Aerosol Model Development: Effects of thermal-hydraulic parameters on particle deposition and transport

Parameter	Experimental or CFD Parameter	Deposition function	Transport function
Temperature gradient	T_{RV}, T_{CV}	Causes particle deposition on the containment vessel wall by thermophoresis	Gives rise to a convective flow, which leads to particle transport throughout the CV volume. Allows particle transport across thermal zones to deposition surfaces.
Pressure	P	Has a moderate effect on particle deposition velocities due to its effects on fluid viscosity	Pressure values assist in development of a steam concentration gradient, which in turn supports particle transport by diffusiophoresis. However, low pressure transients may stop the condensation at the wall and hence dissipate the steam concentration gradient, which in turn stops diffusiophoresis.
Steam concentration gradient	Y_s	Causes particle deposition on the containment vessel wall by diffusiophoresis	Aids in the transport of particles from the saturated zone (where its effects are most dominant) to the condensation zone.
Surface-Area-to-Volume ratio	A/V	Provides deposition and condensation surfaces relative to volume.	Affects particle transport because a higher A/V ratio implies a smaller volume and a shorter radial distance for the particles by the various transport mechanisms.
Particle Size and Knudsen ⁴ Number	Particle Size, Knudsen Number	Gravitational settling deposition velocities heavily dependent on particle size.	For gravitational settling, smaller particles stay suspended longer because of buoyancy and a relatively larger Knudsen number, which varies over the radial distance from the RV surface to the CV wall. This is due to the reduction in the mean free path of the gas molecules as the steam concentration increases, going from superheated conditions at the RV wall to the saturated and condensing zones closer to the CV wall.

⁴ Knudsen Number is the ratio of the molecular mean free path of the gas molecules (λ) relative to the particle diameter (d_p).

$$Kn = \frac{\lambda}{d_p}$$

Parameter	Experimental or CFD Parameter	Deposition function	Transport function
Gas viscosity and buoyancy	Gas viscosity, Buoyancy	For gravitational settling, uplift forces are determined by drag based on viscosity and buoyancy. Hence, these mechanisms are required to be implemented to properly account for gravitational related deposition.	For convective flows, gas molecule transport is achieved in the CFD code by implementation of a buoyancy model.
Domain discretization to represent thermal stratification	Domain discretization	Allows observation and analysis of particle deposition inside the condensation boundary layer.	This illustrates coupling effects; thermophoresis moves particles from the superheated zone into the saturated zone, where diffusiophoresis also acts on them to push them into the condensation zone where deposition mechanisms are effective.

The following section presents results that include (1) experimental data and CFD, (2) experimental data only and (3) CFD simulations only. Experimental results are generally presented with the corresponding simulated CFD results, if CFD was required. CFD simulations were also run for A/V ratios outside the experimental testing range and for comparison against a prior experiment, namely the Phebus test (Birchley, 2004).

CFD results are presented without experimental data for assessments with requirements that are outside the parameters of the current test. These include surface-area-to-volume ratios outside the testing range of 0.6 ft^{-1} to 0.75 ft^{-1} and measurement of deposition rates for specific particle sizes. Particle size effects can only be isolated with CFD simulations in the current study because the tests use poly-disperse particles, which include a range of sizes from 1 to $10 \text{ }\mu\text{m}$. Table 3 summarizes the presentation of experimental and CFD results.

Table 3: Presentation of experimental and CFD results

Objective of Analysis	Case Type	Experimental Results	CFD Results	Comments
Effects of gravitational settling	G	Yes	Yes	Used for CFD model validation
Effects of varying temperature in the absence of steam	TGC	Yes	Yes	Used for CFD model validation
Effects of varying temperature in the presence of steam	TGCD	Yes	Yes	Used for CFD model validation
Effects of varying A/V ratio in the absence of steam	TGC	Yes	No	CFD model for A/V ratio only required for actual accident conditions with steam.
Effects of varying A/V ratio in the presence of steam	TGCD	Yes	Yes	Used to test the ability of the CFD model to predict post-accident conditions
Effects of varying pressure in the absence of steam	TGC	Yes	No	CFD model for pressure assessment only required for actual accident conditions with steam, to assess effects on diffusiophoresis.
Effects of varying pressure in the presence of steam	TGCD	Yes	Yes	Used to validate the steam condensation rates associated with pressure.

Effects of varying A/V ratio outside experimental testing range in the presence of steam	TGCD	No	Yes	Used to develop estimates of decontamination factors outside the testing range.
Effects of varying particle diameter	G, TGC, TGCD	No	Yes	The experiments used poly-disperse particles with a size range from 1 to 10 μm , hence specific particle behavior can only be isolated with the aid of the calibrated CFD model.
Additional validation of CFD model against prior experimental data from the Phebus test.	TGCD	Yes	Yes	Additional validation against prior studies.

3.1 Comparison of Baseline Cases and Establishing the Significance of Convective Flow

Cases 1, 2 and 5 are the baseline cases for G, TGC and TGCD respectively. These cases are examined to establish the significance of convective flow.

For gravitational settling (case 1), there is no steam and no temperature gradient between the RV and CV walls; therefore, decontamination is expected to be slower than the other cases, as the only deposition mechanism is sedimentation.

For the TGC case (case 2), decontamination is expected to be faster due to the presence of a temperature gradient, which drives both thermophoresis and buoyancy-driven convective flow.

The TGCD case (case 5) is expected to undergo the fastest decontamination among the cases under consideration, since the inclusion of steam results in the activation of diffusiophoresis as an additional deposition mechanism.

Figure 2, Figure 3 and Figure 4 show the results from each of the three runs and include the mean curves for the G (Case 1), TGC (case 2) and TGCD (case 5) baseline cases respectively.

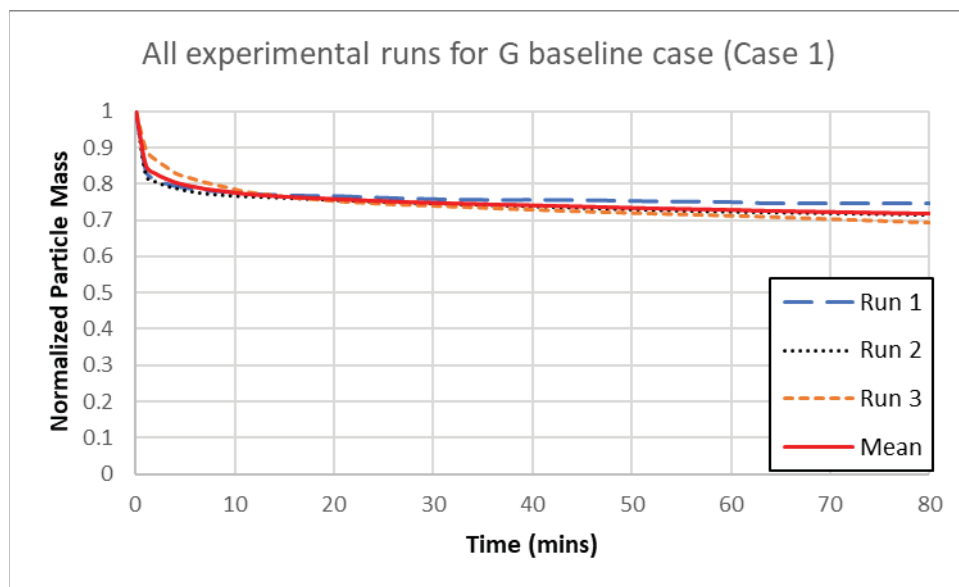


Figure 2: Actual and mean experimental results for the G baseline case (case 1)

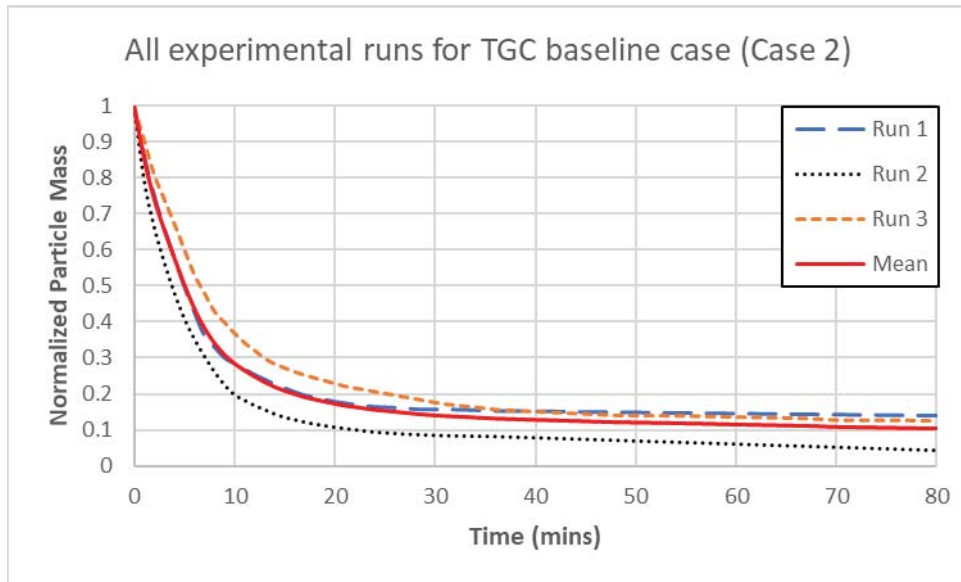


Figure 3: Actual and mean experimental results for the TGC baseline case (case 2)

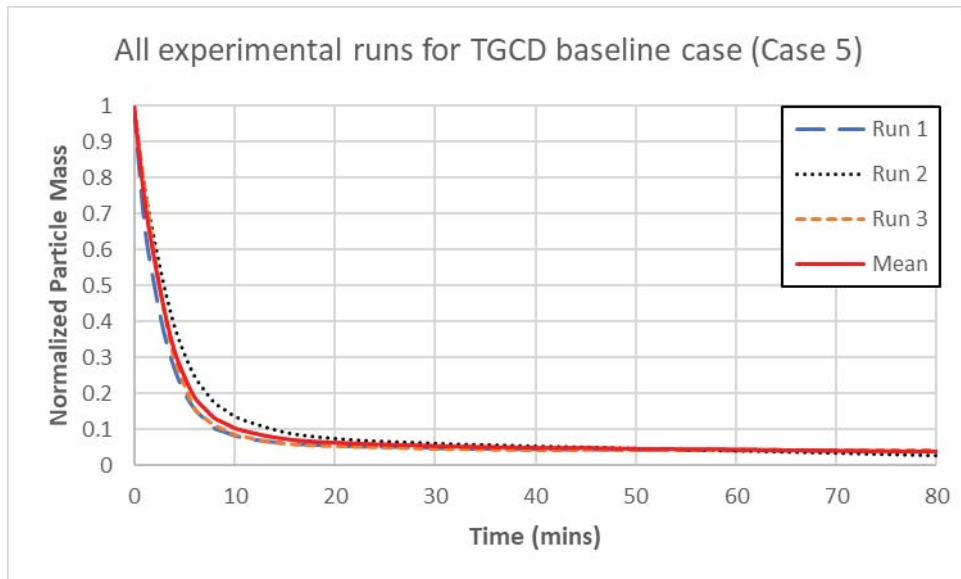


Figure 4: Actual and mean experimental results for the TGCD baseline case (case 5)

Figure 5 shows a comparison between the three baseline cases using the experimentally-obtained results. The experimentally-obtained decay curves were normalized for comparison with each other and also with the CFD results (this comparison is shown in Figure 6).

The following conclusions are drawn from the comparison of Cases 1, 2 and 5:

- The gravitational-only case (case 1) shows an initial steep drop, which is followed by relatively slow decontamination after about 20% decontamination.
- The TGC (case 2) curve shows more than 80% decontamination in the first 30 minutes.

- The TGCD (case 5) curve shows relatively faster decontamination compared to the other cases; by 20 minutes, almost 92% decontamination has taken place.

Figure 5 shows that addition of a temperature gradient enhances decontamination, which is further enhanced by the presence of steam.

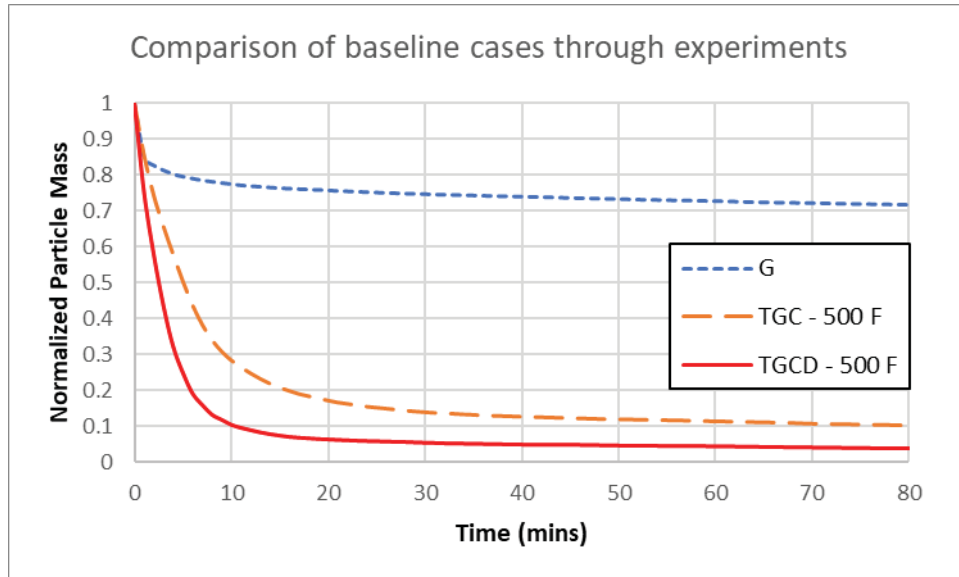


Figure 5: Comparison of experimentally-obtained decontamination curves for baseline cases

Figure 6 shows the comparison of the CFD-generated normalized particle mass vs. time for all three cases. The results from CFD simulations agree with the trend shown experimentally.

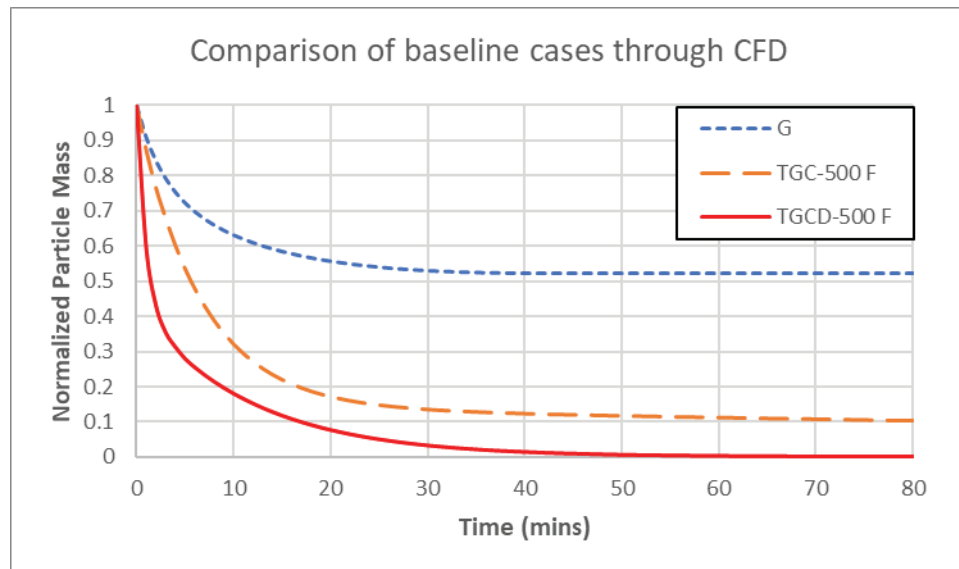


Figure 6 Comparison of decontamination curves for baseline cases obtained from CFD simulations

3.2 Comparison of the Effects of Varying Temperature Gradient in the Absence of Steam (TGC)

Cases 2, 3 and 4 are examined to ascertain the effects of varying temperature gradient from the RV wall to the CV wall, in the absence of steam. Figure 7 shows the comparison of the normalized particle mass vs. time curves for the TGC cases, obtained experimentally. It can be seen that as RV temperature increases, the decontamination becomes faster. The difference in the decontamination rates becomes more apparent as time increases.

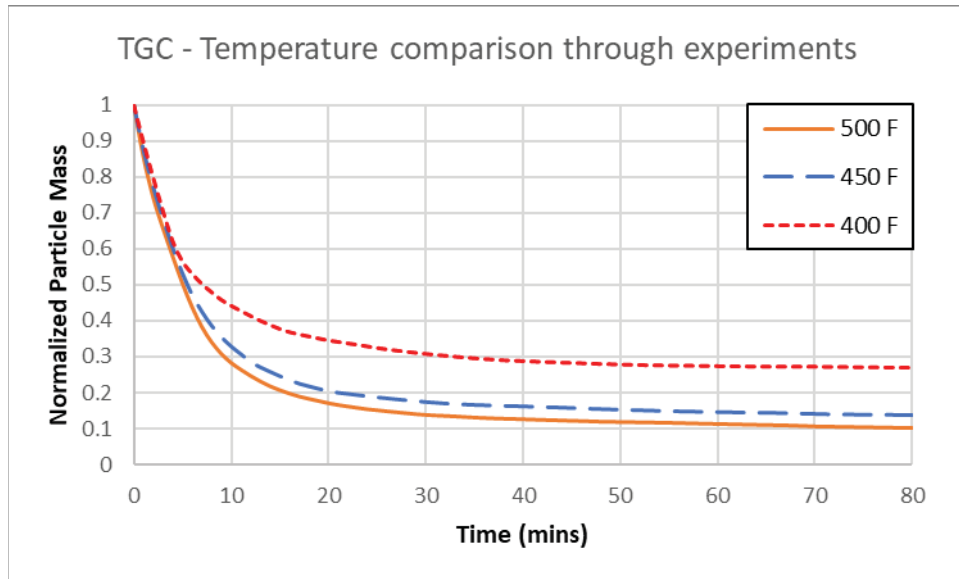


Figure 7: Comparison of effects of varying temperature for TGC cases obtained from experiments

Prior relevant in-containment aerosol deposition experiments are the Aerosol Behavior Code Validation and Evaluation (ABCOVE), LACE (LWR Aerosol Containment Experiment) and the Phebus experiments (SNL, 1994). The relevant ABCOVE program experimental results are from tests AB5, AB6 and AB7. For the ABCOVE experiments, the Containment Test System Facility (CSTF) vessel has a surface-area-to-volume ratio in the iPWR regime at 0.14 ft^{-1} . The tests were performed in a dry (no steam) environment. The test parameters for tests AB5, AB6 and AB7 are as shown in Table 4.

Table 4: Test parameters for the ABCOVE tests

Test ID	Fluid Temperature	CV wall temperature	Pressure
	[°F]	[°F]	[psia]
AB5	534.2	200.34	31.02
AB6	329.18	174.02	24.58
AB7	92.66	77.36	17.78

The difference in the overall pressure for these three tests is less than 14 psi. This small change is not expected to significantly affect the thermal-hydraulic environment. Differences in decontamination can be attributed to other factors such as temperature and the thermal gradients. The temperature gradient

is greatest in test AB5, followed by tests AB6 and AB7. Figure 8 shows data from the actual ABCOVE experiments, for normalized particle mass relative to time for each of the three tests. The results show that as the temperature gradient increases, particle deposition increases.

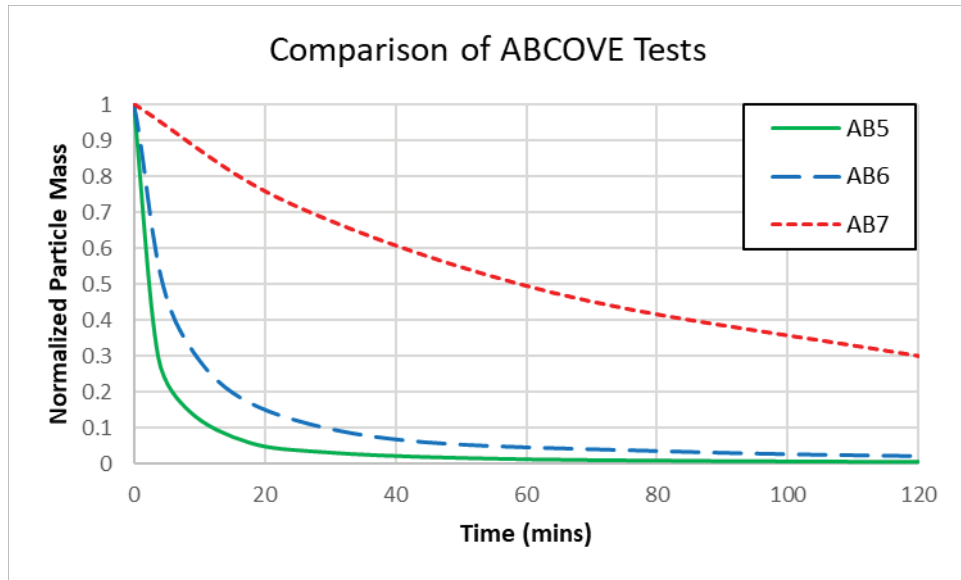


Figure 8: Temperature effects for ABCOVE tests (SNL, 1994)

Figure 9 shows a comparison of CFD results for the 400°F, 450°F and 500°F TGC cases in the current study. As temperature gradient increases, decontamination is enhanced which agrees with the experimental results.

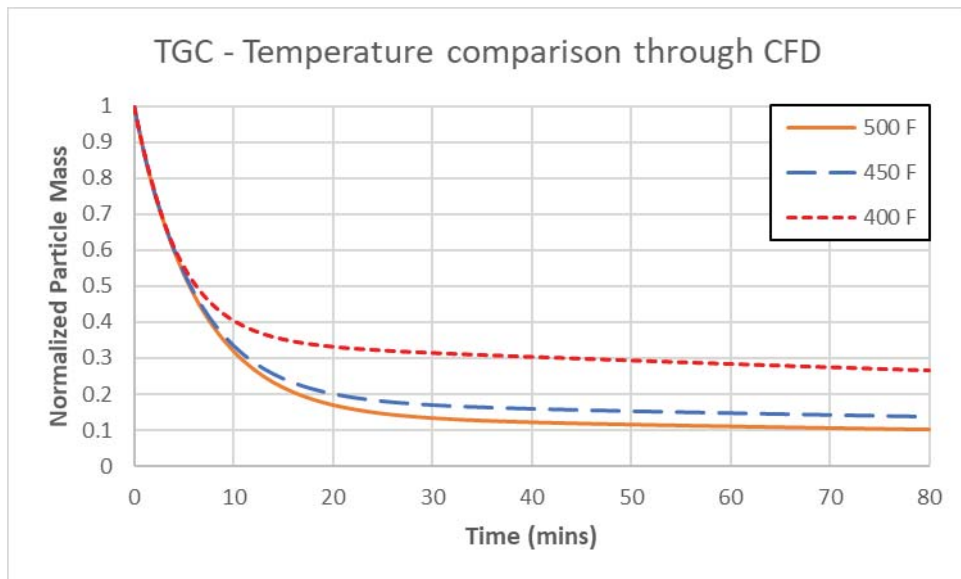


Figure 9: Comparison of Temperature gradient effects (without steam) obtained from CFD simulations

3.3 Comparison of the Effects of Varying Temperature Gradient in the Presence of Steam (TGCD)

Cases 5, 6 and 7 are examined to ascertain the effects of varying temperature gradient in the presence of steam. Figure 10 shows a comparison of the normalized particle mass vs. time curves for the TGCD cases, obtained experimentally. It can be seen that as the RV temperature increases, the decontamination becomes faster, though the difference is less pronounced when compared to the corresponding TGC cases.

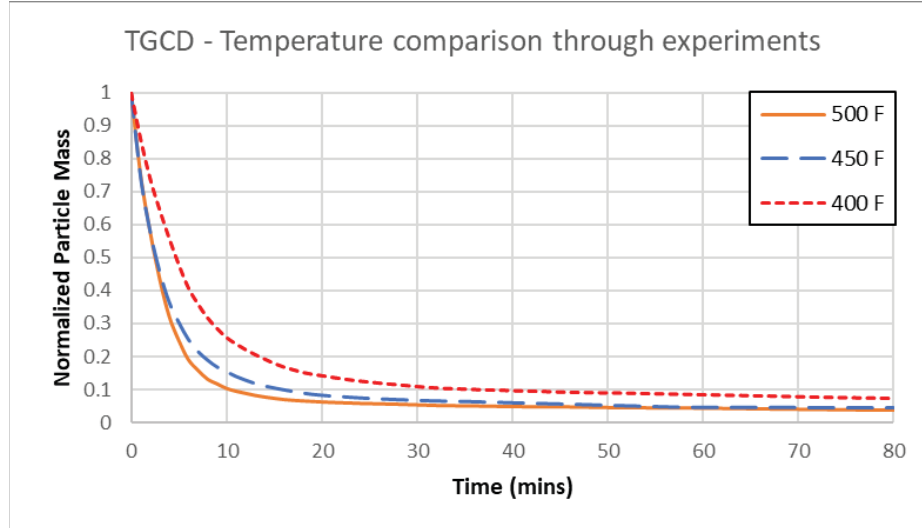


Figure 10: Comparison of Temperature gradient effects (with steam) obtained from experiments

Figure 11 shows a comparison of the corresponding CFD results for cases 5, 6 and 7. The CFD results show that the decontamination rates between the 450°F and 500°F cases are indistinguishable, but do result in somewhat greater decontamination than the 400°F case between 5 and 70 minutes.

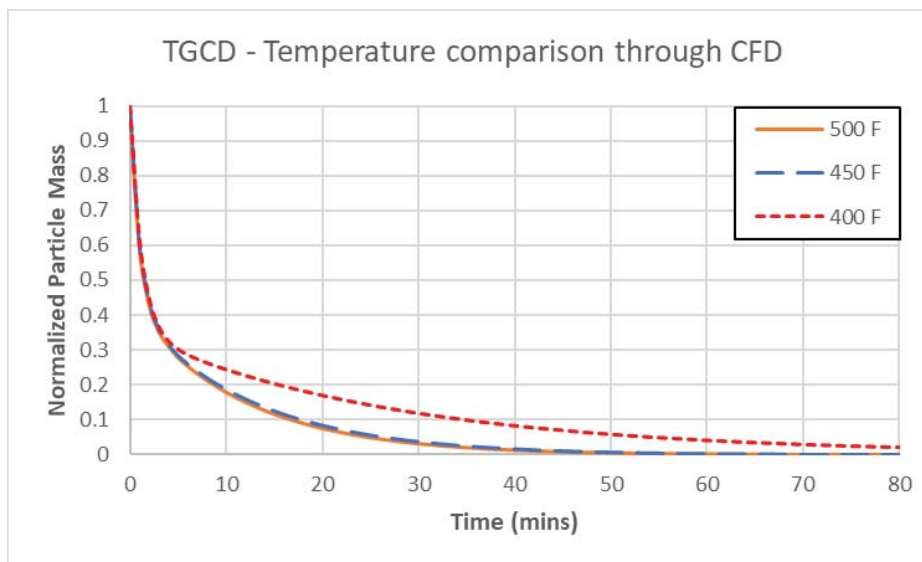


Figure 11: Comparison of Temperature gradient effects (with steam) obtained from CFD simulations

3.4 Comparison of the Effects of Variation of Pressure in the Absence of Steam (TGC)

Cases 2, 12 and 14 are examined to ascertain the effects of variation of initial pressure in the absence of steam. Figure 12 illustrates the comparison of effects of varying pressure for TGC cases obtained experimentally. Although indistinguishable from each other, the decontamination associated with the 65 psi and 200 psi cases is greater than that of the 20 psi case.

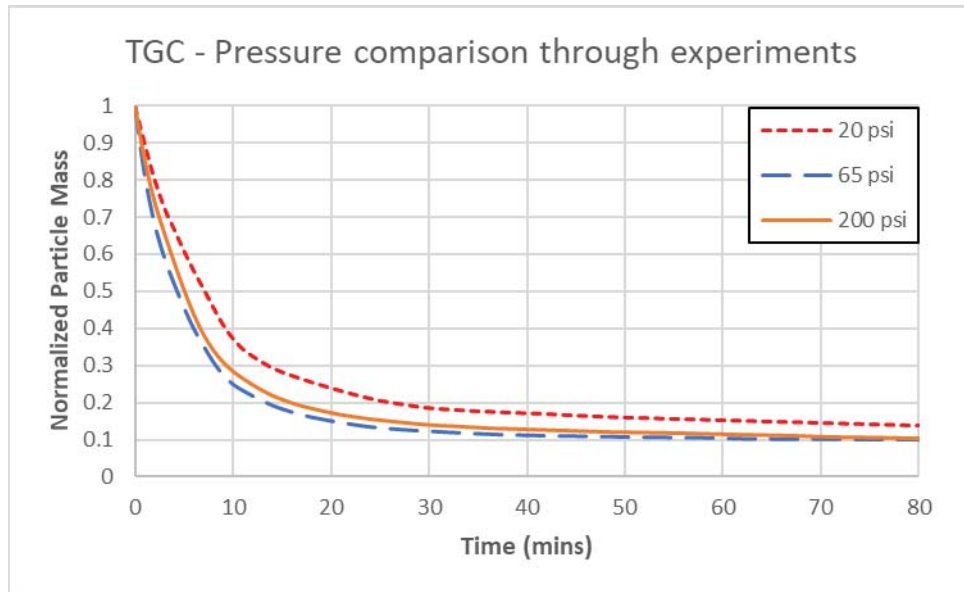


Figure 12: Comparison of effects of varying pressure for TGC cases obtained experimentally

3.5 Comparison of the Effects of Variation of Pressure in the Presence of Steam (TGCD)

Cases 5, 13 and 14 are examined to ascertain the effects of variation of initial pressure in the presence of steam. Figure 13 illustrates the comparison of effects of varying pressure for TGCD cases obtained experimentally. The results are in alignment with the results for the cases in the absence of steam, as shown in Figure 12.

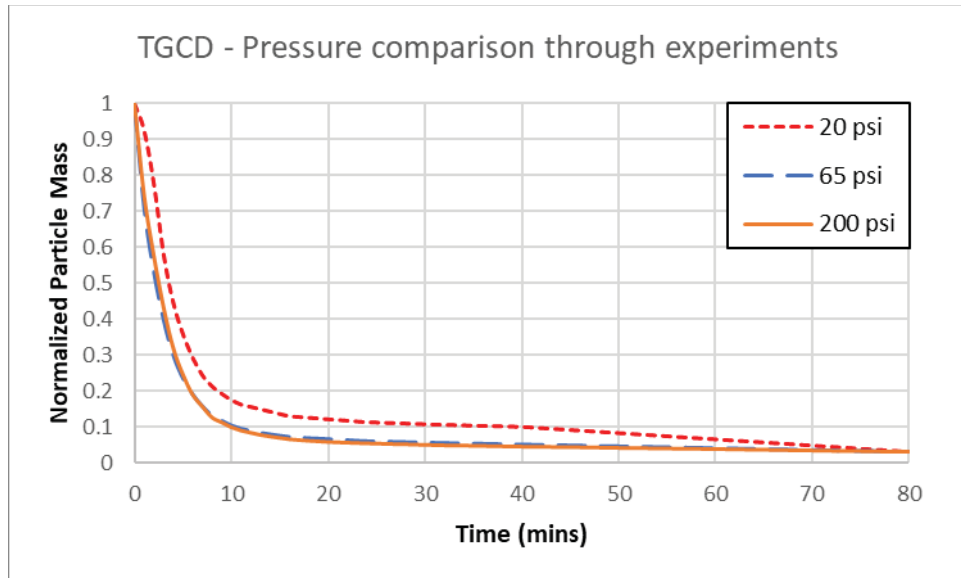


Figure 13: Comparison of effects of varying pressure for TGCD cases obtained from experiments

Figure 14 provides a comparison of CFD results for the normalized particle mass vs. time curves for cases with different pressures, as obtained from CFD simulations.

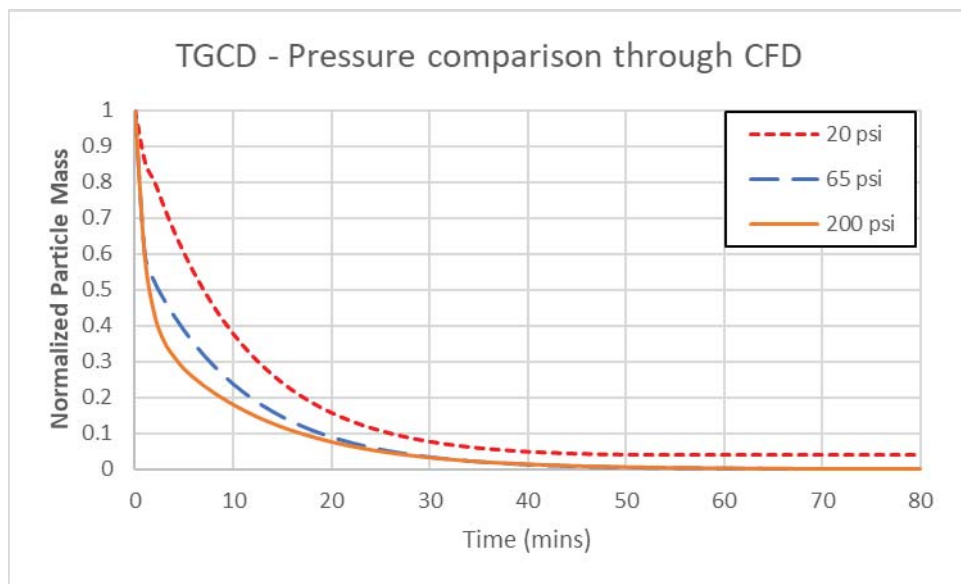


Figure 14: Comparison of effect of varying pressures obtained from CFD

3.6 Comparison of the Effects of Varying A/V ratio in the Absence of Steam (TGC)

Cases 2, 8 and 9 are examined to ascertain the effects of varying A/V ratios in the absence of steam. Figure 15 illustrates the comparison of effects of varying A/V ratios for TGC cases obtained experimentally. Decontamination proceeds at a faster rate with increasing A/V ratios when no steam is present.

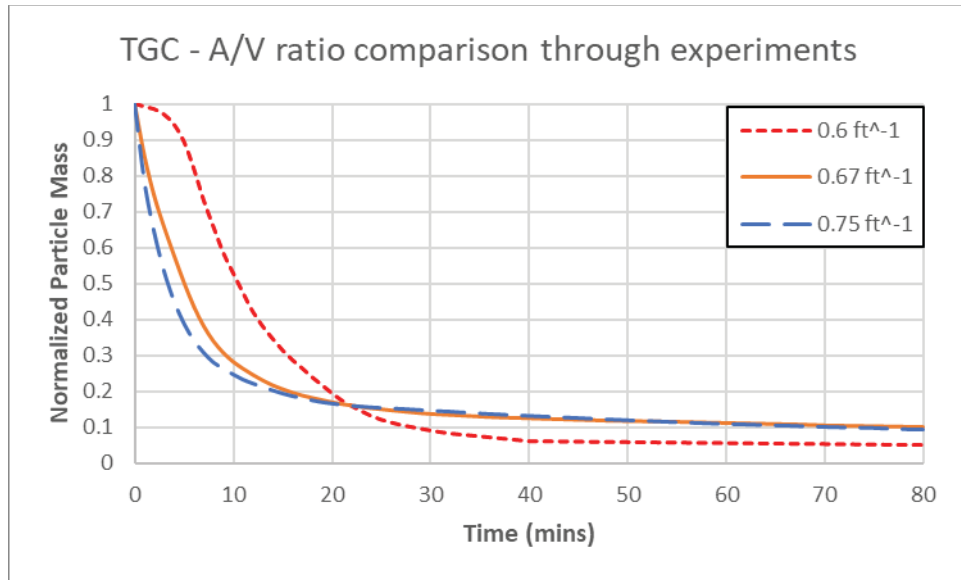


Figure 15: Comparison of effects of varying A/V ratio for TGC cases

3.7 Comparison of the Effects of Varying A/V ratio in the Presence of Steam (TGCD)

Cases 5, 10 and 11 are examined to ascertain the effects of varying A/V ratios in the presence of steam. Figure 16 illustrates the comparison of effects of varying A/V ratios for TGCD cases obtained experimentally.

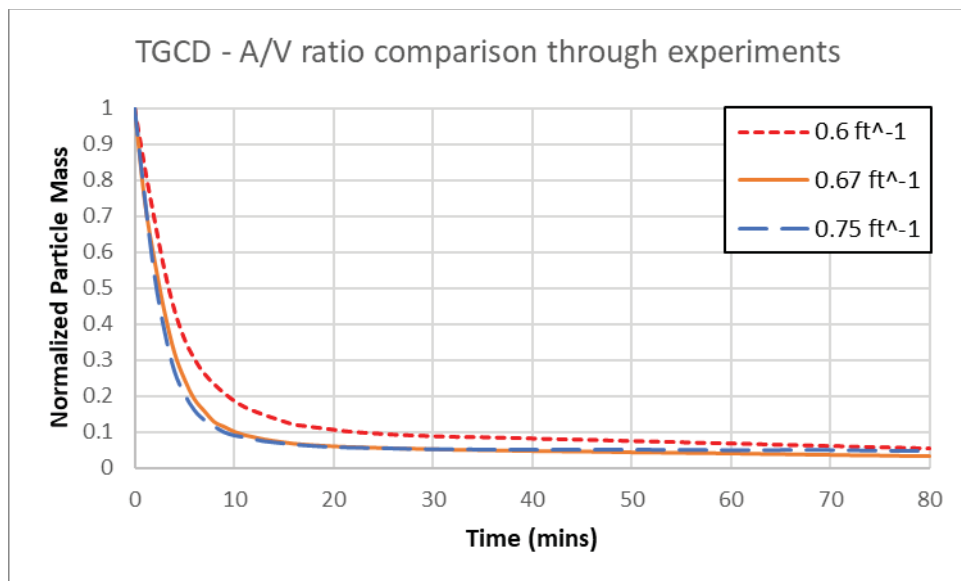


Figure 16: Comparison of effects of varying A/V ratio for TGCD cases obtained experimentally

Figure 17 shows a comparison of CFD results for normalized particle mass vs. time curves for cases with different A/V ratios and shows that the decontamination rate increases with increasing A/V ratios.

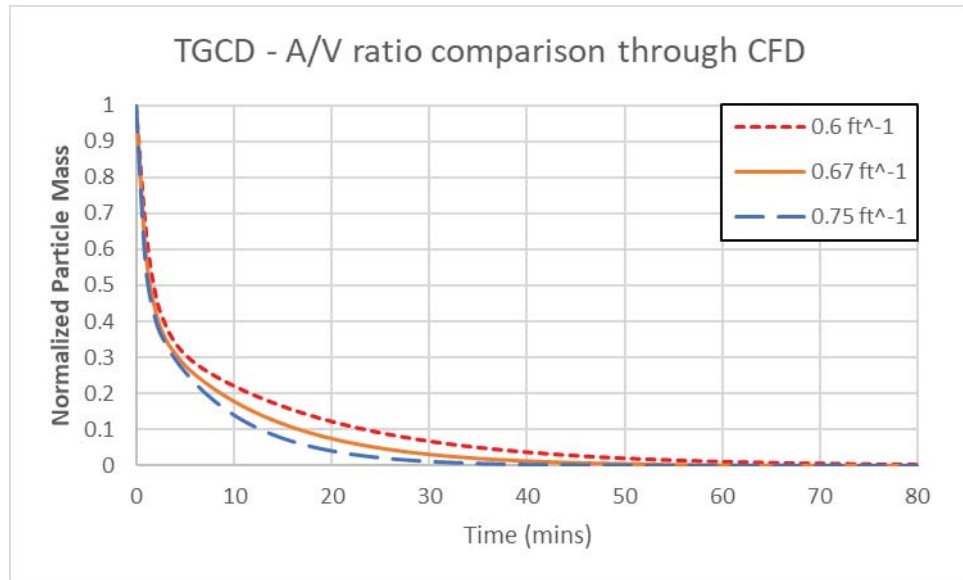


Figure 17: Comparison of effects of varying A/V ratio obtained from CFD

3.8 Additional Estimates of Aerosol Deposition Rates Performed by CFD Simulations

CFD simulations were run for three A/V ratios outside the experimental testing range: 0.14 ft^{-1} , 0.38 ft^{-1} and 0.43 ft^{-1} (while the A/V ratios in the current testing range are 0.6 ft^{-1} , 0.67 ft^{-1} and 0.75 ft^{-1}). All other parameters remained the same as the baseline TGCD case 5. These results were compared to the cases from the current study with varying A/V ratios (cases 5, 10, 11). As expected, decontamination proceeds at a faster rate as the A/V ratio increases. This comparison is shown in Figure 18.

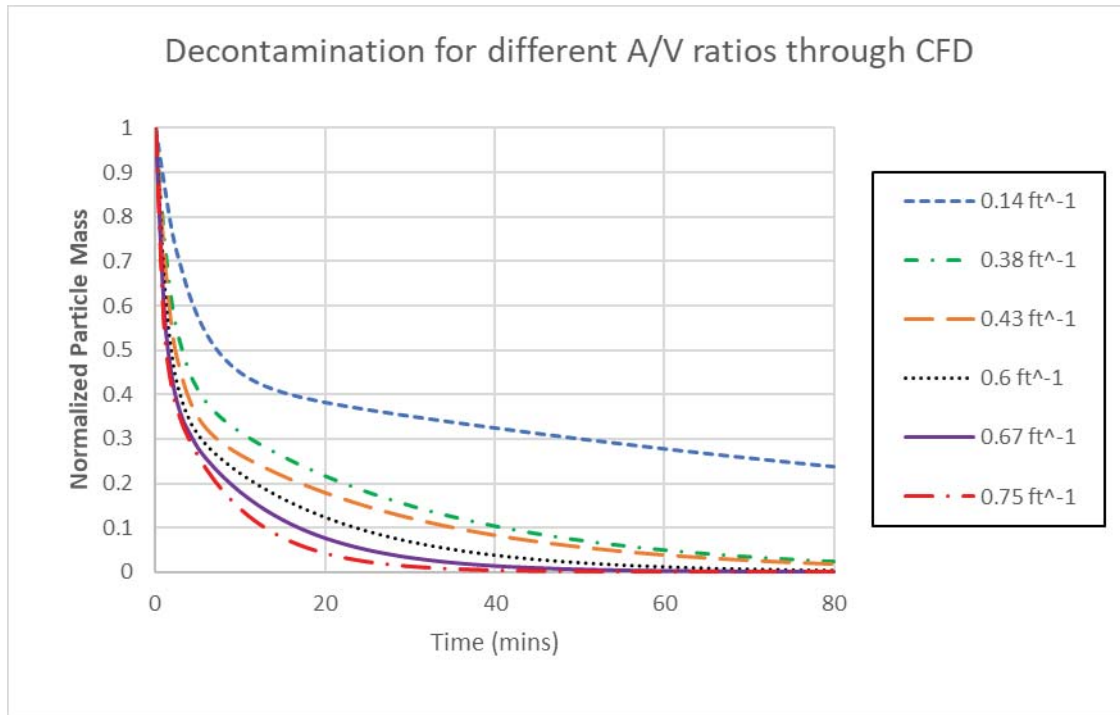


Figure 18: Comparison of effects of varying A/V ratio obtained from CFD simulations (TGCD, outside testing range)

3.9 Comparison of Decontamination Rates with Varying Particle Diameter

The effectiveness of G, TGC and TGCD respectively was examined for three different particle diameters: 1, 6 and 10 μm . Figure 19 shows that gravitational settling (G) increases with increasing particle diameter. Figure 20 shows increasing deposition rates due to the combined effect of thermophoresis, gravitational settling and convective flow (TGC) with increasing particle diameters. Figure 21 shows further increase in deposition rates with the inclusion of steam, which introduces diffusiophoresis (TGCD). The extent to which decontamination is enhanced for 1 μm particles in the presence of steam is much higher than the enhancement in the decontamination of 6 and 10 μm particles.

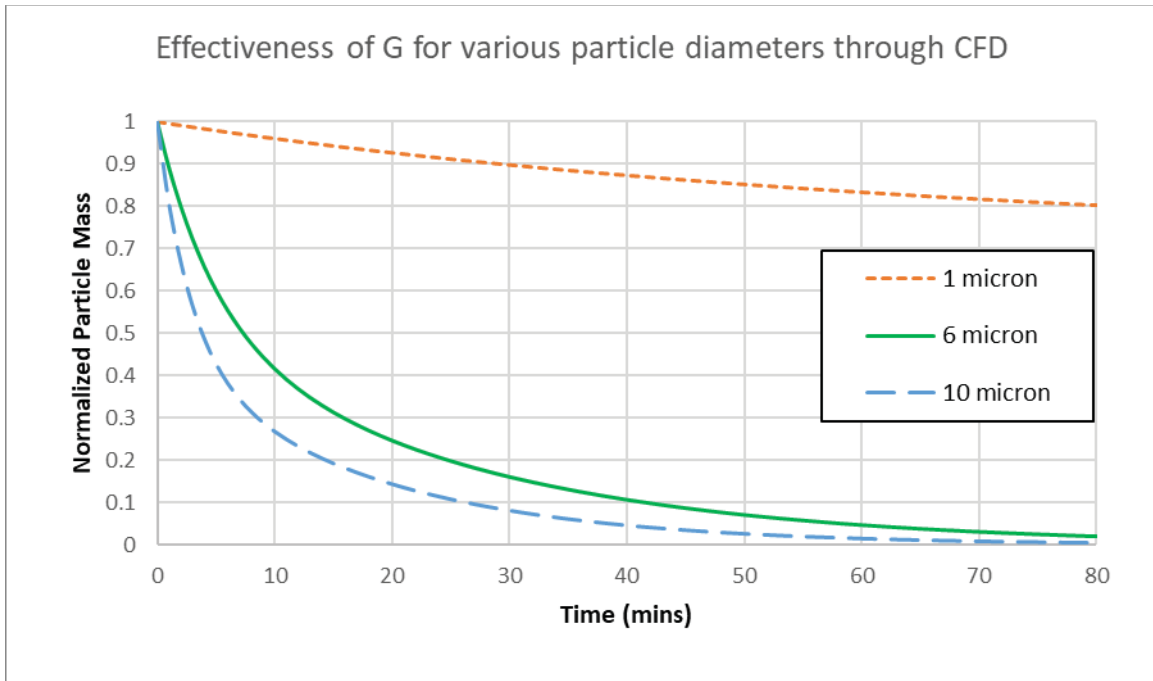


Figure 19: Comparison of CFD results for gravitational settling effectiveness vs. particle diameter

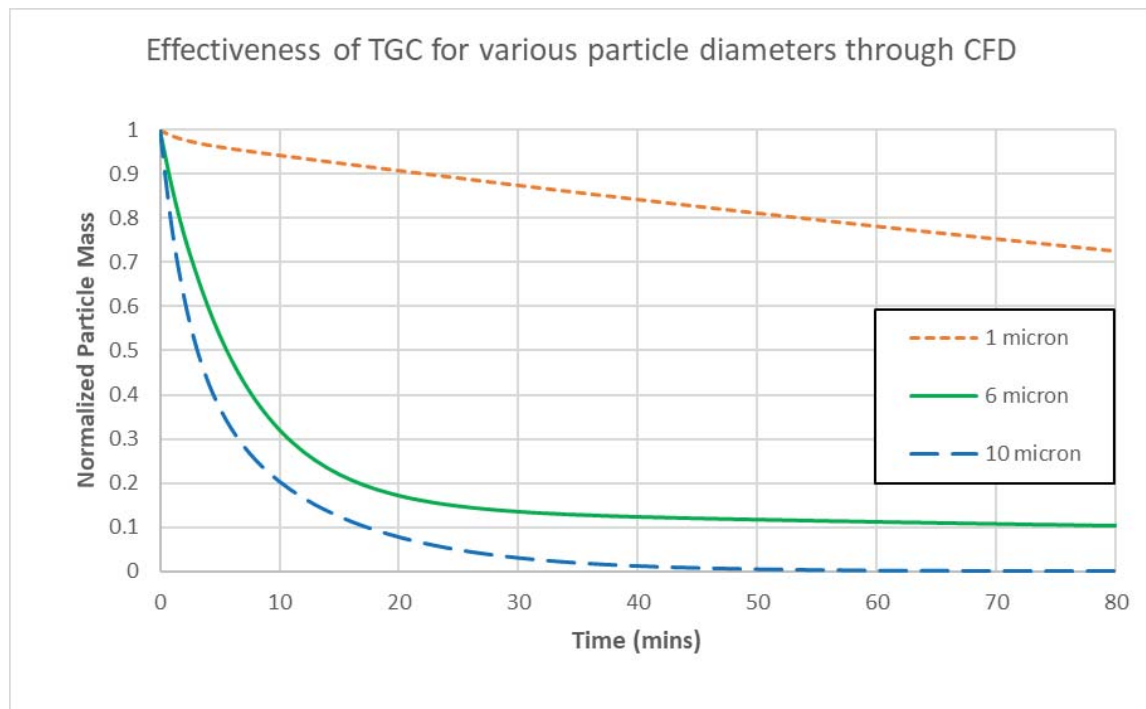


Figure 20: Comparison of CFD results for TGC effectiveness vs. particle diameter

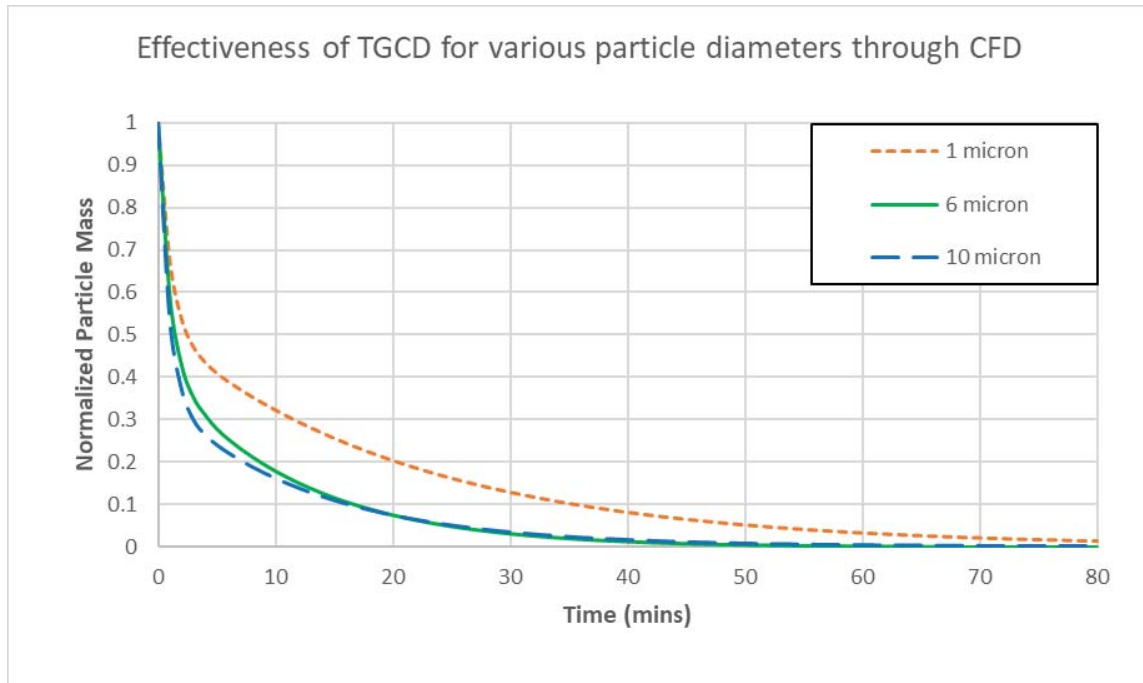


Figure 21: Comparison of CFD results for TGCD effectiveness vs. particle diameter

3.10 Comparison of Experimental and CFD Results

Figure 22 shows a comparison of experimental results to the CFD results for gravitational settling (case 1). It can be seen that the experimental curve follows the 10 μm particle curve initially, before the rate of decontamination slows down. Instead of using a representative particle diameter to characterize overall decontamination due to gravitational settling, a weighted average of the decontamination curves for all particle diameters can be used to model the experimental curve. The weighted average curve is as shown in Figure 23 and it compares better with the experimental result than any of the curves for individual particle diameters.

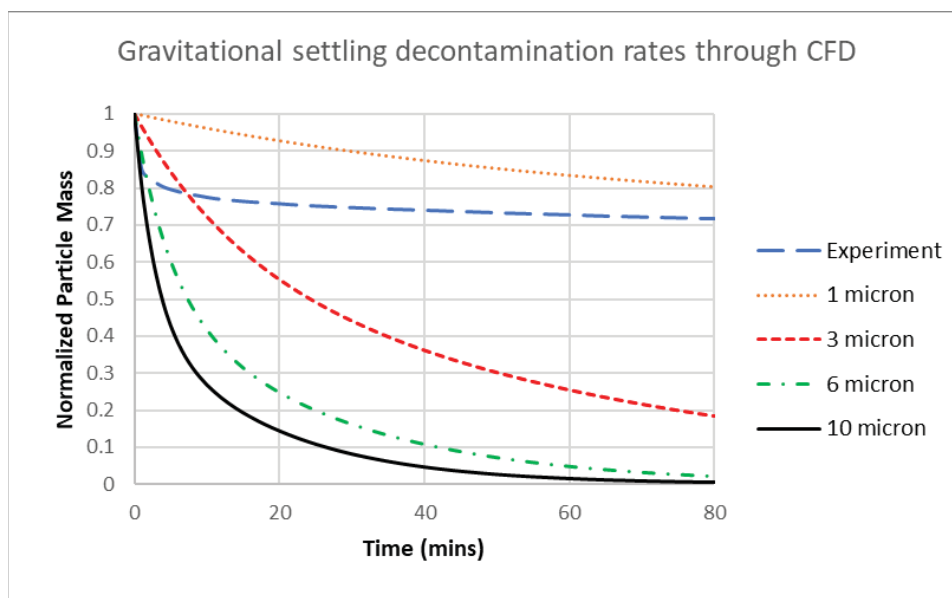


Figure 22: Comparison of decontamination rate curves from Experiments and CFD Simulations for Case 1

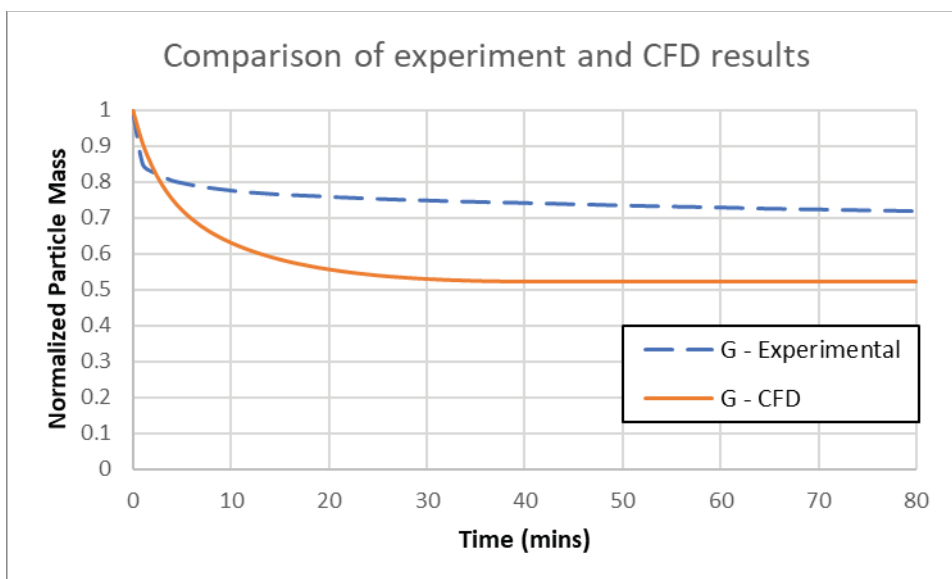


Figure 23: Weighted average curve for gravitational settling

Figure 24 and Figure 25 show the comparison of experimental results to the CFD results for the TGC and TGCD baseline cases (cases 2 and 5) respectively. CFD results predict slightly faster decontamination than experimental results for the TGCD case.

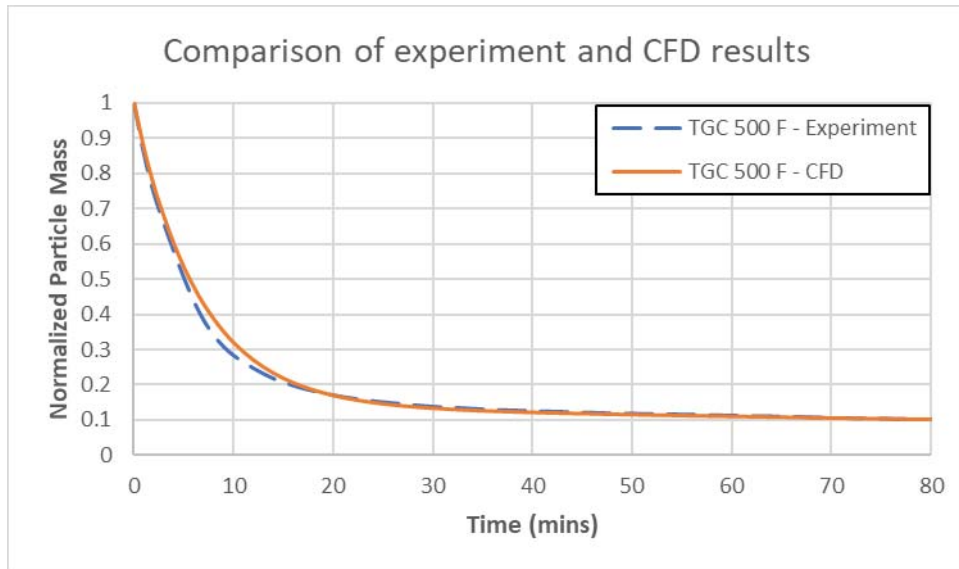


Figure 24: Comparison of decontamination rate curves from Experiments and CFD Simulations for Case 2 (TGC)

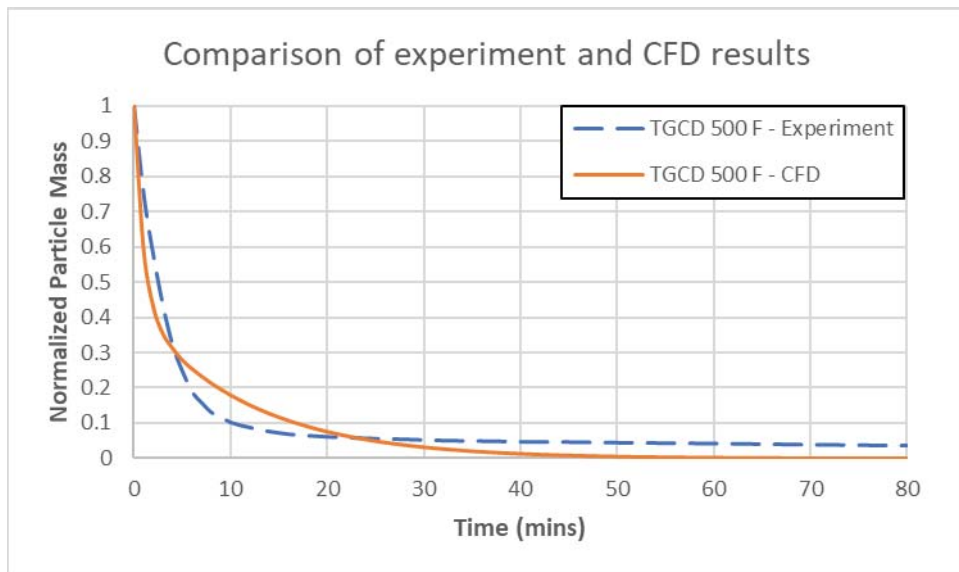


Figure 25: Comparison of decontamination rate Curves from Experiments and CFD Simulations for Case 5 (TGCD)

4 Discussion of results

This section provides a discussion of significant results. Note that Appendix E states additional observations made over the course of this study, which provide supplemental requirements that may be used to improve aerosol deposition codes.

4.1 Establishing the Significance of Convective Flow

Convective flow is identified as a potential key phenomenon based on the comparison of the G – gravitational only case (case 1), TGC – baseline case for thermophoresis, gravitational and convective flow (case 2) and TGCD, which is the baseline case for diffusiophoresis (case 5).

The presence of convective flow is demonstrated by a comparison of case 1 (without a thermal gradient) and case 2 (with a thermal gradient), which shows that the inclusion of a thermal gradient significantly increases the deposition rate. A thermal gradient in a dry environment activates thermophoresis and convective flow (EPRI, 2017a). The increase in decontamination may be largely attributable to convective flow since the estimated deposition rate due to gravitational settling is relatively slow for small particles and the removal rate due to thermophoresis is slower than the gravitational settling rate (EPRI, 2014b).⁵ Therefore, the primary effect of the thermal gradient is convective flow.

Figure 26, which shows the sensitivity of gravitational settling to particle diameter, explains the relatively slow deposition rate observed for gravitational settling (Figure 2). The larger particles, which are up to two-orders of magnitude faster than the slower particles, are removed from the volume relatively quickly, after which the smaller particles are removed slowly as suggested by the deposition velocities in Figure 26.

⁵ The Phase 1 part of this study provides estimated deposition velocities for thermophoresis, diffusiophoresis and gravitational settling.

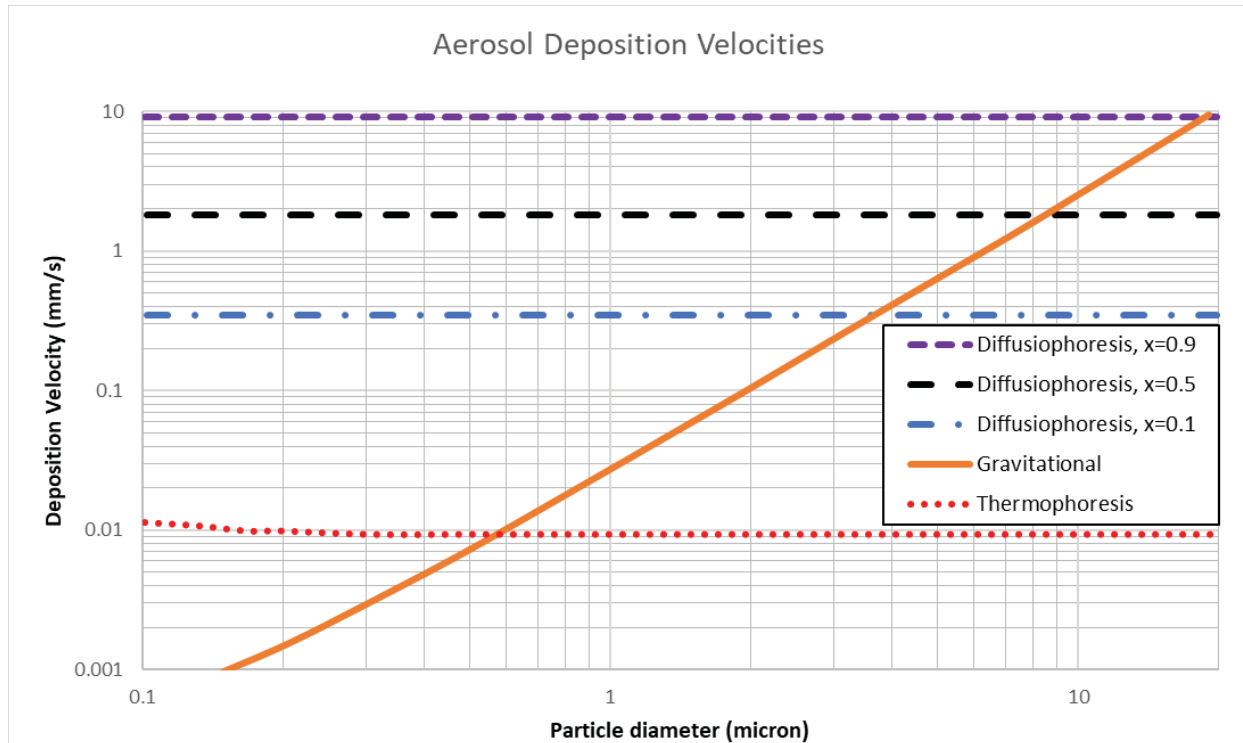


Figure 26: Aerosol deposition velocities associated with various phenomena and conditions (EPRI, 2014b)

4.2 Effects of Varying Temperature Gradient in the Absence of Steam

A parametric evaluation of the effects of varying RV and fluid temperatures was performed. The expected effect of higher RV and fluid temperatures is higher aerosol removal rates, due to higher thermal gradients, which makes both the convective flow and thermophoretic force stronger. This trend is expected in both the presence and absence of steam. Investigation of the expected trend is based on data from the current experimental study, data from prior experiments and CFD simulations for the current study.

Figure 7 provides data from the current study that shows that as RV temperature increases, the decontamination rate increases. The difference in the decontamination rates becomes more apparent as time increases. Data from the ABCOVE program was used for comparison and further evaluation of expected trends (Figure 8). The difference in decontamination rates is assumed to be attributable to the thermal gradients for each test. The temperature gradient is strongest in test AB5, followed by tests AB6 and AB7. This result agrees with the results from the current study, as shown in Figure 7.

An examination of CFD results (Figure 9) shows that the inclusion of a temperature gradient creates a buoyancy-driven convective flow and enhances deposition rates along with the thermophoretic effect. Hence, it follows that the aerosol deposition rate will increase as the thermal gradient increases.

4.3 Effects of Varying Temperature Gradient in the Presence of Steam

The effects of varying temperature gradient in the presence of steam were examined by comparing cases 5, 6 and 7. The experimental data, shown in Figure 10, agrees with the general trend observed for the cases with no steam. A higher temperature difference between the RV and CV walls ($\Delta T = T_{RV} - T_{CV}$) gives rise to steeper temperature and steam concentration gradients, indicating stronger thermophoresis and diffusiophoresis respectively. This is particularly noticeable as the RV temperature approaches 500°F cases. The CFD assessment of the effect of steam inclusion (Figure 11) supports the trend of the experiments with higher deposition associated with higher temperature and steam gradients.

4.4 Comparison of Effects of Varying Pressure

The effect of pressure on particle decontamination is similar for steam and no-steam conditions. Cases 2, 12 and 14 examined the effects of pressure in the absence of steam (Figure 12). Cases 5, 13 and 15 examined the effects of pressure in the presence of steam (Figure 13). Theoretically, higher overall pressure leads to a steeper steam concentration gradient. A similar conclusion has been presented in the report by the Nuclear Energy Agency (NEA, 2009).

The experimental results for the assessment of the effect of pressure in the presence of steam suggests that decontamination is slower at lower pressures; however, the differences are minimal between the 65 and 200 psi cases. The CFD results (Figure 14) also demonstrate that the decontamination rate decreases with decreasing pressure.

The experimental results for the assessment of the effect of pressure in the absence of steam (Figure 12) indicate that pressure has an effect on the deposition mechanisms. At lower pressures (20 psi), decontamination is slower than at higher pressures (65 psi and 200 psi).

4.5 Effects of Varying A/V Ratio

TGC cases 2, 8 and 9 examined the effects of varying A/V ratios in the absence of steam, and TGCD cases 5, 10 and 11 examined the effects of varying A/V ratios in the presence of steam. In general, the effects of varying A/V ratio results in faster deposition with increasing A/V ratios for both the TGC and the TGCD cases. The CFD model also predicts that the deposition rate will increase as the A/V ratio increases.

The Phase 1 part of the current study, demonstrated that containment vessels for iPWRs, with relatively high deposition surface-area-to-volume ratios, are capable of significantly higher post-accident aerosol deposition rates (EPRI, 2014b). This is due to the increased effectiveness of natural deposition phenomena within the thermal-hydraulic and geometric parameters of these plant designs.

Figure 15 presents results from the current set of experiments, for the effects of varying A/V ratio on particle decontamination, for the same pressure and temperature in the absence of steam. It is observed that decontamination proceeds at a faster rate with increasing A/V ratios. It should be noted that the smallest A/V ratio case (0.6 ft^{-1}), which has the largest volume shows a relatively slower start at the

beginning of the decontamination process. This may be due to the larger volume, which results in slower gas flow velocities associated with convective flow.

For the experimental TGCD cases, the decontamination rate increases as the surface-area-to-volume ratio increases, as shown in Figure 16. The CFD model also predicts that the deposition rate increases as the A/V ratio increases, as shown in Figure 17.

4.6 Comparison of Decontamination Rates with Varying Particle Diameter

A review of Figure 19 to Figure 21 shows that the higher deposition rates are associated with larger particle sizes. This trend can be seen for the different deposition mechanisms. Figure 19 shows that gravitational settling (G) increases with increasing particle diameter. Figure 20 shows increasing deposition rates for the combined effect of thermophoresis, gravitational settling and convective flow (TGC) with increasing particle diameters. Figure 21 shows that the inclusion of steam, which introduces diffusiophoresis has a significant effect on particle deposition, which is more significant for smaller particles.

4.7 Comparison of Experimental and CFD Results

Phase 2b demonstrated that experimental and simulated results can be compared to better understand deposition rates for three areas: (1) identification of particle size influence during gravitational settling, (2) incorporation of experimental data in CFD models for more precise fluid buoyancy modeling, and (3) identification of potential enhancements to CFD models based on experimental data.

Review of gravitational settling (case 1) experimental results supported the observation that experimental loss of larger particles occurred in the test vessel supply line.⁶ The average particle size showed a reduction from an average of 5.23 μm to 4.98 μm between introduction into and exit from the containment vessel supply lines. CFD decontamination curves for various particle sizes illustrated that the experimental curves initially follow the 10 μm particle curve before the rate of decontamination slows down. Examination of this case using experimental data and CFD models demonstrated that a weighted average of particle diameters offers greater granularity than using representative particle diameters to characterize overall decontamination due to gravitational settling.

The CFD model was calibrated to account for fluid buoyancy and particle suspension, by modifying the drift-flux model (EPRI, 2017b). A change was made to the gravitational settling velocity (V_g) equation, whereby V_g is calculated by equating gravitational force to the sum of the viscous drag and the buoyant force which acts on the particle due to the displacement of the fluid. This allowed the inclusion of the effects of fluid buoyancy on the particle, based on the following equation (Mitchell, 1995):

⁶The experiments included an assessment of potential loss in the vessel supply lines. The assessment showed that the average particle size reduced from 5.23 μm to 4.98 μm , however the size range was maintained at 1 to 10 μm .

$$V_g = \frac{C_c(\rho_p - \rho_g)d_p^2g}{18\mu_g}$$

Where C_c is the Cunningham Slip factor, ρ_p and ρ_g are particle and fluid densities respectively, d_p is particle diameter, and μ_g is fluid viscosity.

CFD results predict slightly faster decontamination for the TGCD case when comparing experimental results to CFD results for the TGC and TGCD baseline cases (cases 2 and 5), respectively. The difference may be attributed to differences in the particle distribution as some particles may be lost in the test vessel supply line. Enhanced CFD modeling could address this issue.

4.8 CFD Model Comparison with Results from Relevant Prior Experiments

To further validate the CFD model, CFD results were compared against prior experimental results from the Phebus test and another aerosol decontamination estimation code, MELCOR which is a computer code developed by Sandia National Laboratories to model the progression of severe nuclear power plant accidents and to estimate aerosol source terms. A prior validation exercise that compared MELCOR results to data from the Phebus test is referenced (Birchley, 2004). The Phebus test was selected because of relatively similar test conditions including an A/V ratio for the Phebus test vessel of 0.55 ft⁻¹, which is similar to the experimental A/V ratios (0.6 ft⁻¹ to 0.75 ft⁻¹). Other Phebus test parameters are stated in Table 5.

Table 5: Experimental Parameters for the Phebus test

Parameter	Value
Fluid Temperature	157-177°C (314.6-350.6°F)
CV wall Temperature	110°C (230°F)
Steam concentration	35.4% by volume (26% by mass)
Pressure	2 bar (29 psi)
Particle Size	3.5 μm
Aerosol Concentration	6.5 g/m ³
A/V Ratio	0.55 ft ⁻¹

Figure 27 shows a comparison between the Phebus experimental results, a MELCOR simulation, and a CFD simulation with the model developed as part of the current study, for the Phebus test conditions stated in Table 5. A comparison is made against the MELCOR code because both MELCOR and CFD use the discrete approach, in which transport equations are solved. The MELCOR analysis was performed in the referenced work (Birchley, 2004) using MELCOR 1.8.5. The CFD results show fairly good agreement with the Phebus test results.

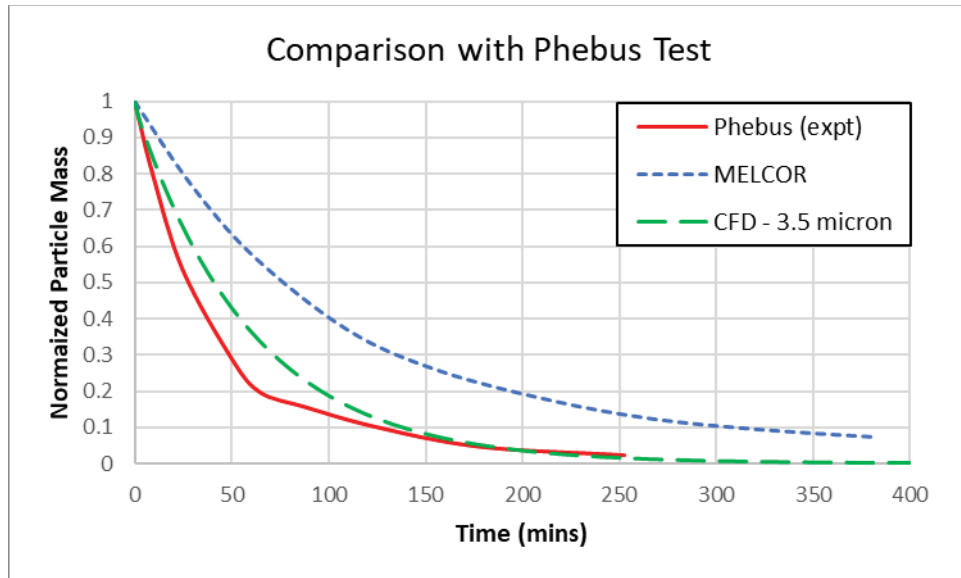


Figure 27: Comparison of results from the current study and the Phebus test for similar particle diameters (NRC, 2014)

4.9 In-line Loss Characterization Test

The potential for particle loss in the vessel supply line was investigated. This investigation was conducted to ensure that there was not a significant amount of deposition occurring in the vessel supply lines, which could invalidate the assumptions for the particle size in the vessel. The particle size distribution and average particle size were measured before introduction into the line and at the exit from the line, just before entry into the vessel. The average of three tests showed that the average particle size before and after introduction were 5.23 and 4.98 μm over a 1 to 10 μm range. Considering the size distribution is maintained, the amount lost is considered to be insignificant because all sizes were still represented in the distribution. The tests also confirmed that the particle charge neutralizer was functioning; the average particle size at the exit without the charge neutralizer was 4.36 μm .

4.10 Vessel Wall Impaction Test

A test was conducted to determine the potential for impaction-related losses on vertical surfaces due to convective flow. Two tests were conducted; one in dry conditions and the other with steam. The dry condition test was carried out during performance of the base case 2 test, with conditions at 200 psi and 500°F with no steam (TGC). The wet case was carried out during performance of base case 5, with conditions at 200 psi, 500°F and 70% steam concentration (TGCD). The test results showed no measurable wall deposition for the dry tests, while the wet test showed 2 milligrams/in² deposited after drying the test sample. This demonstrates that there is impaction occurring and that the steam environment supports adhesion.

5 Application of Results: Scaling

This section provides guidance on scaling critical aerosol decontamination parameters developed from the current study. The information in this section provides guidance on how to apply the results from this study to specific design conditions, which may include different geometries and thermal-hydraulic conditions.

The decontamination factor, which is used in safety analysis, is calculated from the aerosol removal rate. The method for development of correlations assumes that there is a correlation between the removal rate (also known as the aerosol removal rate coefficient) λ and the suspended mass concentration (EPRI, 2008). Hence, experiments such as those performed in this study, which measure mass concentrations over a period, can be correlated by evaluating λ at various times as the logarithmic derivative of the mass concentration. A plot of λ versus the concentrations provides the correlation.

The CFD method used in this study improves the estimation accuracy of aerosol deposition by modeling both the aerosol characteristics and the thermal-hydraulic environment. The aerosol characteristics are defined by the particle size and density, while the environment is described by the temperature, pressure and steam concentration. Table 6 lists the critical scaling parameters applicable to these thermal-hydraulic parameters and shows that actual post-accident aerosol characteristics and environmental conditions were used based on applicable NRC guidance documents including NUREG/CR-6189 and NRC Reg. Guide 1.183. The use of actual conditions allows direct application of experimentally-derived aerosol removal rates to be applied to established PWR aerosol removal correlations. This can be achieved by addition of the new aerosol removal rate coefficients to coefficients in existing correlations. Additionally, this study indicates the significance of convective flow as an aerosol removal mechanism. This section also describes how the effects of convective flow on particle transport and deposition can be implemented through turbulence and impaction aerosol removal rates.

Table 6: Critical Scaling Parameters

Parameters	Scaling Ratio to iPWR	Test Values
Aerosol Parameters		
Particle Density (g/cm ³)	1:1	8.9
Particle Concentration (g/m ³) ⁷	1:1	10
Particle Size and Distribution (μm)	1:1	1 – 10
Geometric Parameters		
Area (ft ²)	1:x	168.47
Height (ft)	1:x	8
Volume(ft ³) ⁸	1:x	279.11, 249.63, 222.59
Surface-Area-to-Volume Ratio (ft ⁻¹)	1:1	0.60, 0.67, 0.75
Operating Parameters		
Steam mass fraction	1:1	0.7
Temperature (°F)	1:1	325 to 500
Pressure (psi)	1:1	20 to 200
Time (hours)	1:1	0 – 12

⁷ For the purpose of scaling, particle concentration is converted to the massless number concentration which is particle number density ($n(v_p, t)$).

⁸ Volume and Surface-Area-to-Volume Ratio depend on experimental facility reactor vessel insert sizes.

5.1 Aerosol Scaling

As indicated in Table 6, the critical aerosol parameters required for scaling are (1) particle concentration, which for scaling purposes, is described in terms of particle number density ($n(v_p, t)$), (2) particle size and distribution (often characterized as particle diameter or particle volume, v_p) and (3) time (t), which is relevant for all parameters. There are two additional parameters that are derived from these basic parameters, which are used as measures of the decontamination process: (1) particle mass density (m) and (2) decontamination or aerosol removal rate (λ). Dimensionless scaling factors for aerosol parameters can be defined by using physical properties of the particles and the fluid, as well as dynamic constants. It is assumed that the particle deposition velocity (u) follows a power law with respect to particle volume (v_p), as stated in the following equation (Sher & Hobbins, 2011):

$$u(v_p) = Bv_p^b$$

The parameters B and b are constants applicable to specific deposition mechanisms. The three main aerosol parameters ($n(v_p, t)$, v_p , t) have dimensionless quantities associated with them, namely, ($N(V, \tau)$, V , τ). Using constants (c_1 , c_2 , c_3), the dimensionless quantities can be defined for each of the aerosol parameters.

$$N(V, \tau) = \frac{n(v_p, t)}{c_1}$$

$$V = \frac{v_p}{c_2}$$

$$\tau = \frac{t}{c_3}$$

Evaluation of c_1 , c_2 , c_3 uses the Boltzmann constant (k_B), the particle material density (ρ_p), gas viscosity (μ_g), the normalized agglomeration kernel ($K_0 = \frac{4k_B T}{3\mu_g}$); and the effective height of the aerosol volume (H).

Expressions for c_1 , c_2 , c_3 are determined as follows:

$$c_1 = \frac{B}{K_0 H} \left(\frac{g \rho_p}{\mu_g K_0} \right)^{\left(\frac{3}{4(1-b)} \right)}$$

$$c_2 = \left(\frac{K_0 \mu_g}{g \rho_p} \right)^{\left(\frac{3}{4} \right)}$$

$$c_3 = \left(\frac{H}{B} \right) \frac{g \rho_p}{(\mu_g K_0)^{\frac{3b}{4}}}$$

The constants c_1 , c_2 and c_3 can thus be evaluated for a certain set of conditions, in order to calculate the dimensionless versions of the critical aerosol parameters. These dimensionless parameters are used to further evaluate other parameters like the aerosol removal rate (λ) and the particle mass density (m), which describe the aerosol behavior during post-accident conditions inside the containment vessel; this process is discussed in more detail in the subsequent section.

The general aerosol deposition equation can be written in a dimensionless form as:

$$\frac{\partial N(V, \tau)}{\partial \tau} = \frac{1}{2} \int_0^V \theta(V', V - V') N(V, \tau) N(V - V', \tau) dV' - \int_0^\infty \theta(V', V) N(V', \tau) N(V, \tau) dV' - \frac{1}{2(9\pi)^{\frac{1}{3}}} V^{\frac{2}{3}} N(V, \tau)$$

θ is the dimensionless coagulation coefficient, given by:

$$\theta(V', V) = \frac{1}{2} \left[V^{\frac{1}{3}} + (V')^{\frac{1}{3}} \right] \left[V^{-\frac{1}{3}} + (V')^{-\frac{1}{3}} \right] + \frac{1}{2(9\pi)^{\frac{1}{3}}} \varepsilon(V', V) \left[V^{\frac{1}{3}} + (V')^{\frac{1}{3}} \right]^3 \left[(V')^{\frac{1}{3}} - V^{\frac{1}{3}} \right]$$

Note that $\varepsilon(V', V)$ is the gravitational agglomeration efficiency, while V and V' represent particle volumes. Based on this equation, the dimensionless particle number density ($N(V, \tau)$) can be evaluated to provide a measure of particle concentration inside the system.

5.1.1 Scaling Factors for Critical Parameters

As discussed in the previous section, critical aerosol parameters can be described in a non-dimensional form when the deposition velocity follows a power law. These dimensionless versions can be further used in the evaluation of scaling factors for other important parameters such as dimensionless particle mass density (M) and dimensionless aerosol removal rate/decontamination coefficient (Λ).

Epstein et al. (Epstein, Ellison, & Henry, 1986) provide expressions for the scaling factors for dimensionless time (τ), dimensionless particle mass density with respect to the height of the containment vessel (M), and dimensionless decontamination coefficient (Λ) in terms of the original aerosol parameters i.e. time (t), particle mass density (m) and the decontamination coefficient (λ), as follows (NRC, 1996):

$$\tau = \left(\frac{\mu_g K_0}{\gamma \varepsilon_0 g \rho_p} \right)^{\left(\frac{1}{2}\right)} \left(\frac{B}{H} \right) t$$

$$M = \frac{\gamma K_0 H C(p)}{\chi \rho_p B} \left(\frac{\gamma \varepsilon_0 g \rho_p}{\mu_g K_0} \right)^{1.25} m$$

$$\Lambda = \left(\frac{\gamma \varepsilon_0 g \rho_p}{\mu_g K_0} \right)^{\left(\frac{1}{2}\right)} \left(\frac{H}{B} \right) \lambda$$

The above expressions use additional parameters such as the particle settling shape factor (χ) and collision shape factor (γ) (Epstein, Ellison, & Henry, 1986), as well as a parameter to indicate the uncertainty in the efficiency of gravitational coagulation (ε_0) (NRC, 1996). Using these expressions, aerosol decay can be characterized for both steady state and transient state. Steady state is defined as the conditions after sufficient passage of time in which the rate of aerosol deposition is equal to the source rate. Transient state is defined as aerosol decay after the source has been cut off. The dimensionless particle mass density (M) can be expressed in terms of dimensionless time (τ) for a transient state, as follows (Sher & Hobbins, 2011):

$$M(\tau) = 74.24\tau^{-3.05}(1 + 3.74\tau^{-1.12})^{-1.70}$$

Similar expressions can be derived for the dimensionless decontamination coefficient (Λ) for steady and transient states. The transient state is relevant to the current effort given the focus of the study is the post-pressurization aerosol depletion period. The transient equation for the dimensionless decontamination coefficient is as follows (NRC, 1996):

$$\Lambda(M) = 0.528M^{0.235}(1 + 0.473M^{0.754})^{0.786}$$

5.1.2 Inclusion of the Effects of Convective Flow with Aerosol Removal Rates for Turbulence and Impaction

Turbulence: To account for the effects of convective flow, NRC NUREG/CR-6189 identifies the applicability of the aerosol removal rates for turbulent diffusion. Considering turbulence effects, the dimensionless decontamination coefficient for the transient state is given by the following equation:

$$\Lambda(M) = (4.06 \times 10^{-3})M^{0.512}(1 + 3070M^{1.106})^{0.397}$$

Impaction: Aerosol deposition due to inertial impaction, which is the resultant of convective flow impingement on deposition surfaces has the following dimensionless decontamination coefficient:

$$\Lambda(M) = 0.337M^{0.21}(1 + 1.74M^{1.9})^{0.14}$$

5.1.3 Implementation Approach

Implementing the similitude approach requires the following actions to be performed.

- Calculate the non-dimensional scaling factor for time (t) and the corresponding dimensionless time (τ).
- Calculate the dimensionless particle mass density (M) and dimensionless decontamination coefficient (Λ).
- Evaluate the scaling factors for particle mass density (m) and decontamination coefficient (λ) using the required values of the thermal-hydraulic and aerosol parameters.
- Scale the non-dimensional parameters to provide the required results for $M(\tau)$ and $\Lambda(M)$.
- Perform a vector summation of the applicable removal coefficients, which include turbulence and impaction coefficients.

5.2 Thermal-Hydraulic Scaling

The similitude approach can also be used for the scaling of mixing and thermal stratification (Cai, et al., 2013). To employ the similitude approach, the dimensionless vessel height (z^+) and diameter are the base parameters from which correlations for dimensionless time, volume flow rate (Q_0), jet fluid velocity (U_0) and diameter of the flow source are developed for scaling.

Using the mass-energy conservation equation and the momentum equation for upward driven convective flow and non-dimensional thermal parameters, the characteristic time-scale may be described as follows (Cai, et al., 2013):

$$\Pi = \frac{5\alpha_T}{3} Ri^{\frac{1}{3}} (z^+)^{\frac{2}{3}} \left(\frac{H_{sf}}{d_{bj,0}} \right)^{\frac{5}{3}}$$

Where α_T is the Taylor entrainment constant; H_{sf} is the thickness of the stratified fluid, which is calculated from the height of the start of the flow stream to the top; $d_{bj,0}$ is the diameter of the jet⁹, and Ri is the similarity criterion number (or Richardson number), which is defined as follows:

$$Ri = \frac{g d_{bj,0} (\rho_a - \rho_0)}{\rho_a U_0^2} = \frac{16 g d_{bj,0}^5 (\rho_a - \rho_0) \pi^2}{\rho_a Q_0^2}$$

Where ρ_a is the ambient fluid density and ρ_0 is the jet fluid density.

The characteristic time scale has the following critical factors, which include the entrainment constant, the height-to-diameter ratio, density of the ambient fluid and Ri number. It should be noted that of these factors, only the height-to-diameter ratio and Ri number are variable. Hence, if these parameters are constant, the scaling can be performed for stratification and thermal mixing.

A similar approach has been provided in the work by Zhao et al. (Zhao & Peterson, 2010), where a study of computer codes for analysis of thermal mixing and stratification was carried out. An analysis of an injected buoyant jet case was performed in the work, which proposes characterization of thermal mixing and stratification. The applicable parameters are the jet velocity, enclosure height, jet source diameter and the jet Richardson number. The applicable fluid properties include densities of source and ambient fluids. The method assumes the ambient fluid between flow streams and boundary layer flows is homogeneously mixed and hence can be described by a 1-D temperature and fluid concentration distribution. Hence, stratified mixing processes in complex enclosures can be analyzed using 1-D differential equations, with transport streams modeled using 1-D integral models. For application of this method to containment vessels, the detailed geometry becomes unimportant, and only the horizontal cross-sectional area and perimeter are required to be specified as a function of elevation (INL, 2010).

The INL study concludes that results obtained from such an approach are satisfactory and have better accuracy than the 0-D codes as well as better computational efficiency than the 2-D and 3-D codes. In summary, the study indicates that 1-D codes such as the BMIX++ (Berkeley mechanistic MIXing code in C++) (Christensen & Peterson, 2001) can be used to implement an effective scaling methodology for thermal mixing.

⁹A jet is described here as a generic concept for a steady continuous flow in an ambient volume with a dominant flow direction and a length scale much less than the ambient volume's scale (INL, 2010).

6 Application of Results: Estimation of iPWR Decontamination Factors

The Decontamination Factor (DF) for a certain test configuration is defined as the ratio of initial particle mass ($m(0)$) to the time-dependent particle mass ($m(t)$); this is shown according to the following equation (EPRI, 2017a):

$$DF(t) = \frac{m(0)}{m(t)}$$

The DF can also be expressed in terms of the aerosol deposition rate ($\lambda(t)$), given by the following equation (Zhao, Zhang, & Tong, 2015):

$$DF(t) = \frac{1}{e^{-\int_0^t \lambda(t) dt}}$$

The time-dependent particle mass is normalized using the initial particle mass, and this normalized particle mass (N_m) is used as a measure of particle deposition. This quantity is defined as:

$$N_m(t) = \frac{m(t)}{m(0)}$$

Therefore, the relationship between DF and N_m is:

$$DF(t) = \frac{1}{N(t)}$$

$N_m(t)$ is modeled using a double exponential decay curve as:

$$N_m(t) = ae^{-bt} + ce^{-dt}$$

Where a, b, c, d are constants and $b, d > 0$.

$N_m(t)$ is also modeled using a triple exponential decay curve as:

$$N_m(t) = a + be^{-ct} + de^{-ft}$$

Where a, b, c, d, f are constants and $c, f > 0$.

A relationship between N_m and $\lambda(t)$ can be developed, since $\lambda(t)$ and N_m are both related to DF. Using the above equations, the following equation portrays the relationship between N_m and λ :

$$N_m = e^{-\int_0^t \lambda(t) dt}$$

Taking the natural logarithm on both sides,

$$\ln(N_m) = -\int_0^t \lambda(t) dt$$

Differentiating with respect to time on both sides and using the fundamental theorem of calculus,

$$\frac{1}{N_m} \frac{dN_m}{dt} = -\lambda(t)$$

After rearranging, the above equation can also be written as:

$$\lambda(t) = -\frac{1}{N_m} \frac{dN_m}{dt}$$

Thus, the decontamination coefficient can be expressed in terms of the normalized particle mass. Using the double exponential form of $N_m(t)$, the above equation becomes:

$$\lambda(t) = \frac{abe^{-bt} + cde^{-dt}}{ae^{-bt} + ce^{-dt}}$$

Thus, the aerosol decontamination rate can be written only in terms of time.

A better understanding of the time dependence of N_m , DF and λ can be gained by considering an example. The Characteristic Case for particle decontamination is used for this purpose; it is derived by taking the average of the experimental results for all the TGCD (steam) cases together, since they contain the effects of all three deposition phenomena. Curve-fitting was also carried out for the individual TGCD cases. The parameters for the fitted curves are summarized in Table 7, along with the Root Mean Squared Error (RMSE) and the R-Square value to indicate the goodness of the curve fit, a detailed analysis of which has been carried out in Appendix A of this document.

Table 7: Values for N_m using Double Exponential Curve for Characteristic Case and each Test Case

Parameter	Characteristic Case	TC 5	TC 6	TC 7	TC 10	TC 11	TC 13	TC 15
	400, 450, 500 F 20, 65, 200 psi 0.6, 0.67, 0.75 A/V	500 F 200 psi 0.67 A/V	450 F 200 psi 0.67 A/V	400 F 200 psi 0.67 A/V	500 F 200 psi 0.6 A/V	500 F 200 psi 0.75 A/V	500 F 65 psi 0.67 A/V	500 F 20 psi 0.67 A/V
Asymptote	N/A	N/A	0.0424	N/A	N/A	N/A	N/A	N/A
Scale 1	0.111	0.070	0.142	0.136	0.121	0.088	0.069	0.154
Decay Rate 1	0.011	0.008	0.060	0.008	0.009	0.008	0.009	0.014
Scale 2	0.897	0.937	0.808	0.871	0.898	0.916	0.920	0.930
Decay Rate 2	0.281	0.321	0.336	0.184	0.248	0.318	0.374	0.272
Root Mean Squared Error (RMSE)	0.056	0.017	0.052	0.028	0.007	0.022	0.011	0.023
R-Square	0.88	0.99	0.90	0.97	0.99	0.98	0.99	0.98
N/A – Not Applicable (only TC 6 was fit with an asymptote)								

For example, the Characteristic Case equation for $N_m(t)$ is given by (as obtained from Table 7):

$$N_m(t) = 0.111e^{-0.011t} + 0.897e^{-0.281t}$$

Figure 28 shows the Normalized particle mass (N_m) as a function of time for the Characteristic Case.

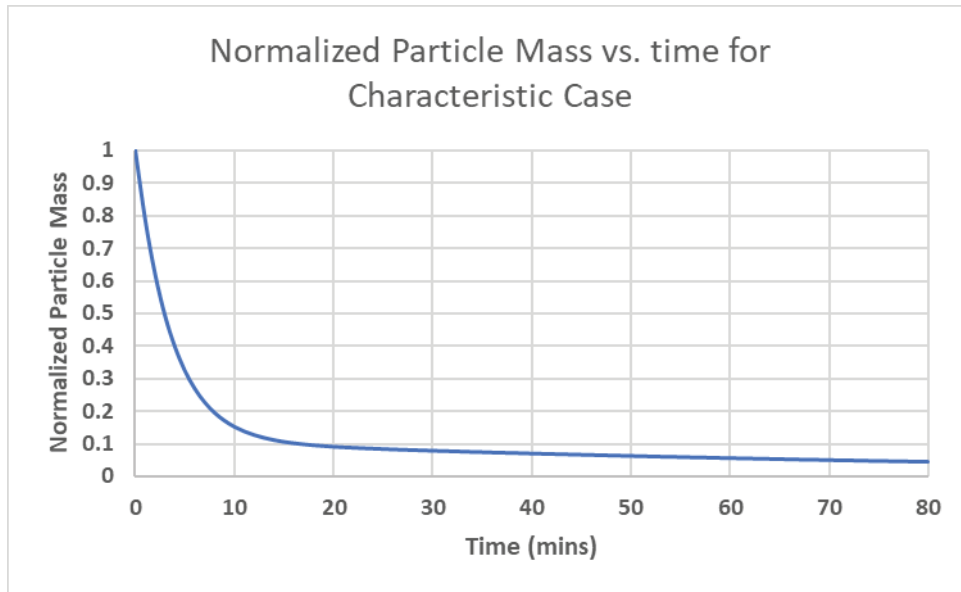


Figure 28: Normalized particle mass vs. time for Characteristic Case

The above equation gives rise to the following equation for $\lambda(t)$ for the Characteristic Case:

$$\lambda(t) = \frac{0.00122e^{-0.011t} + 0.252e^{-0.281t}}{0.111e^{-0.011t} + 0.897e^{-0.281t}}$$

Figure 29 shows the plot of $\lambda(t)$ against time for the Characteristic Case. The aerosol decontamination rate decreases with increasing time, before becoming asymptotic at a certain value which can be evaluated after taking the limit of $\lambda(t)$.

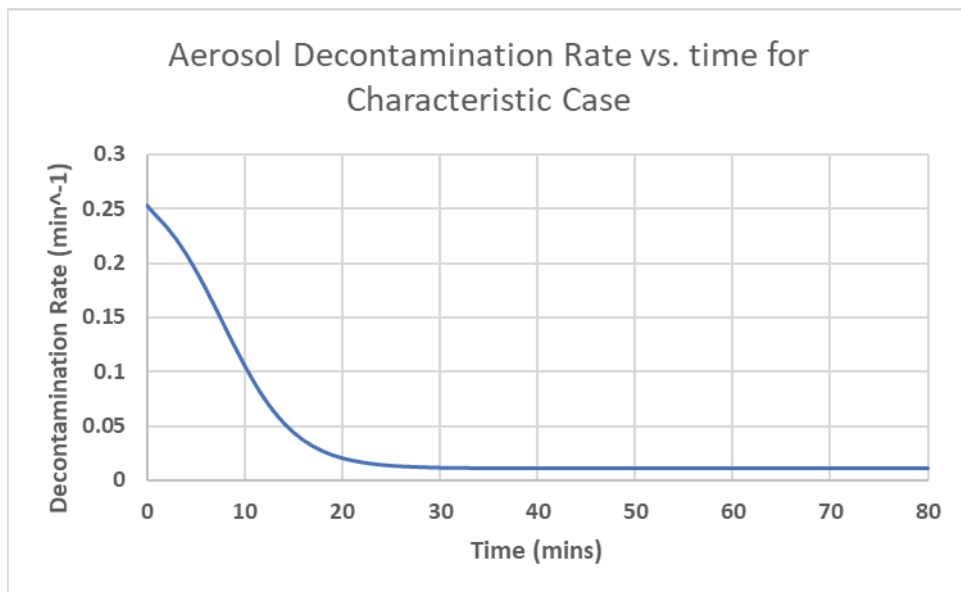


Figure 29: Aerosol decontamination rate vs. time for Characteristic Case

The equation of N_m also allows calculation of DF and decontamination efficiency ($DE = 1 - N_m$); both are as shown in Figure 30 and Figure 31. As expected, the DF shows an exponential increase with time. On the other hand, the DE becomes asymptotic to 1.

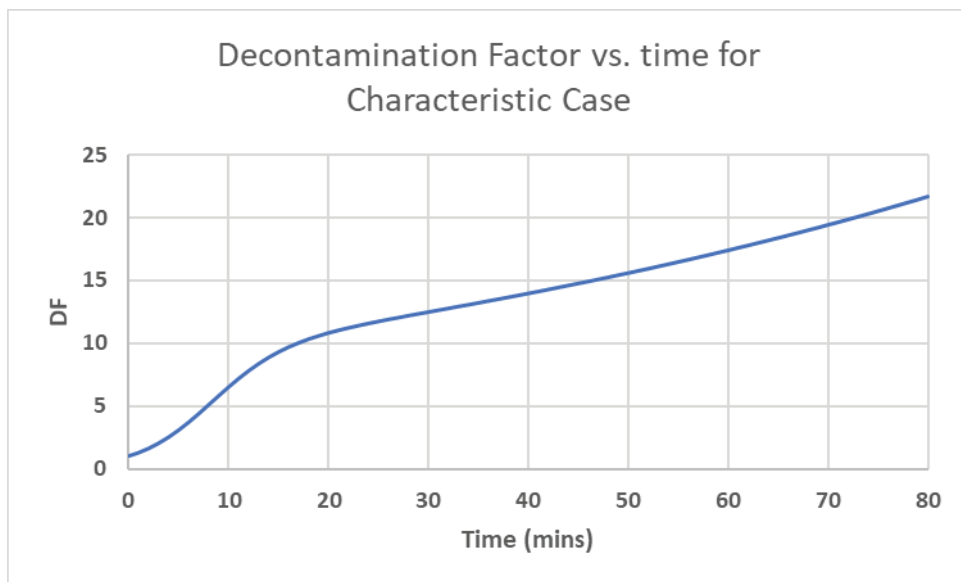


Figure 30: DF vs. time for Characteristic Case

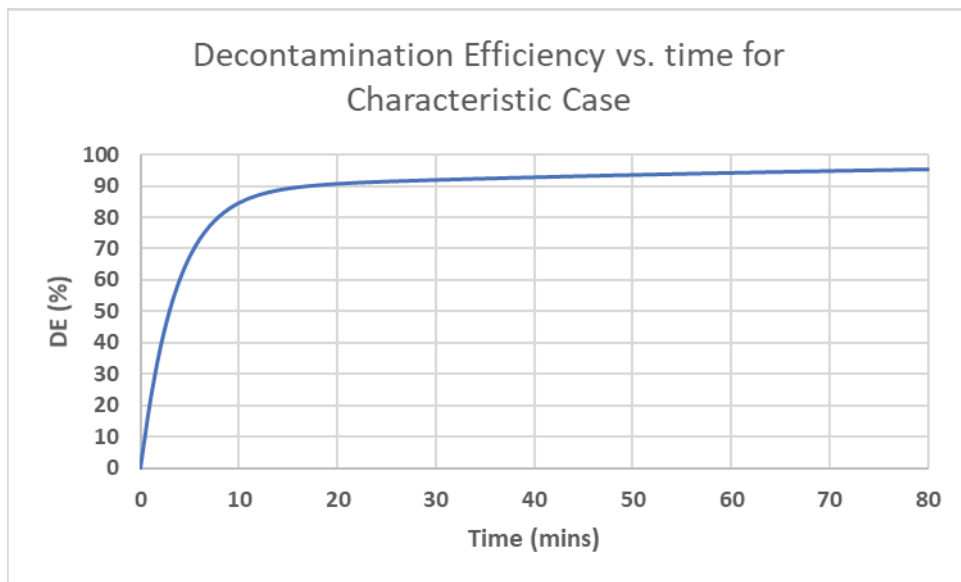


Figure 31: DE vs. time for Characteristic Case

7 Conclusions and Recommendations

The objective of this study is to experimentally quantify decontamination factors associated with post-accident aerosol decontamination in iPWRs. The objective also includes development of CFD-based simulated estimates of aerosol decontamination rates for a wider range of potential iPWR parameters beyond the tested range. The results of the study indicate that the iPWR decontamination factors are significantly high (19.3) and in the range of decontamination factors for containment vessel spray systems in large reactors.

To quantify the iPWR decontamination factors, this study included a parametric evaluation of critical elements that affect in-containment iPWR SMR vessel aerosol deposition, which provided qualified experimental data to support the applicability of previously established theoretical models. These theoretical models for thermophoresis, diffusiophoresis and gravitational settling were implemented into a CFD model, which was demonstrated to adequately predict deposition rates when compared against experiments. The model was also compared against prior experiments and demonstrated reasonable agreement. Aerosol removal rates for a wide range of surface-area-to-volume ratios and thermal-hydraulic conditions were estimated with the CFD code. Representative decontamination factors were calculated for a set of characteristic post-accident iPWR thermal-hydraulic conditions. To support independent development of similar models, the study provides a list of aerosol estimation modeling requirements, based on the methods implemented and the findings from the study.

This study describes the role of convective flow as a transport mechanism that moves particles throughout the containment vessel and into the saturation zone, where diffusiophoresis and thermophoresis can further act as deposition mechanisms. The study evaluated current aerosol deposition codes, which use the discrete method. These codes utilize one-dimensional aerosol deposition particle transport equations and a loss efficiency (the fraction of particles lost at the wall relative to the total number of particles near the wall) at deposition surfaces. While these codes may have convective flow assessment capabilities, it is typically implemented for convective heat transfer analysis of containment heat removal. No evidence has been found for application of convective flow as an in-containment vessel aerosol removal mechanism in recent nuclear safety analysis submission. It is important to note that although convective flow is not modeled as a particle transport mechanism, it is modeled for the purposes of thermal-hydraulic analysis as in the case of the AP1000 passive containment cooling system (PCCS) (Westinghouse Electric Co., 2008). The fact that convective flow is modeled for cooling, indicates the applicability of convective flow as a particle transport mechanism, if quantified and found to be significant enough to move particles in specific thermal-hydraulic environments.

Correlations for the aerosol removal rate due to turbulence and impaction are identified to characterize the additional aerosol removal associated with the turbulent environment. This is because convective flow induces a turbulent environment in the containment vessel and subsequently enhances mixing. It should be noted that although these terms had been identified by the NRC as potentially being applicable to reactors with relatively smaller containment vessels (NRC, 1996), these terms were not applied in decontamination analysis of the AP1000 design (Westinghouse Electric Co., 2008). By describing the significance and quantitative effects of convective flows, this study provides safety analysts with a basis for inclusion of turbulent and impaction aerosol removal coefficients in the performance of containment decontamination analyses.

The study further provides guidance for the use of the results by including a section on scaling methodology. The scaling methodology addresses scaling requirements for both aerosol characteristics and the aerosol environment. Finally, the study provides a list of recommendations for further study based on preliminary NRC and iPWR designer feedback.

8 References

- Birchley, J. (2004). Assessment of the MELCOR Code Against PHEBUS Experiment FPT-1 Performed in the Frame of ISP-46. *12th International Conference on Nuclear Engineering* (pp. 551-560). ASME.
- Cai, J., Wang, S., Niu, F., Shi, P., Liu, X., & Zhao, R. (2013). Scaling Analysis of Mixing and thermal Stratification in Passive Containment. *21st International Conference on Nuclear Engineering*.
- CEC. (1988). *Diffusiophoresis of Fission Product Aerosol in LWR Containment After Core Meltdown*. Brussels: Commission of the European Communities.
- Christensen, J., & Peterson, P. F. (2001). A One-Dimensional Lagrangian Model for Large-Volume Mixing. *Nuclear Engineering and Design*, 204, 299-320.
- EPRI. (2008). *Evaluation of Empirical Aerosol Correlations*. Electric Power Research Institute.
- EPRI. (2014a). *Advanced Nuclear Technology: Integrated Pressurized Water Reactor (iPWR) Containment Aerosol Deposition Behavior Phase 1: Test Plan Development*.
- EPRI. (2014b). *Integrated Pressurized Water Reactor (iPWR) Containment Aerosol Deposition Behavior*. Electric Power Research Institute.
- EPRI. (2017a). *Experimental Verification of Post-Accident Integrated Pressurized Water Reactor (iPWR) Aerosol Behavior - Engineering Basis and Test Plan (TP-PIT-1-16)*. Electric Power Research Institute.
- EPRI. (2017b). *Experimental Verification of Post-Accident Integrated Pressurized Water Reactor (iPWR) Aerosol Behavior - Computational Fluid Dynamics Model Development, Validation and Verification (PR-PIT-3-17-1)*. Electric Power Research Institute.
- EPRI. (2017c). *Experimental Verification of Post-Accident Integrated Pressurized Water Reactor (iPWR) Aerosol Behavior – Methodology for Extrapolation of Results from Computational Fluid Dynamics Simulations to Develop Aerosol Decontamination Factors (PR-PIT-3-17-2)*. Electric Power Research Institute.
- Epstein, M., Ellison, P. G., & Henry, R. E. (1986). Correlation of Aerosol Sedimentation. *Journal of Colloid and Interface Science*.
- INL. (2010). An Overview of Modeling Methods for Thermal Mixing and Stratification in Large Enclosures for Reactor Safety Analysis. Idaho National Labs.
- LLNL. (2014). *Deposition Velocity Methods for DOE Site Safety Analyses*.
- Mitchell, D. L. (1995). Use of Mass- and Area-Dimensional Power Laws for Determining Precipitation Particle Terminal Velocities. *Journal of the Atmospheric Sciences*.
- NEA. (1990). *Aerosol Transport in Severe Reactor Accidents*. Nordic Liaison Committee for Atomic Energy.
- NRC. (1993). *A Simplified Model of Aerosol Removal by Containment Sprays*.

- NRC. (1996). *A simplified model of aerosol removal by natural processes in reactor containments*. U.S. Nuclear Regulatory Commission.
- NRC. (2014). *MELCOR Best Practices as Applied in the State-of-the-Art Reactor Consequence Analyses Project*.
- Nuclear Energy Agency. (2009). *State-of-the-art Report on Nuclear Aerosols*. Organisation for Economic Co-operation and Development.
- Sher, R., & Hobbins, R. (2011). Aerosol Deposition Mechanisms. In *Transport and Removal of Aerosols in Nuclear Power Plants Following Severe Accidents*. American Nuclear Society.
- SNL. (1994). *MELCOR 1.8.2 Assessment: Aerosol Experiments ABCOVE AB5, AB6, AB7, and LACE LA2*. Sandia National Laboratory.
- Westinghouse Electric Co. (2008). *AP1000 Design Control Document*.
- Zhang, Z., & Chen, Q. (2007). Comparison of the Eulerian and Lagrangian Methods for Predicting Particle Transport in Enclosed Spaces. *Atmospheric Environment*, 5236 - 5248.
- Zhao , H., & Peterson, P. F. (2010). *An Overview of Modeling Methods for Thermal Mixing and Stratification in Large Enclosures for Reactor Safety Analysis*. Idaho National Laboratories.
- Zhao, Y., Zhang, L., & Tong, J. (2015). Development of rapid atmospheric source term estimation system for AP1000 nuclear power plant. *Progress in Nuclear Energy*, 264-275.

Appendix A: Statistical Analysis

A statistical analysis is performed to examine the combined aerosol deposition velocity effects due to thermophoresis, gravitational settling, convective flow, and diffusiophoresis (TGCD). Varying test conditions associated with the test cases are examined. The TGCD test conditions, namely the independent test variables, notation, and numerical test values are:

- Temperature of the reactor vessel (RV) (Fahrenheit, °F), T_{RV} , values 400, 450, and 500°F.
- Pressure (pounds per square inch, psi), P , values 20, 65, and 200 psi.
- Area-to-Volume ratio (per foot, ft^{-1}), A/V , values 0.60, 0.67, 0.75.

All tests were performed at a fixed temperature of the containment vessel (CV), $T_{CV} = 220^\circ\text{F}$, in the presence of steam.

Statistical analysis and modeling used data from the TGCD Test Cases (TC) to determine the Decontamination Factor (DF). TGCD denotes thermophoresis, gravitational settling, convective flow, and diffusiophoresis aerosol effects. The TGCD test cases are TC 5, 6, 7, 10, 11, 13 and 15.

Statistical results from the TGCD TC indicate that 69.16 minutes is the time at which there is a 95% confidence that 95% decontamination (equivalently, 5% of the particle mass remains) has occurred. The basis for this value is discussed at the conclusion to this Appendix. This time is referred to as $T(95/95)$ and denotes the time at which there is a 95% confidence that 95% decontamination has occurred. In general, this notation is $T(C/D)$, namely, there is a $C\%$ confidence that $D\%$ decontamination has occurred.

The DF value for $T(95/95) = 69.16$ minutes is presented in

Figure 32 for the Characteristic Case and each TC. The Characteristic Case combines data from all TC. The upper and lower 2-sigma values are calculated for the Characteristic Case to illustrate the potential range of DF at time = $T(95/95)$ and identify DF overlap for each TC. Similar charts may be generated for any time value.

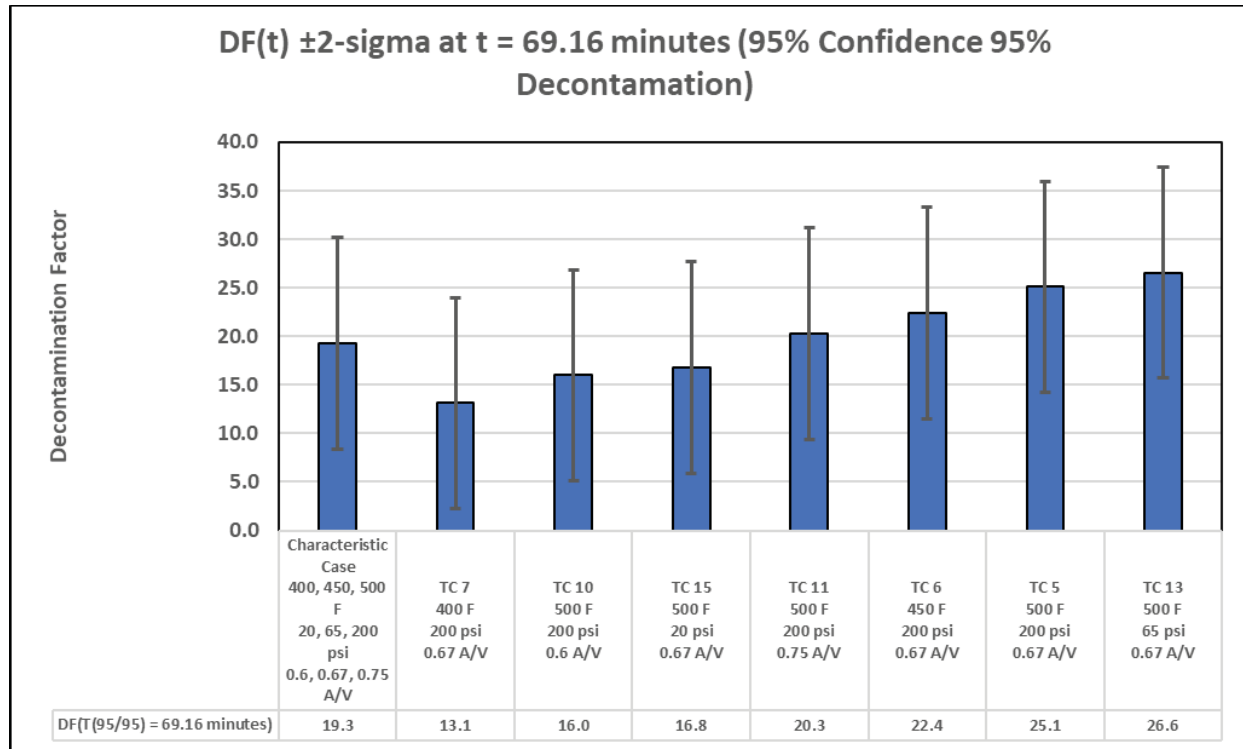


Figure 32: Decontamination Factor at T(95/95) for the Characteristic Case and all TC

Since DF is time-dependent, it is properly expressed as DF(t). Each TC collected normalized particle mass, N_m , data from 0 to 80 minutes. N_m is also expressed as $N_m(t)$. The relationship between $N_m(t)$ and DF(t) at any time t is:

$$DF(t) = \frac{1}{N_m(t)}$$

$N_m(t)$ is modeled using a double exponential decay curve as:

$$N_m(t) = ae^{-bt} + ce^{-dt}$$

Where a, b, c, d are constants and $b, d > 0$.

$N_m(t)$ is also modeled using a triple exponential decay curve as:

$$N_m(t) = a + be^{-ct} + de^{-ft}$$

Where a, b, c, d, f are constants and $c, f > 0$.

$N_m(t)$ curve fit parameters for the Characteristic Case and each TC are provided in Table 7 (in Section 6) of this document. A graphical portrayal of $N_m(t)$ curve fits for the Characteristic Case and each TC is presented in Figure 33. A graphical portrayal of DF(t) curve fits for the Characteristic Case and each TC is presented in Figure 34.

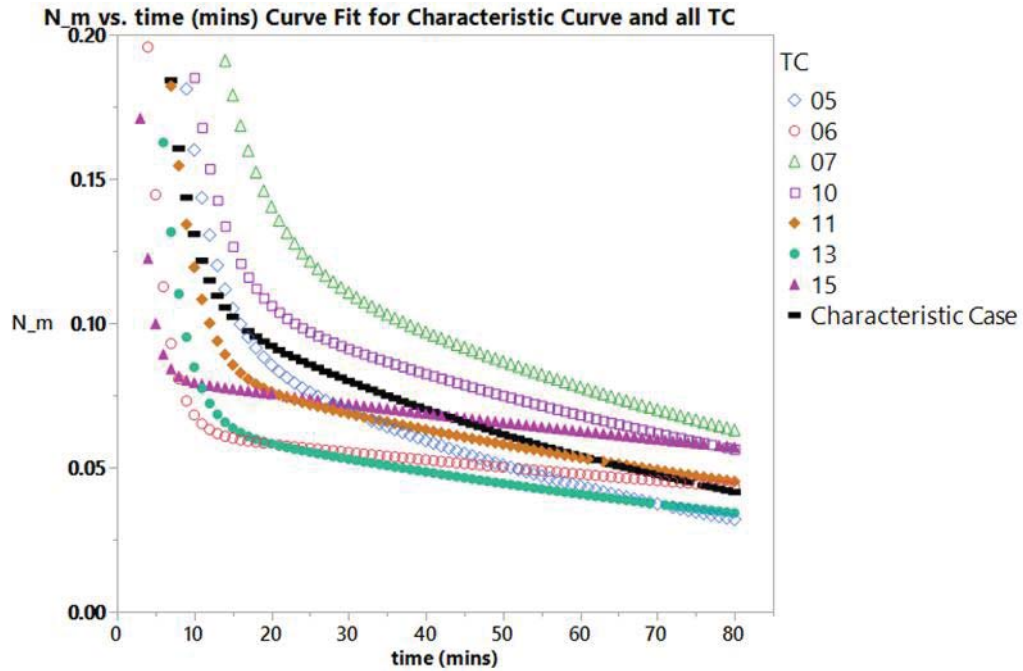


Figure 33: Normalized Mass Curve Fit for Characteristic Case and all TC

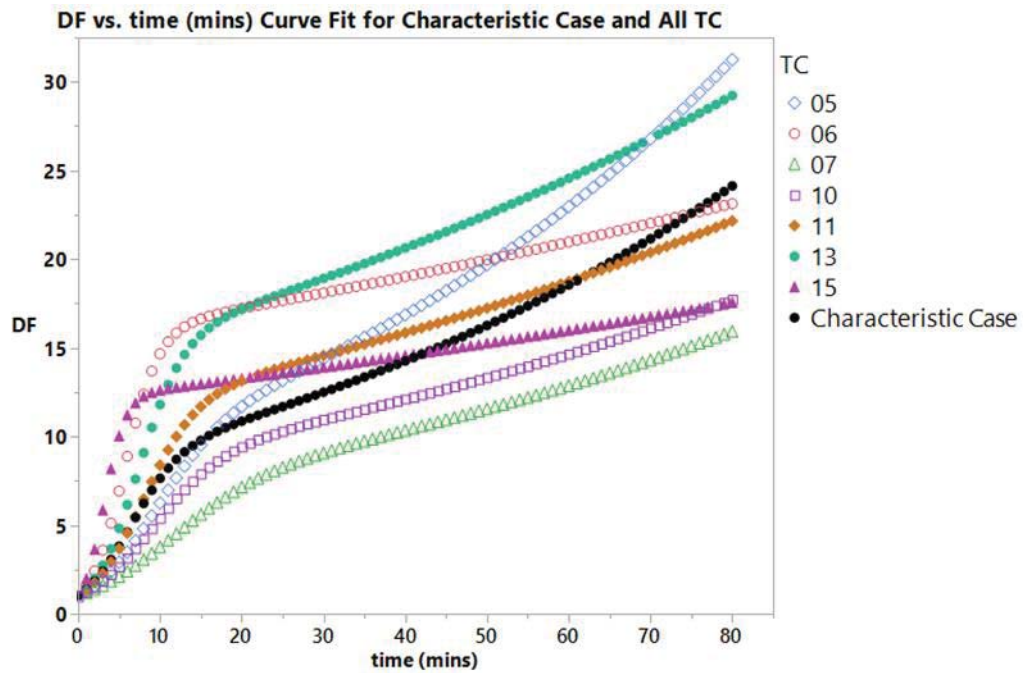


Figure 34: Decontamination Factor Curve Fit for Characteristic Case and all TC

The curve fits for each test case are shown as follows from Figure 35 to Figure 41.

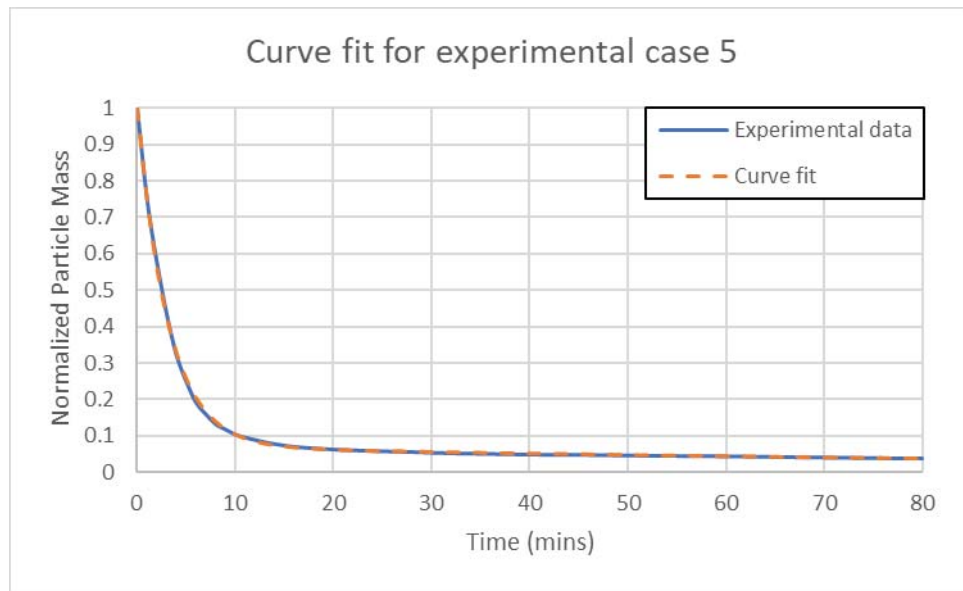


Figure 35: Curve fit for experimental case 5

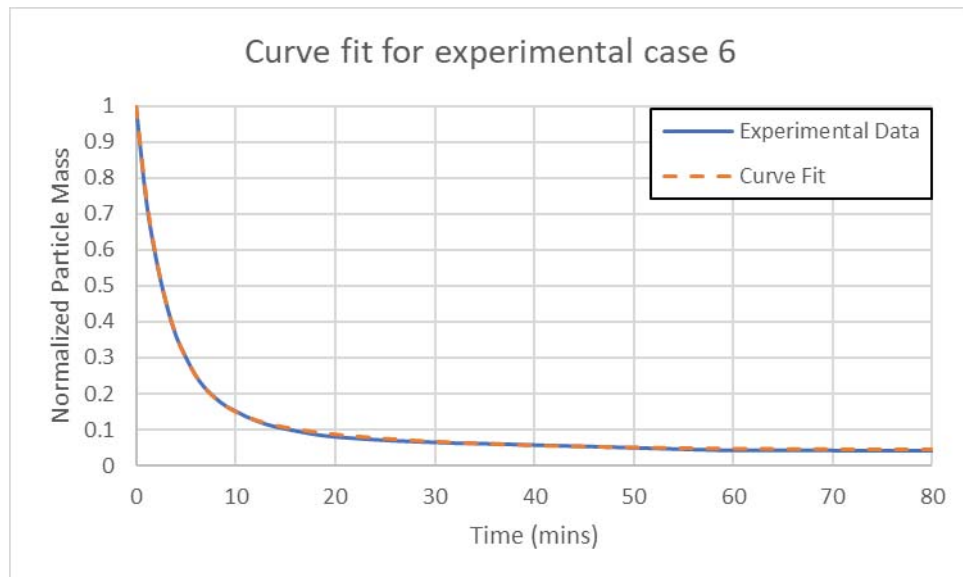


Figure 36: Curve fit for experimental case 6

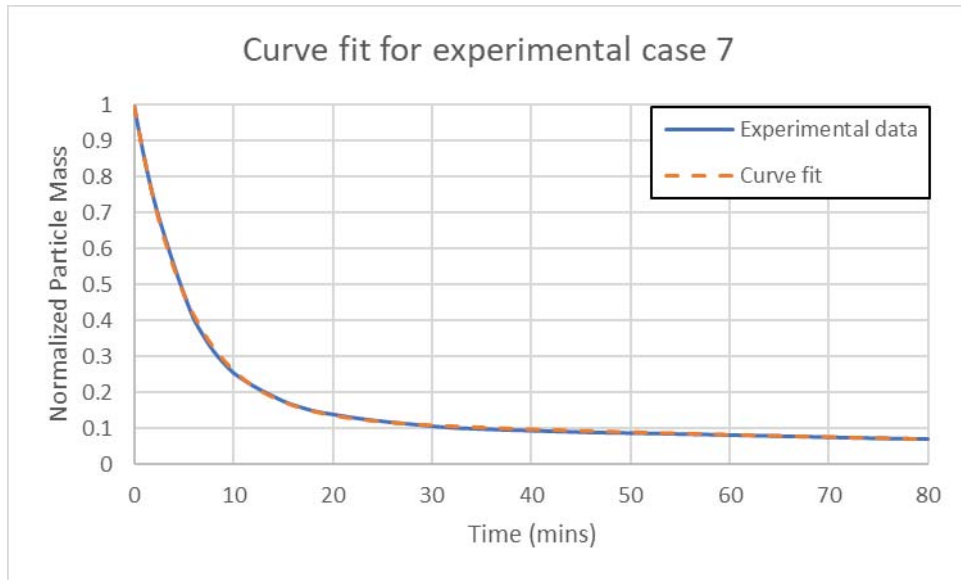


Figure 37: Curve fit for experimental case 7

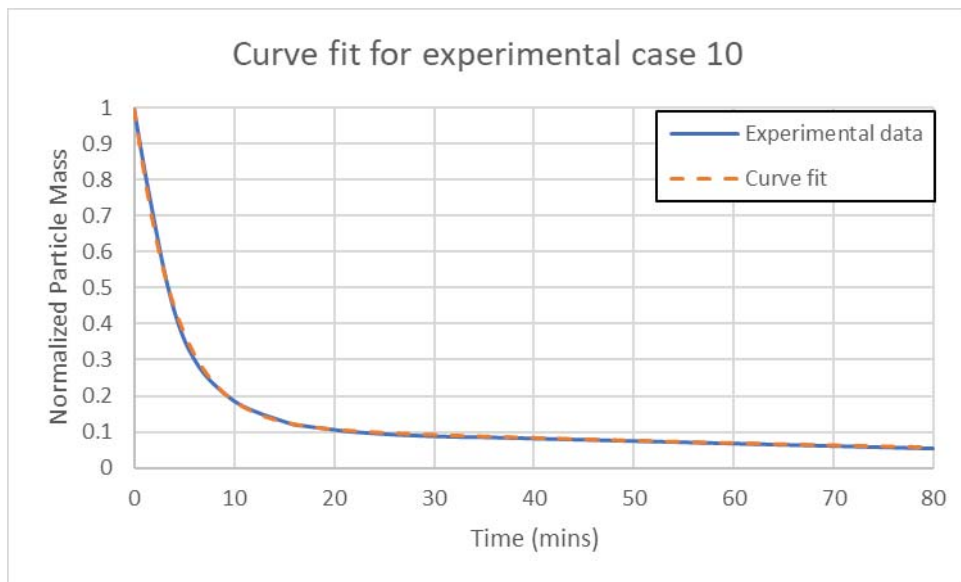


Figure 38: Curve fit for experimental case 10

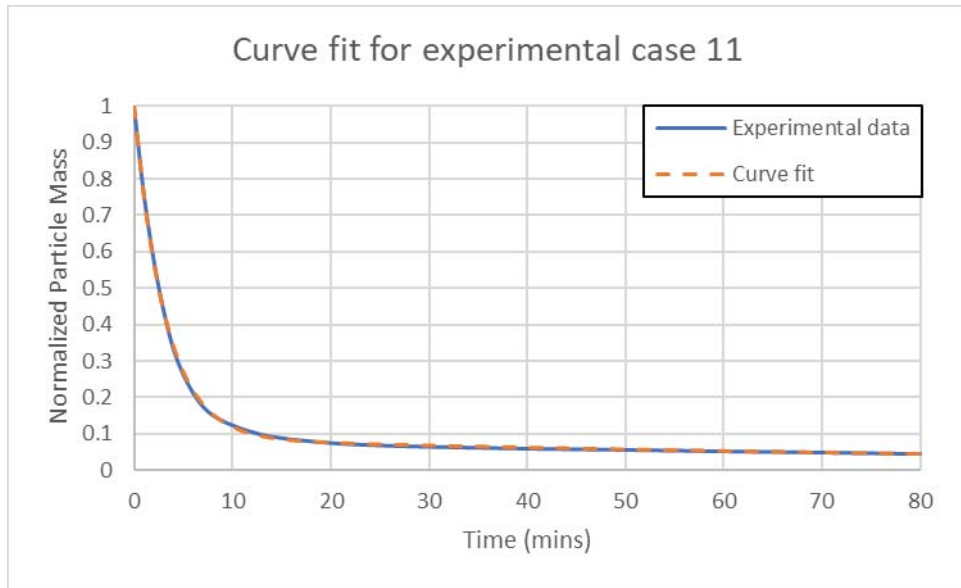


Figure 39: Curve fit for experimental case 11

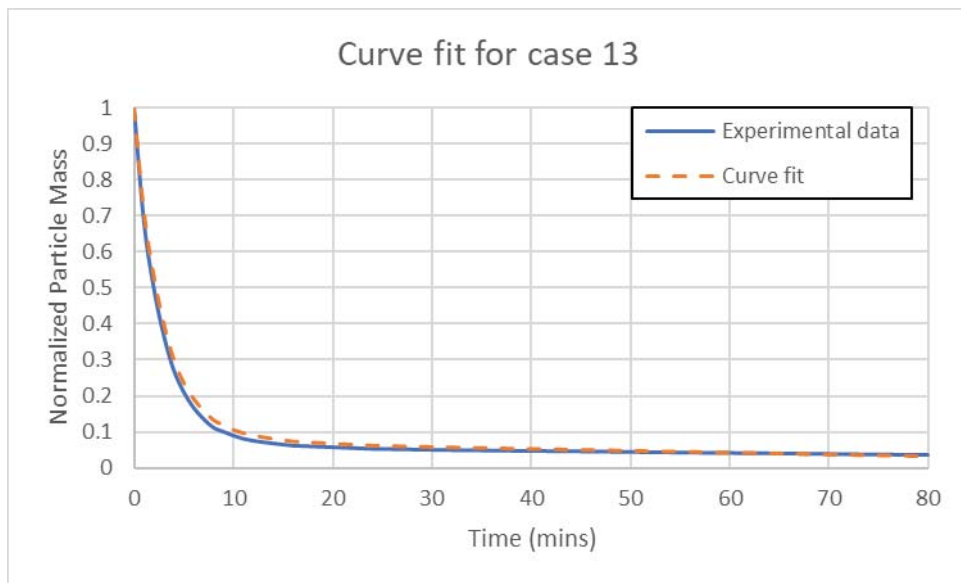


Figure 40: Curve fit for experimental case 13

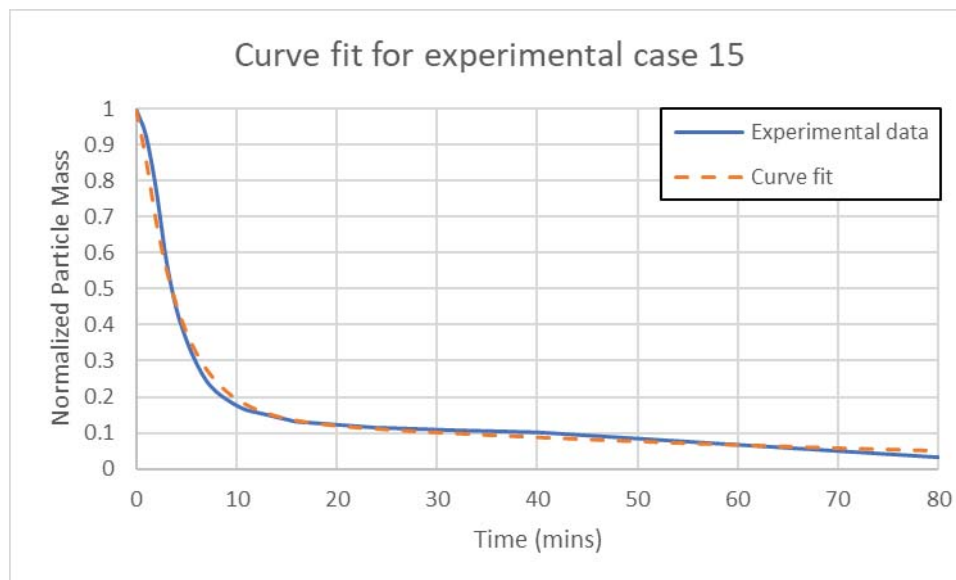


Figure 41: Curve fit for experimental case 15

Examination of the differences between the curve fit and the TC data, the low Root Mean Square Error (RMSE), and the R-square value, indicates these are acceptable curve fits.¹⁰ The RMSE indicates how concentrated the TC data are around the curve fit; values close to zero are desirable. The R-square value also measures how close the TC data are to the curve fit. It is the percentage of the response variable variation that is explained by the curve fit. Values above 0.90 (90%) are desirable.

The notation T(C/D) is used to denote the time at which there is a C% confidence that D% decontamination has occurred. In general, C = 95% confidence is investigated.

- T(95/95) represents the time at which there is a 95% confidence that 95% decontamination has occurred. TC data which provided times of 95% decontamination occurred were examined. These data are denoted as T95.
- T(95/90) represents the time at which there is a 95% confidence that 90% decontamination has occurred. TC data which provided times of 90% decontamination occurred were examined. These data are denoted as T90.
- T(95/80) represents the time at which there is a 95% confidence that 80% decontamination has occurred. TC data which provided times of 80% decontamination occurred were examined. These data are denoted as T80.

Examination of the influences of each temperature, pressure, and A/V ratio test condition was examined. Summary statistics were generated and used to determine the probability distribution describing T95, T90, and T80 values. Based on the probability distributions for T95, T90, and T80, the T(95/95), T(95/90), and T(95/80) corresponding to 95% confidence that 95%, 90%, or 80% decontamination occurred.

¹⁰ Differences in the Double Exponential Curve fit and the test data was consistent time-equivalent and concentration-equivalent approach used to generate each test value for N(t).

The remainder of this Appendix provides a discussion of (1) how data collection and processing was performed to include a graphical comparison of TC data to the Characteristic Case, (2) the power analysis associated with the test conditions of temperature of the reactor vessel, the pressure, and the Area-to-Volume ratio, (3) summary statistics for 80%, 90%, and 95% decontamination, (4) the effects of each test condition on 80%, 90%, and 95% decontamination results, and (5) the analysis used to determine that $T(95/95) = 69.16$ minutes is the time at which there is a 95% confidence that 95% decontamination has occurred.

Data Collection and Processing

Laser imaging and sensor systems were used to collect and process aerosol and particle deposition data. Aerosol concentration measurements were collected for each TGCD test condition. Counts of particle deposition were collected at discrete time intervals. The counts were transformed to a normalized particle mass, denoted as N_m , of particles which remained at the end of each time interval; for example, $N_m = 0.2$ means 20% of the particles remained at the end of the time interval. Examination of N_m equal to 0.20, 0.10 was performed to determine each of T80, T90, and T95, respectively.

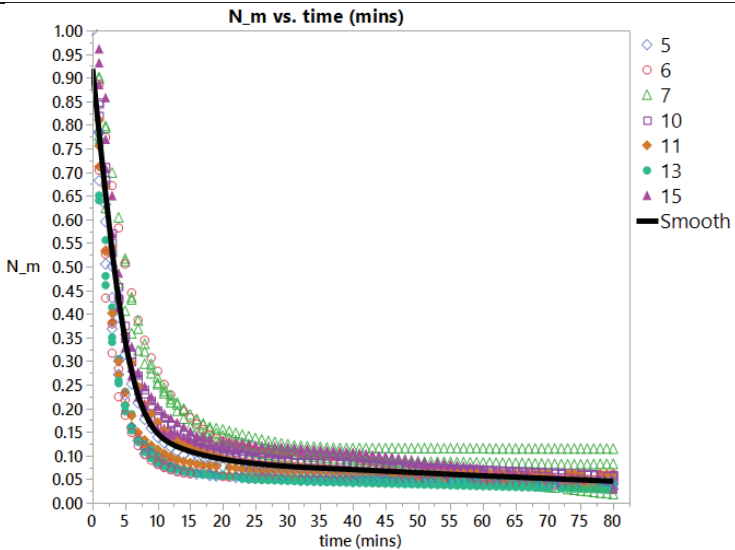
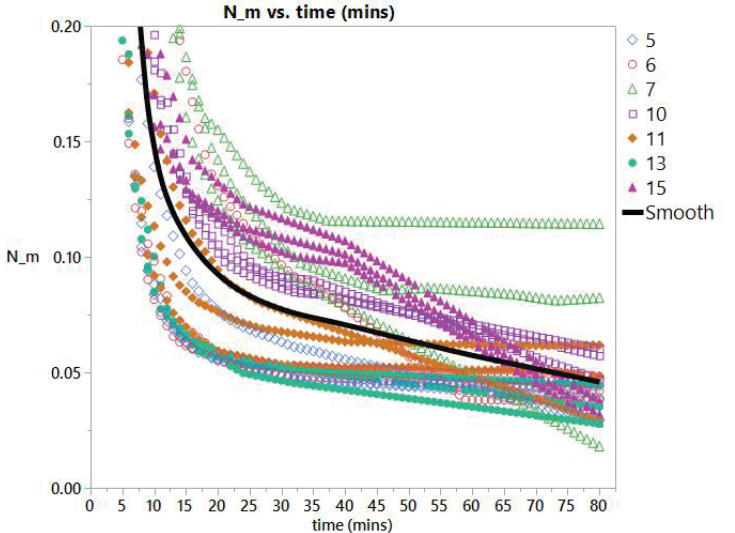
Table 8 illustrates the time-based data collected for all TC when Normalized Particle Mass, N_m , ranges from 0 to 1 and for all TC when N_m ranges from 0 to 0.2 for greater resolution. To complement the T80, T90, and T95 numerical values, the time-based test case raw data for $N_m \leq 0.20$ is also provided for each of the test cases.

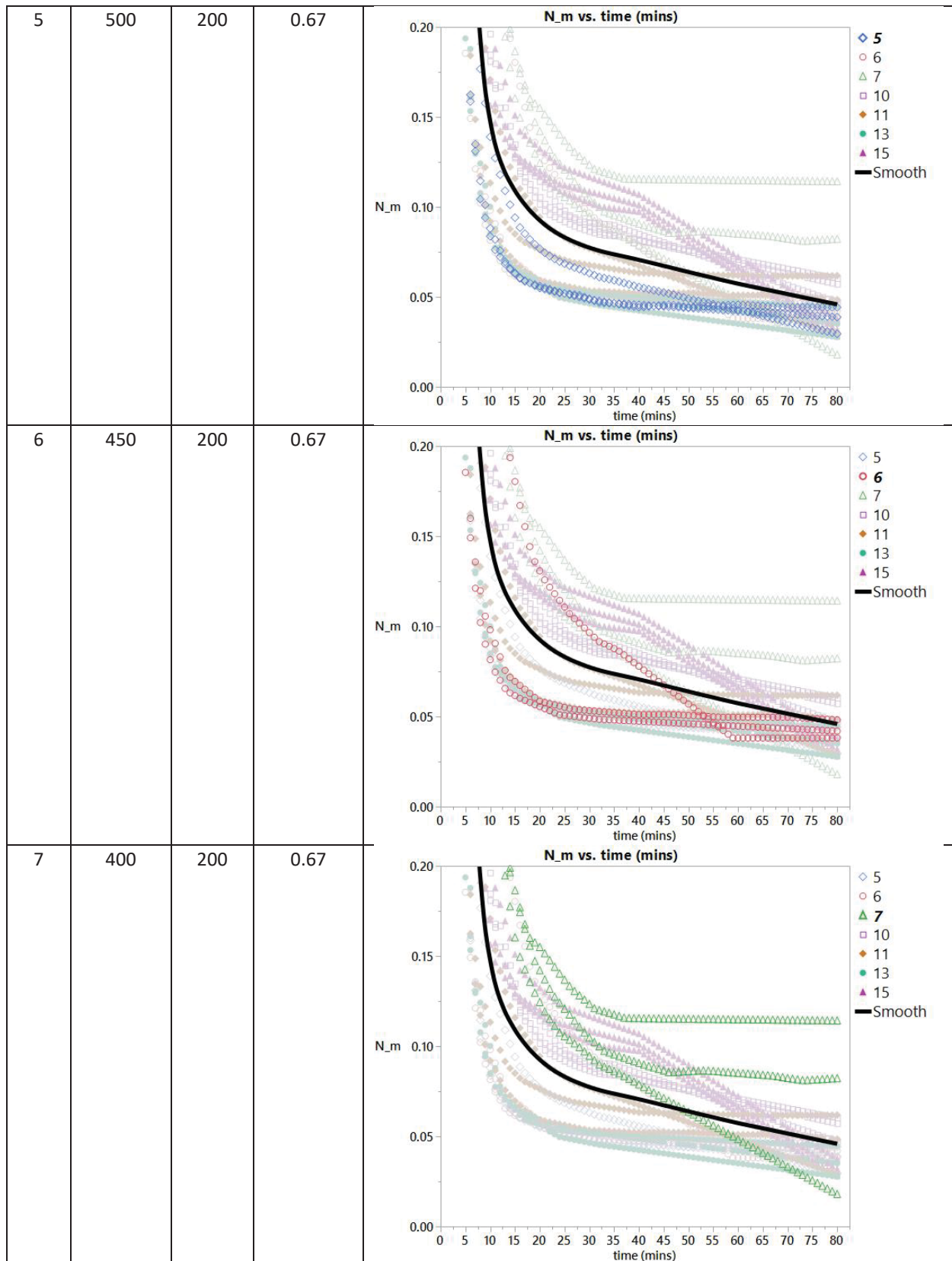
The smoothed curve (denoted as Smooth) represents the double exponential fit for the characteristic curve as described in the equation below. This visualization allows a comparison of each TC N_m values to curve fit.

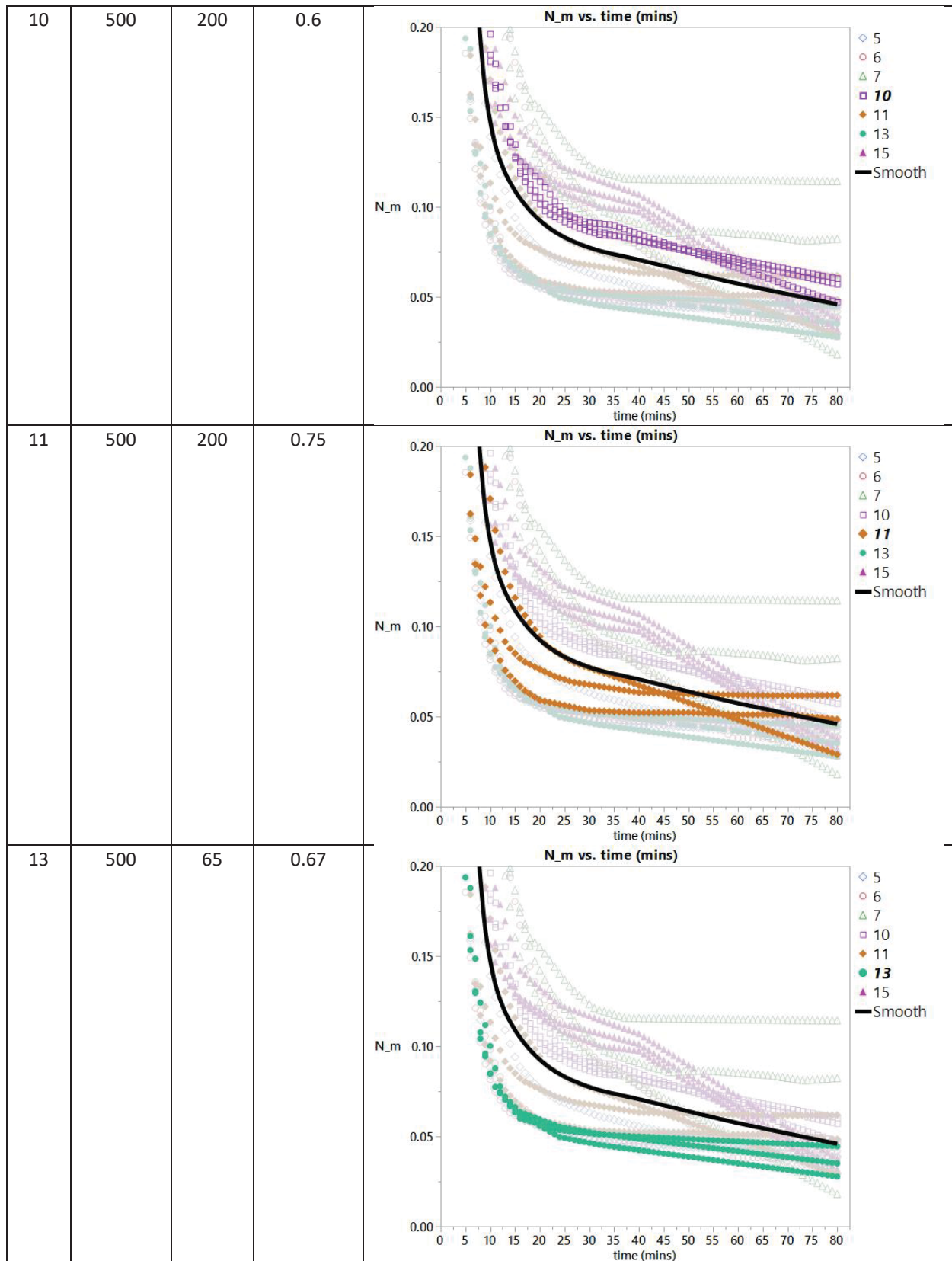
$$N_m(t) = 0.111e^{-0.011t} + 0.897e^{-0.281t}$$

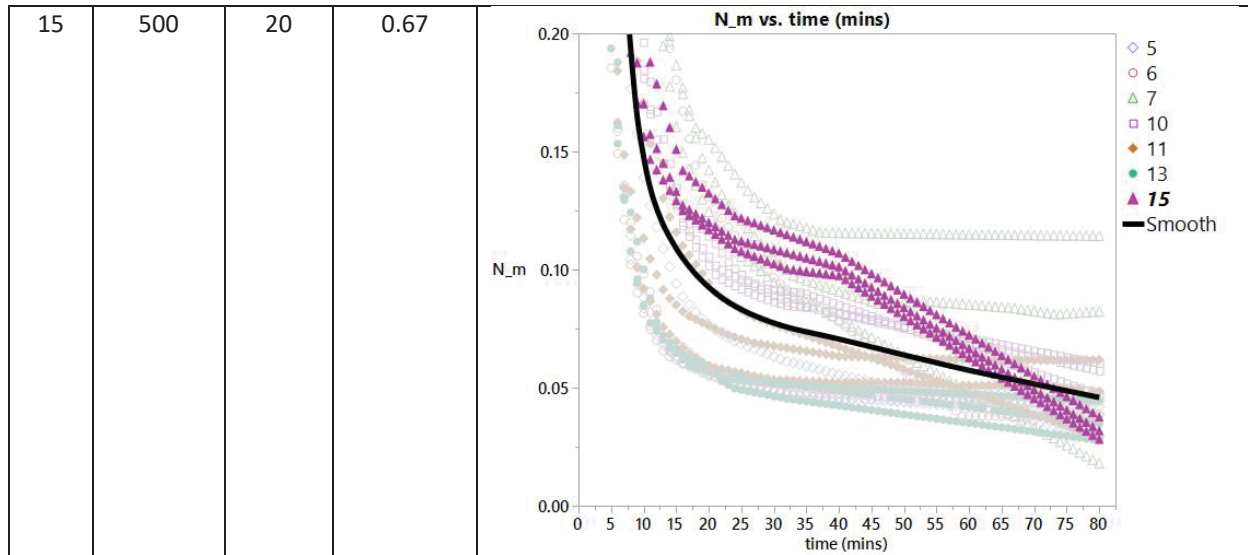
The shaded curves represent other test cases, so a comparison can be made to the identified TC. The subsequent statistical analysis specifically addresses points on each test case curve which correspond to T80 ($N_m = 0.20$), T90 ($N_m = 0.10$), and T95 ($N_m = 0.05$).

Table 8: TCGD test conditions for T80, T90, and T95 test results

TC	TRV (°F)	P (psi)	A/V	N _m vs. time (minutes) for TC test results
All TC for $0 \leq N_m \leq 1$				
All TC for $0 \leq N_m \leq 0.2$				







Power Analysis

Power analysis is performed to illustrate how well the effects of the independent variables are demonstrated. The power range is from 64% to 90% for all TGCD test cases as indicated in Table 9.

Table 9: TCGD Power Analysis for TGCD Test Cases

Power Analysis for TGCD Test Cases At 95% confidence	
Term	Power
Intercept	0.77
T_{RV} ($^{\circ}F$)	0.83
P (psi)	0.90
A/V	0.64

Summary Statistics for T80, T90, and T95

Based on TC data for all test conditions, histograms with upper standard error bars and summary statistics were determined. The standard error bars indicate the possible height of each bin of the histogram.

Figure 42 illustrates T80 is bounded by 13.91 minutes. The distribution is moderately uniform with a range (difference between maximum and minimum) is 9.29 minutes and 50% of the data lies between 5.23 minutes and 10.03 minutes. The arithmetic mean is 8.16 minutes with a standard error of the mean of 0.69 minutes. The coefficient of variation is 39.01% at one standard deviation, 3.18 minutes. The median is 7.74 minutes and the geometric mean is 7.61 minutes.

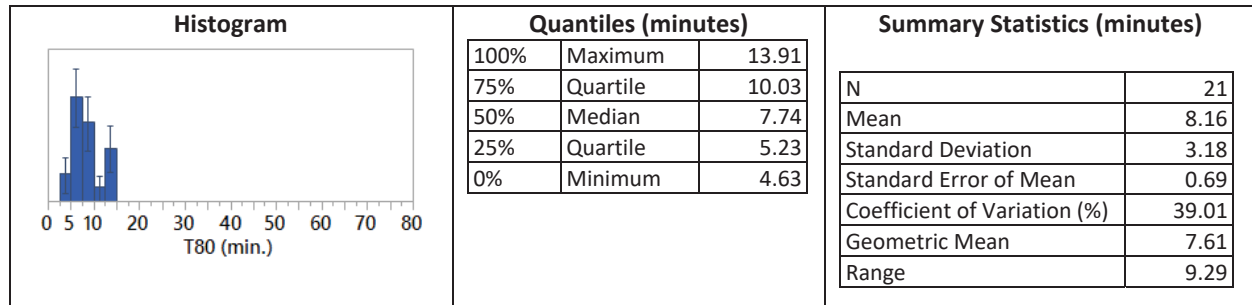


Figure 42: T80 Histogram and Summary Statistics

Figure 43 illustrates T90 is bounded by 44.00 minutes. The distribution is moderately right skewed. The range (difference between maximum and minimum) is 35.82 minutes and 50% of the data lies between 9.09 minutes and 28.44 minutes. The arithmetic mean is 19.43 minutes with a standard error of the mean of 2.59 minutes. The coefficient of variation is 59.57% at one standard deviation, 11.58 minutes. The median is 16.38 minutes and the geometric mean is 35.82 minutes.

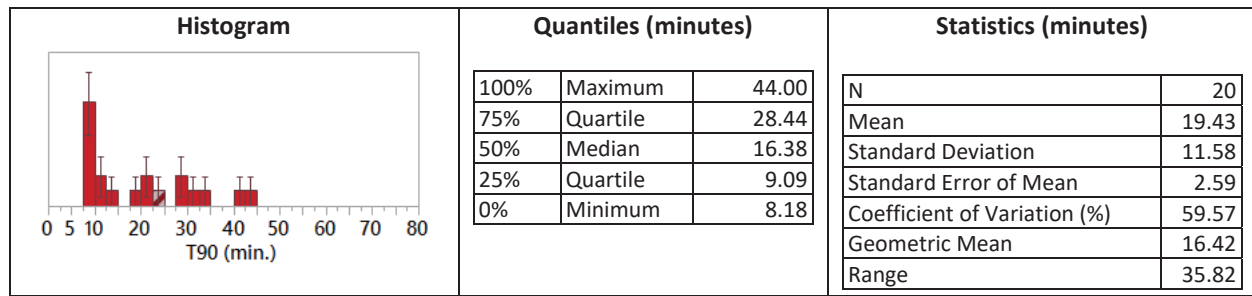


Figure 43: T90 Histogram and Summary Statistics

Figure 44 illustrates that T95 is bounded by 77.03 minutes. The distribution is moderately uniform. The range (difference between maximum and minimum) is 53.25 minutes and 50% of the data lies between 30.69 minutes and 68.99 minutes. The arithmetic mean is 51.10 minutes with a standard error of the mean of 4.62 minutes. The coefficient of variation is 47.61% at one standard deviation, 18.49 minutes. The median is 53.80 minutes and the geometric mean is 47.61 minutes.

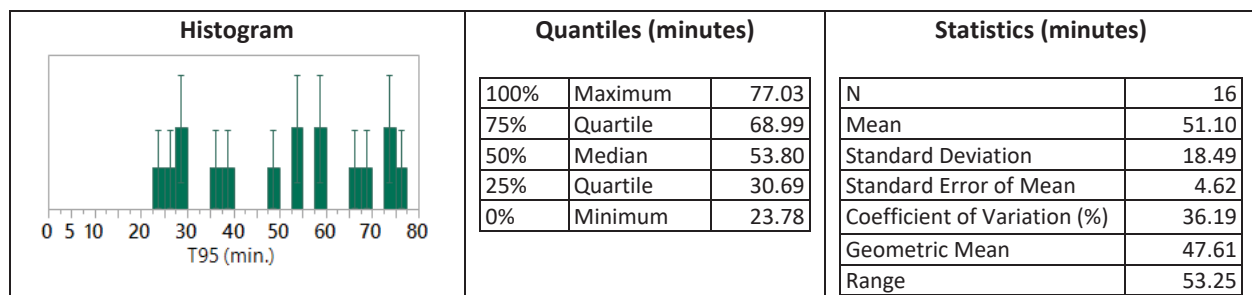


Figure 44: T95 Histogram and Summary Statistics

Effects of Test Conditions on T80, T90, and T95

The effects of the TGCD test conditions on T80, T90, and T95, including the 95% confidence interval about the linear fit for T80, T90, and T95 are examined for each test condition associated with T_{RV} , P, and A/V. The Root Mean Square Error (RMSE) is also provided for each of the linear fits of T80, T90, and T95. The RMSE is a measure of the differences between the T80, T90, and T95 values predicted by a linear model and the TGCD values actually observed.

Figure 45 illustrates the effect of T_{RV} ($^{\circ}$ F) on T80, T90, and T95, including the 95% confidence Interval (shaded area) about the mean value for each of T80, T90, and T95. It indicates a moderately decreasing T80 and T90 as T_{RV} increases and a fairly constant increasing T95 as T_{RV} increases. The narrow 95% confidence interval around the T80 fitted line is explained by the relatively small RMSE of 2.49 minutes. A wider 95% confidence interval around the T90 fitted line is explained by the large RMSE of 11.65 minutes. and the influence of the test results associated with T_{RV} ($^{\circ}$ F) = 400 $^{\circ}$ F or 450 $^{\circ}$ F. A considerably wider 95% confidence interval around the T95 fitted line is explained by the large RMSE of 19.14 minutes and the influence of the test results associated with T_{RV} ($^{\circ}$ F) = 400 $^{\circ}$ F or 450 $^{\circ}$ F.

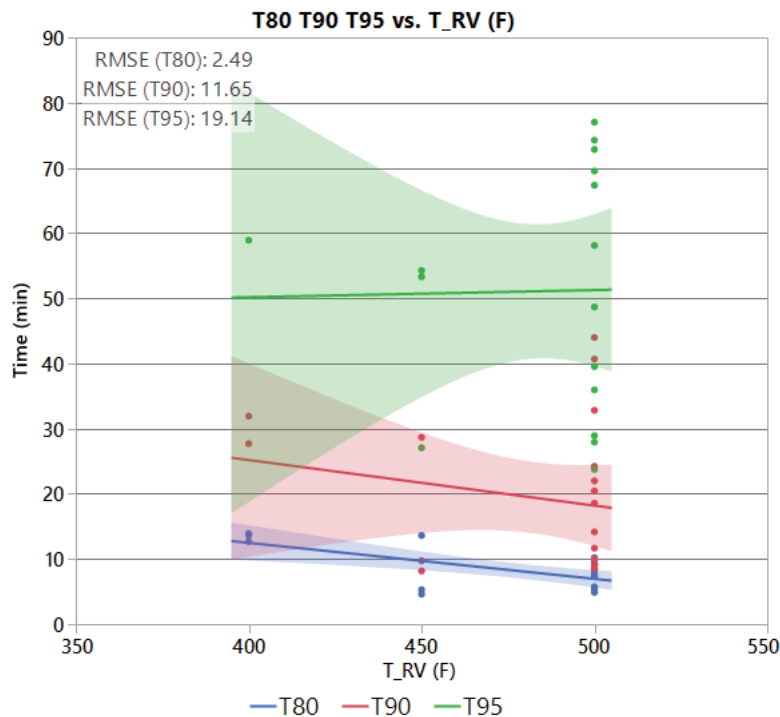


Figure 45: Effect of T_{RV} ($^{\circ}$ F) on T80, T90, and T95

Figure 46 illustrates the effect of P (psi) on T80, T90, and T95, including the 95% Confidence Interval (shaded area) about the mean value for each of T80, T90, and T95. It indicates a moderately constant T80 and a moderately decreasing T90 and T95 as P increases. The narrow 95% confidence interval around the T80 fitted line is explained by the relatively small RMSE of 3.21 minutes. A wider 95% confidence interval around the T90 fitted line is explained by the large RMSE of 10.95 minutes and the influence of the test results associated with P = 20 psi or 65 psi. A considerably wider 95% confidence interval around the T95

fitted line (between 12 minutes and 65 minutes) is explained by the large RMSE of 18.98 minutes and the influence of the test results associated with $P = 20$ psi or 65 psi.

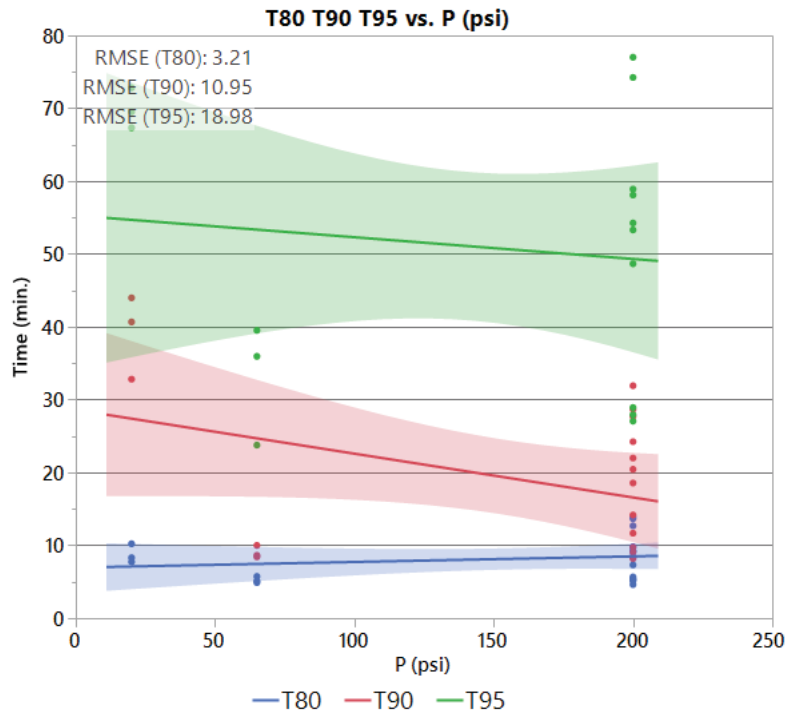


Figure 46: Effect of P (psi) on T80, T90, and T95

Figure 47 illustrates the effect of surface-area-to-volume ratio (A/V) on T80, T90, and T95, including the 95% Confidence Interval (shaded area) about the mean value for each of T80, T90, and T95. It indicates a moderately decreasing T80 and T90 as A/V increases and a moderately increasing T95 as A/V increases. The narrow 95% confidence interval around the T80 fitted line is explained by the relatively small RMSE of 3.15 minutes. A wider 95% confidence interval around the T90 fitted line is explained by the large RMSE of 11.58 minutes and the influence of the test results associated with $A/V = 0.6$ or 0.75 . A considerably wider 95% confidence interval around the T95 fitted line is explained by the large RMSE of 19.1 minutes and the influence of the test results associated with $A/V = 0.6$ or 0.75 .

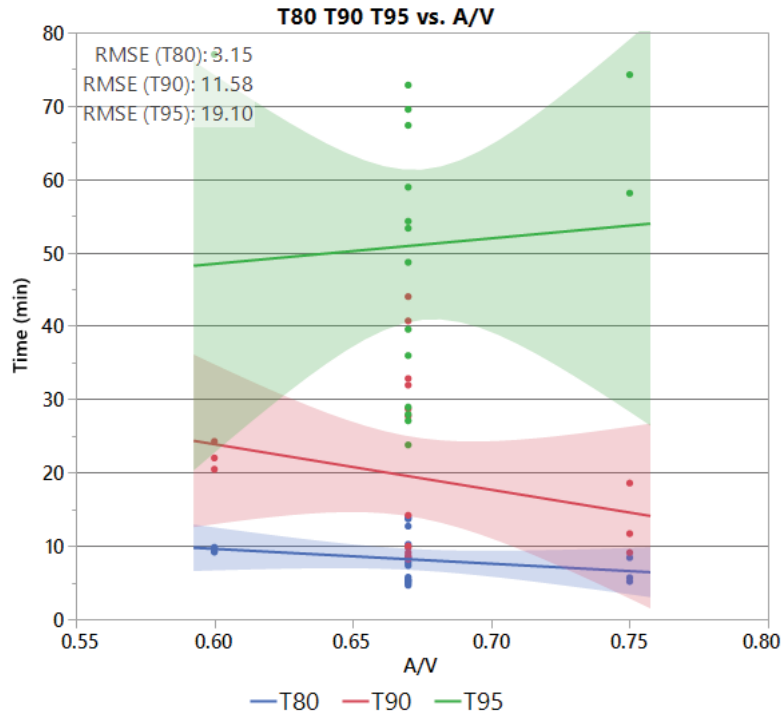


Figure 47: Effect of A/V on T80, T90, and T95

Probability Functions for T80, T90, and T95

Probability function fits were performed for the observations for each of T80, T90, and T95, respectively. Although lognormal or Weibull distributions can be fit to T80, T90, and T95, the small number of samples ($N = 21$ for T80, $N = 20$ for T90, and $N = 16$ for T95) and the low P-values associated with the goodness of fit test P-values (e.g., maximum Cramer von Mises W Test $P = 0.25$) suggest concluding the choice of a lognormal distribution or a Weibull distribution is not warranted.

Note that When $N = 21$, there is a 95% confidence that there is at least a 13% probability the maximum value obtained from T80 sample data has not identified the true maximum value for the population of possible T80 values. This probability increases to 14% for T90 when $N = 20$ and increases to 17% for T95 when $N = 16$.

In the absence of statistically significant goodness of fit results, a triangular probability function is used to describe the distributions for each of T80, T90, and T95 and illustrated in Figure 48. The triangular distribution is characterized by three parameters, the minimum (MIN), the most likely (ML), and the maximum (MAX). The form of the triangular distribution, denoted as $f(x)$ is for the variable, x , is provided below.

$$f(x) = \frac{2(x - MIN)}{(ML - MIN) \times (MAX - MIN)} \quad \text{for } MIN \leq x \leq ML$$

$$f(x) = \frac{2(MAX - x)}{(MAX - ML) \times (MAX - MIN)} \quad \text{for } ML < x \leq MAX$$

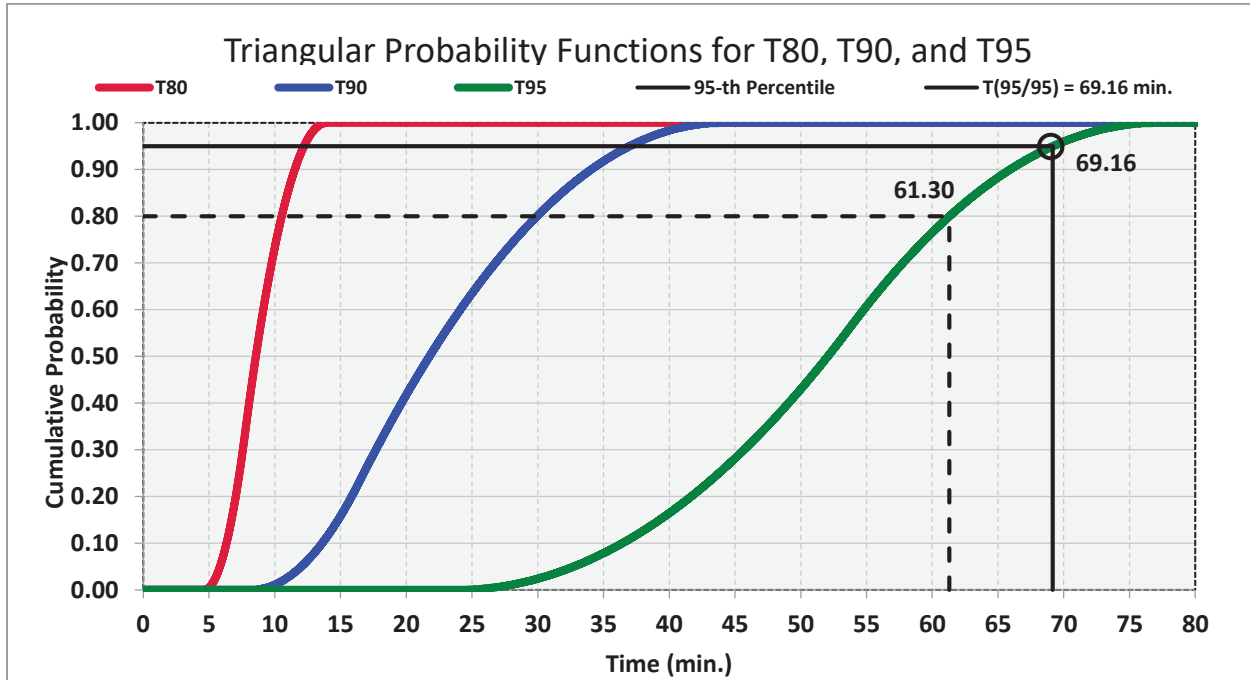


Figure 48: Triangular Probability Functions for T80, T90, and T95 (with T95/95 = 69.16 minutes indicated)

T(C/D), namely, the time at which there is a C% confidence that D% decontamination has occurred, is directly obtained from the cumulative probability distribution. The probability curve corresponding to D = 80%, 90%, and 95% decontamination is represented by the distribution of the T80, T90, and T95 values. Two horizontal lines cross the probability curves at the 95th-percentile and the 80th-percentile values. The intersection of those curves with the percentile values represent the confidence, C = 95% or 80%.

- For example, examine the T95 curve. The curve intersects the 95th-percentile line at 69.16 minutes, thus, T(95/95) = 69.16 minutes, and this is the time at which there is a 95% confidence that 95% decontamination has occurred.
- For example, examine the T90 curve. The curve intersects the 95th-percentile line at 26.36 minutes, thus, T(95/90) = 26.36 minutes, and this is the time at which there is a 95% confidence that 90% decontamination has occurred.

In summary,

- The distribution of times achieving 95% decontamination is represented by the T95 curve and is modeled using a triangular (23.78, 53.80, 77.03) distribution
 - Mean Value = 51.54 minutes
 - $T(80/95)$ = 61.30 minutes, i.e., 80% confidence of 95% decontamination
 - $T(95/95)$ = 69.16 minutes, i.e., 95% confidence of 95% decontamination
- The distribution of times achieving 90% decontamination is represented by the T90 curve and is modeled using a triangular (8.18, 16.38, 44.00) distribution
 - Mean Value = 22.50 minutes
 - $T(80/90)$ = 28.93 minutes, i.e., 80% confidence of 90% decontamination
 - $T(95/90)$ = 39.96 minutes, i.e., 95% confidence of 90% decontamination
- T80 is modeled using a triangular (4.63, 7.74, 13.91) distribution
 - Mean Value = 8.76 minutes
 - $T(80/80)$ = 10.52 minutes, i.e., 80% confidence of 80% decontamination
 - $T(95/80)$ = 12.22 minutes, i.e., 95% confidence of 80% decontamination

Appendix B: Summation of Aerosol Decontamination Parameters

NRC NUREG CR/6189 documented that thermophoretic, diffusiophoretic and turbulent deposition processes can be simultaneously operative on all deposition surfaces. Occurrence of a specific deposition process is dependent on the particle position and whether gravitational deposition augments, opposes, or does not affect the process. Particles are in one of three states, and depending on the state, the particles may be affected by gravitational, thermophoretic, diffusiophoretic and turbulent convective deposition processes.

Deposition velocities for thermophoresis and diffusiophoresis are additive since they act in the same direction based on the creation of thermal and steam concentration gradients, respectively. The particle deposition velocity calculations are as follows (NRC, 1996):

At upward-facing surfaces: $V_d = V_{d,g} + V_{d,o}$

At downward-facing surfaces: $V_d = \text{Max}[0, V_{d,o} - V_{d,g}]$

At vertical surfaces: $V_d = V_{d,o}$

where

V_d = Overall deposition velocity

$V_{d,g}$ = Deposition velocity due to gravity

$V_{d,o}$ = Deposition velocity due to other processes (thermophoresis, diffusiophoresis, and turbulent convection)

This implies that uncertainty effects are closely coupled by (a) the position of the particle, and (b) the effects of one or more combinations of thermophoresis, diffusiophoresis, or turbulent convection on the particle.

The term $V_{d,o}$ represents the deposition velocity due to other processes (thermophoresis, diffusiophoresis, and turbulent convection). An uncertainty indicator, δ_Σ , should be used to account for uncertainty in the coupled condition of particle location and deposition effect. This coefficient is also used to select the model for the summation of deposition mechanisms. The probability density function for δ_Σ is uniform within the range of 0 to 1 (NRC, 1996). The method of calculation is stated below and illustrated in Figure 49.

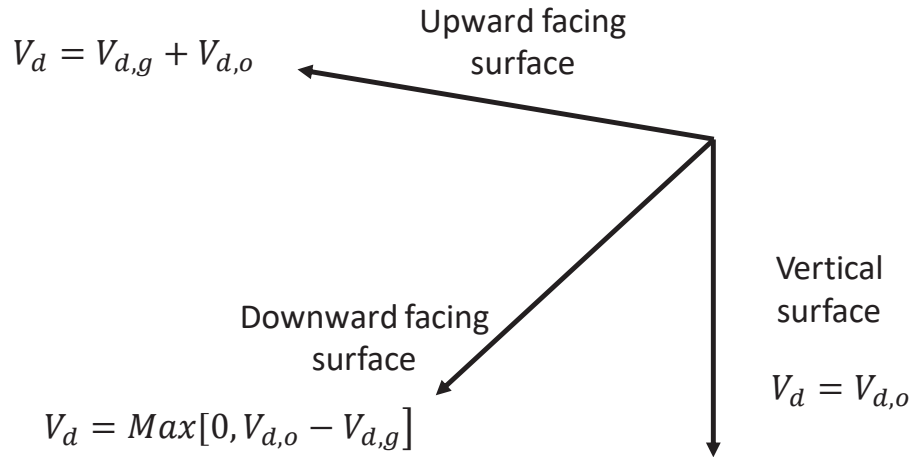


Figure 49: Vectorial calculation of deposition velocities

$$V_{d,o} = \begin{cases} V_{d,t} + V_{d,d} + V_{d,c} & \text{if } 0 \leq \delta_{\Sigma} \leq 1/3 \\ \sqrt{[V_{d,t} + V_{d,d}]^2 + V_{d,c}^2} & \text{if } 1/3 \leq \delta_{\Sigma} \leq 2/3 \\ \max(V_{d,t} + V_{d,d}, V_{d,c}) & \text{if } 2/3 \leq \delta_{\Sigma} \leq 1 \end{cases}$$

where

$V_{d,t}$ = Deposition velocity due to thermophoresis

$V_{d,d}$ = Deposition velocity due to diffusiophoresis

$V_{d,c}$ = Deposition velocity due to turbulent convection

δ_{Σ} = Uncertainty parameter uniformly distributed between [0,1]

CFD-Specific Considerations

The drift-flux model, which was developed and implemented for the CFD model used in this study, allows tracking of particles so that the position of the particle can be identified as being at an upward-facing surface, at a downward-facing surface, or at a vertical surface. Once this is known, the use of δ_{Σ} implies the following:

- One-third of the time, the deposition velocity is due to thermophoresis, diffusiophoresis, and turbulent convection, namely, $V_{d,t} + V_{d,d} + V_{d,c}$

- One-third of the time, the deposition velocity is due to either thermophoresis and diffusiophoresis, or the deposition velocity is due to turbulent convection only, namely, $\max(V_{d,t} + V_{d,d}, V_{d,c})$
- One-third of the time, the deposition velocity is the resultant of the thermophoresis and diffusiophoresis deposition velocities and the turbulent convection velocity, namely,

$$\sqrt{[V_{d,t} + V_{d,d}]^2 + V_{d,c}^2}$$

When using the CFD model, the expected value of $V_{d,o}$ may be incorporated as:

$$V_{d,o} = 0.33 \times \left[(V_{d,t} + V_{d,d} + V_{d,c}) + \max(V_{d,t} + V_{d,d}, V_{d,c}) + \sqrt{[V_{d,t} + V_{d,d}]^2 + V_{d,c}^2} \right]$$

Appendix C: Experimental Data

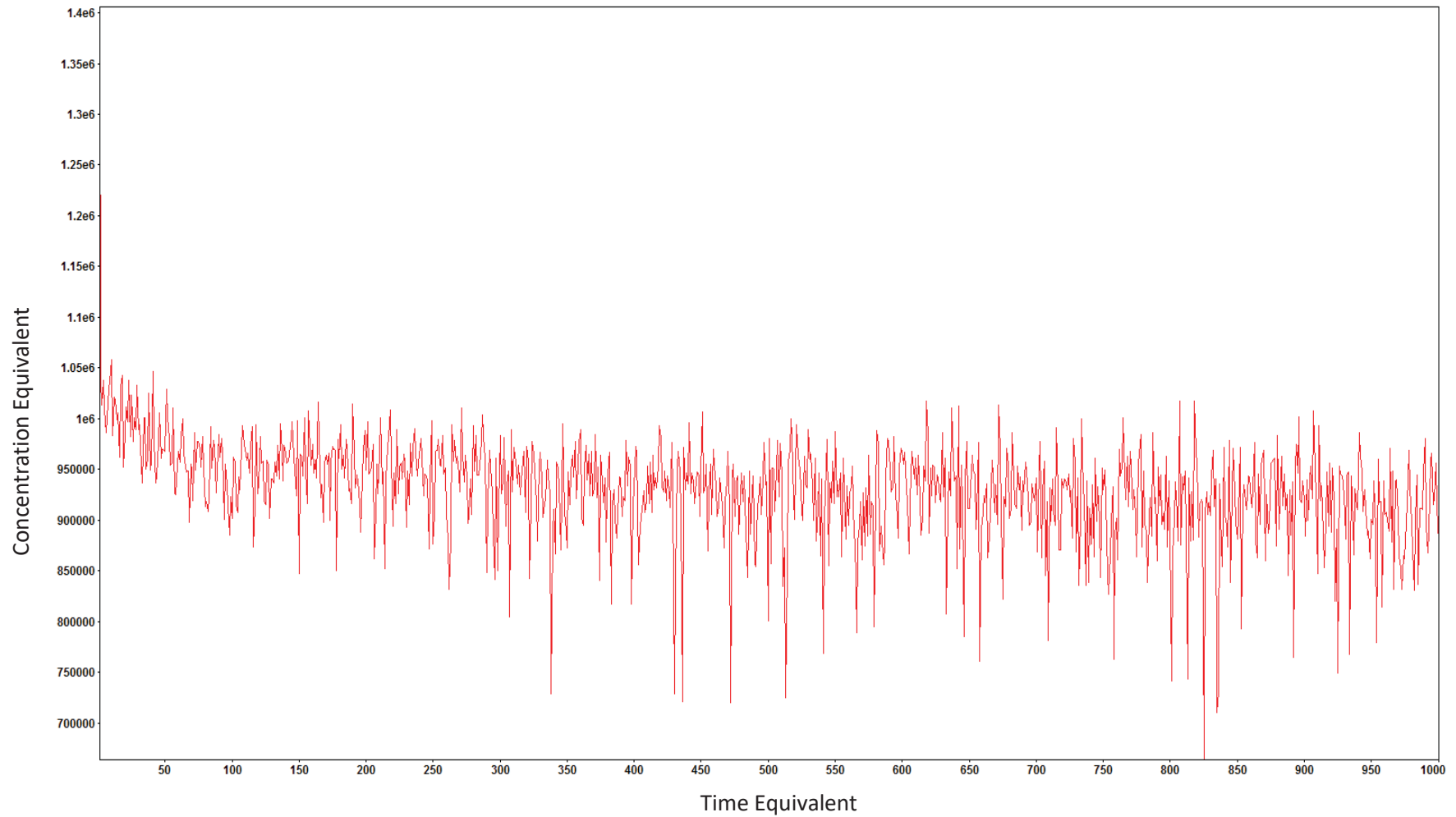


Figure 50: Experimental decay curve for gravitational settling (Case 1)

Note: Time Equivalent is the time it takes to record the number of images, which Concentration Equivalent is a measure of the particle concentration based on the light intensity of the laser beams, and is directly proportional to the particle concentration.

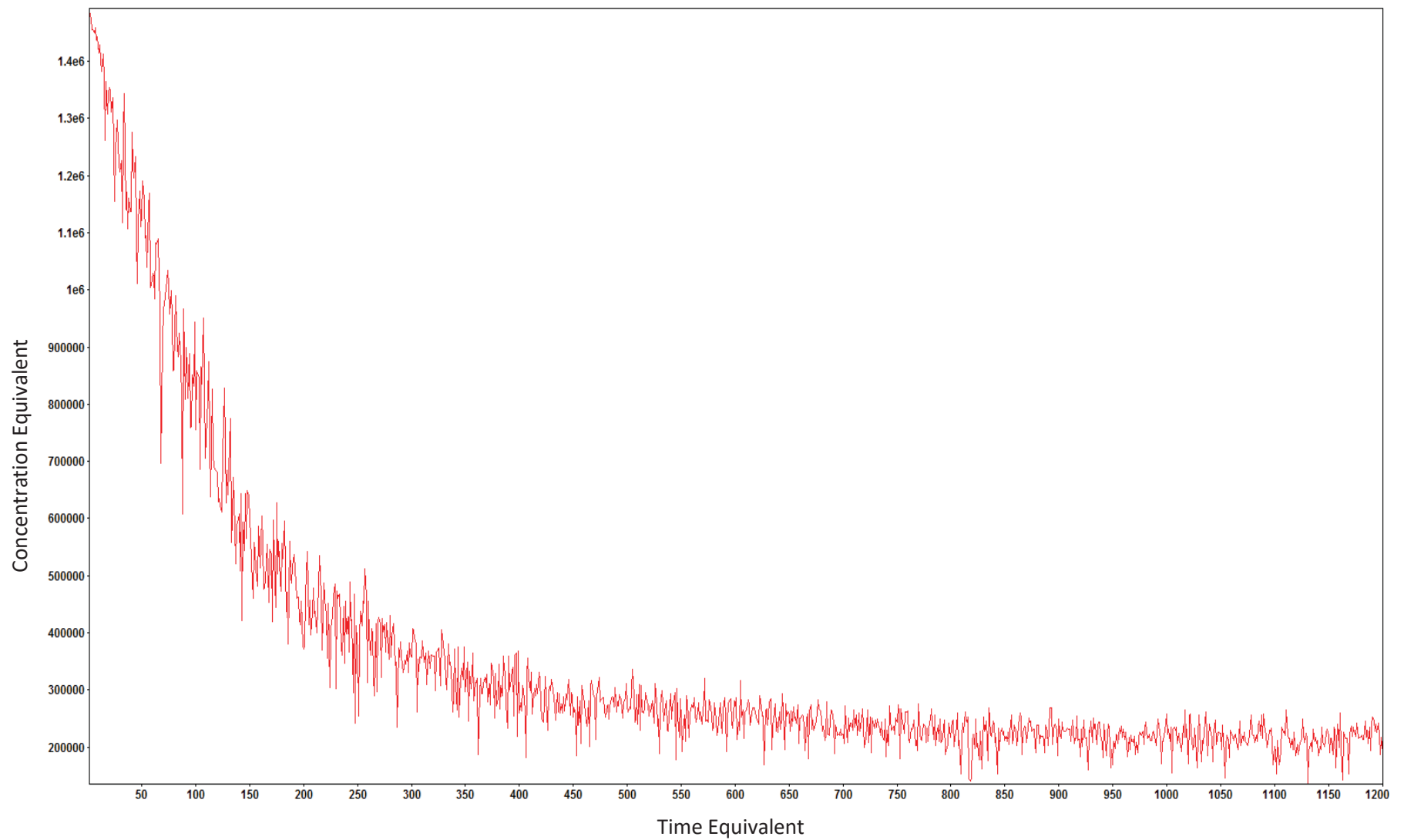


Figure 51: Experimental decay curve for TGC case with $T_{RV} = 500^{\circ}\text{F}$ (Case 2)

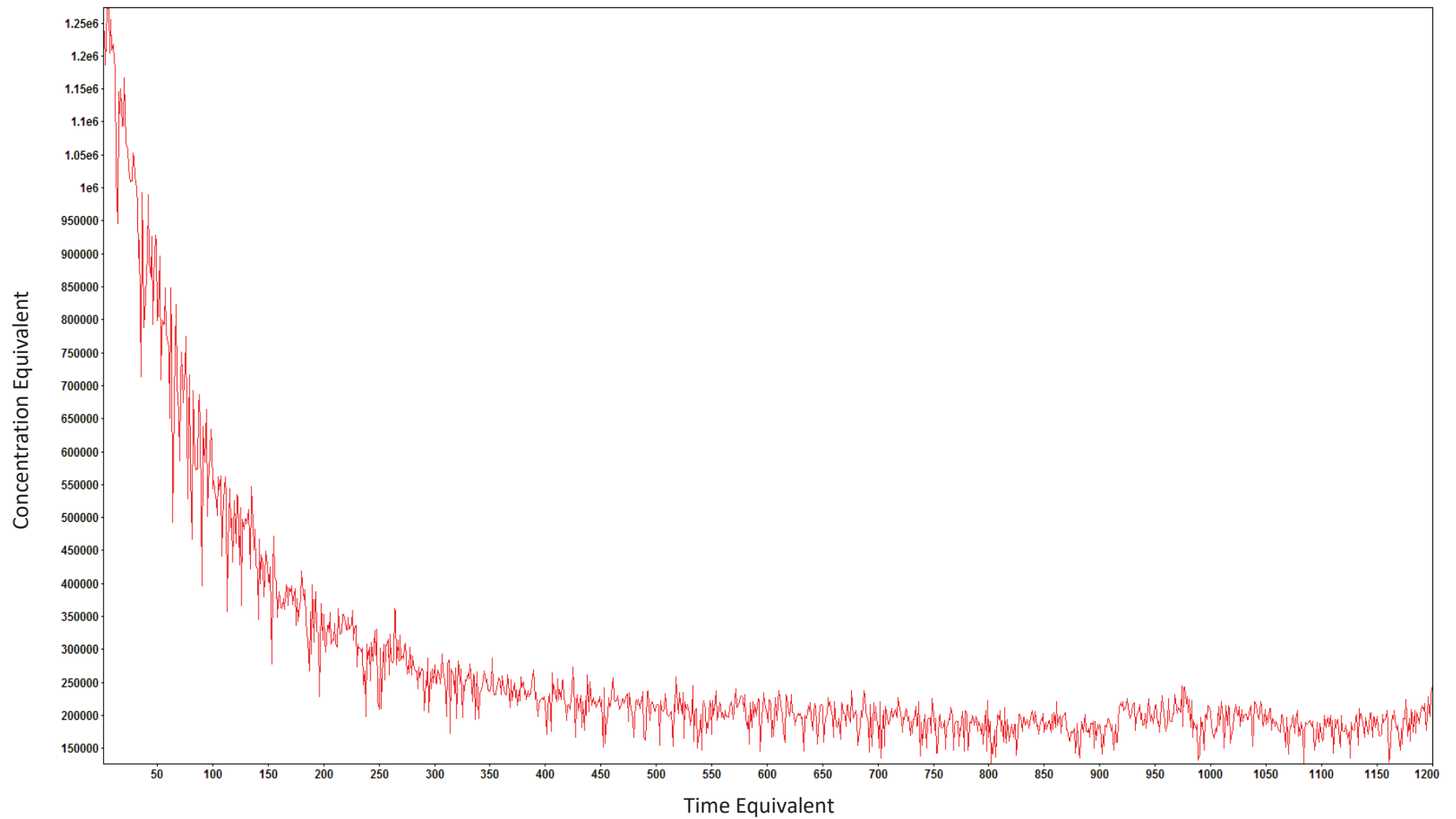


Figure 52: Experimental decay curve for TGC case with $T_{RV} = 450^{\circ}\text{F}$ (Case 3)

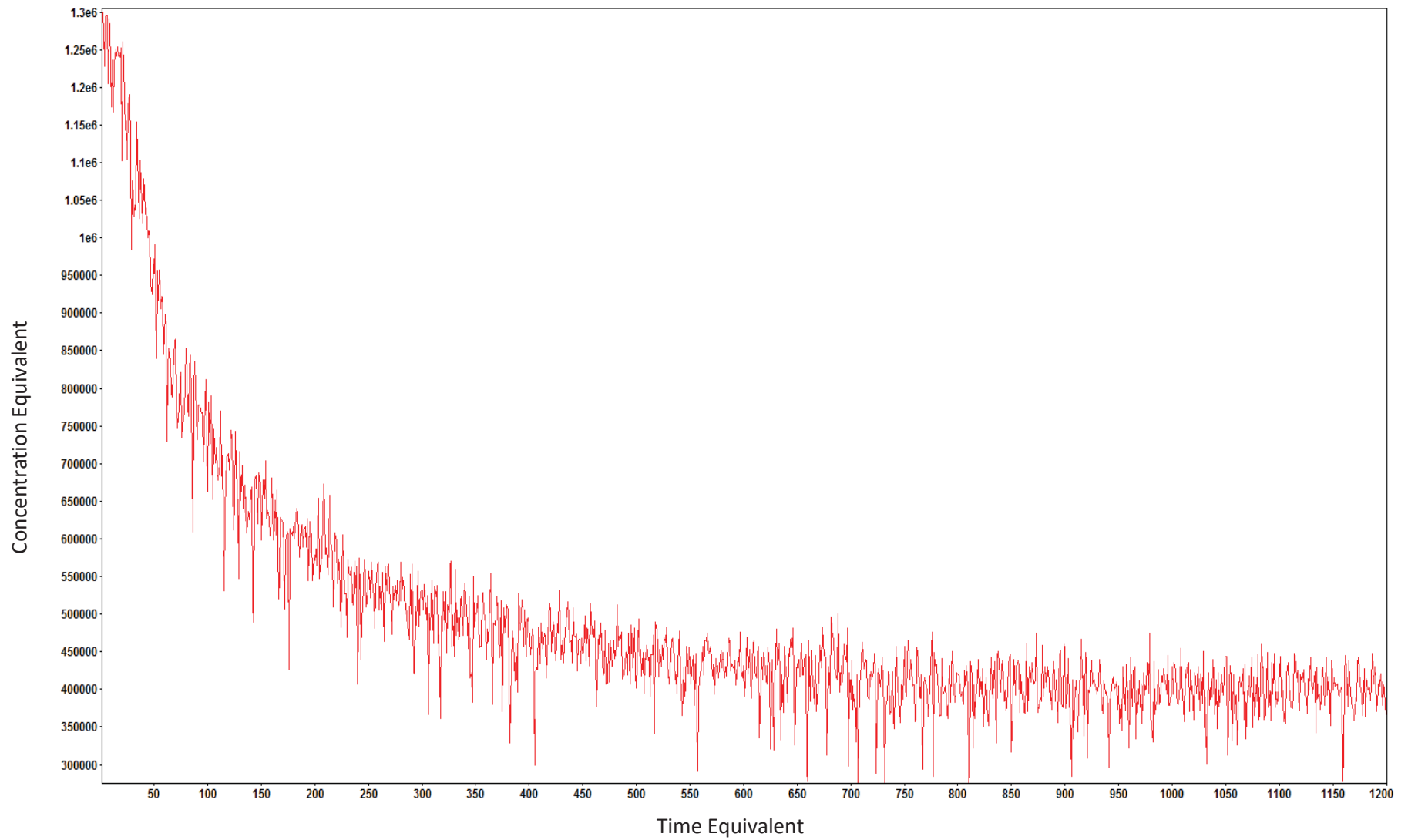


Figure 53: Experimental decay curve for TGC case with $T_{RV} = 400^{\circ}\text{F}$ (Case 4)

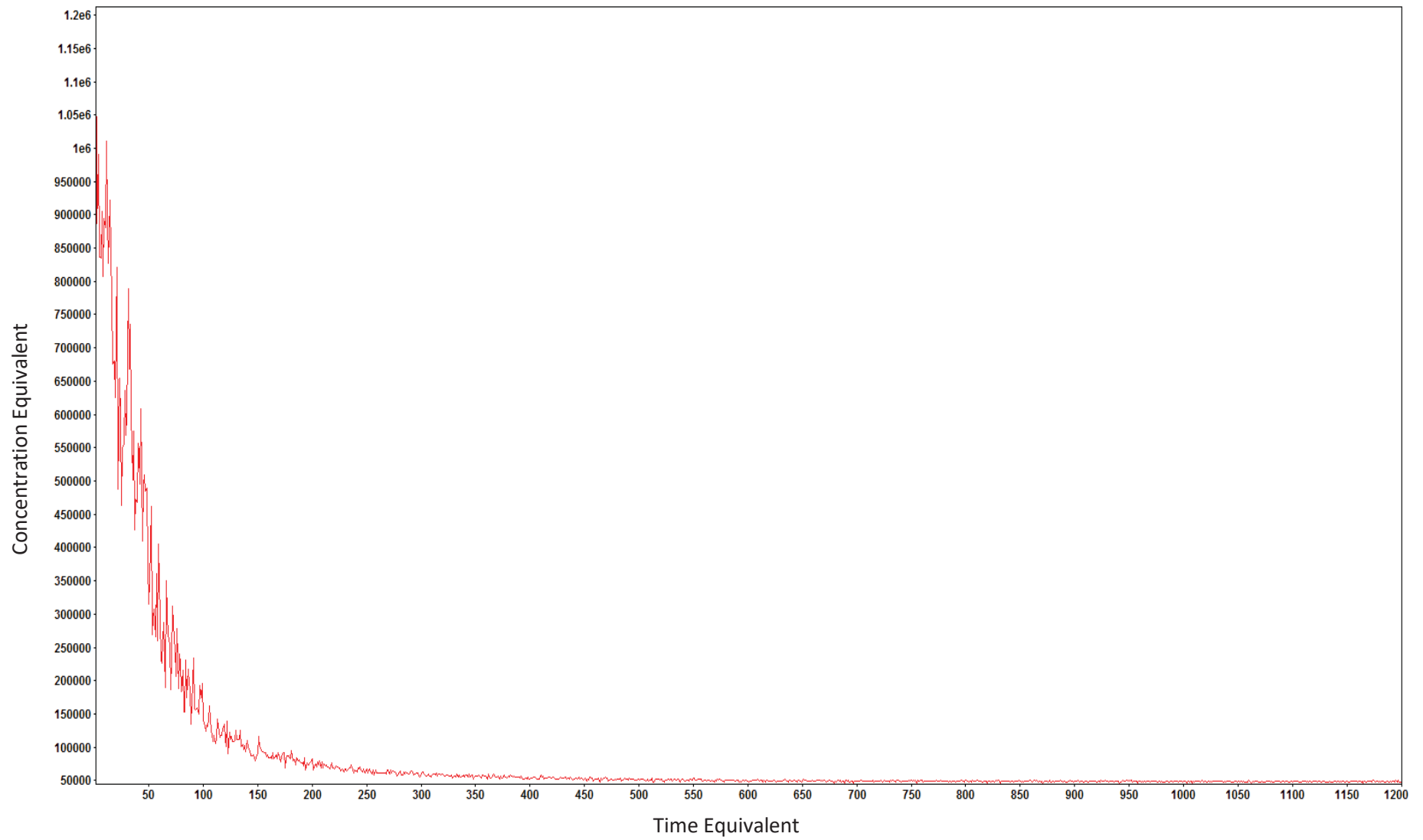


Figure 54: Experimental decay curve for TGCD case with $T_{RV} = 500^{\circ}\text{F}$ (Case 5)

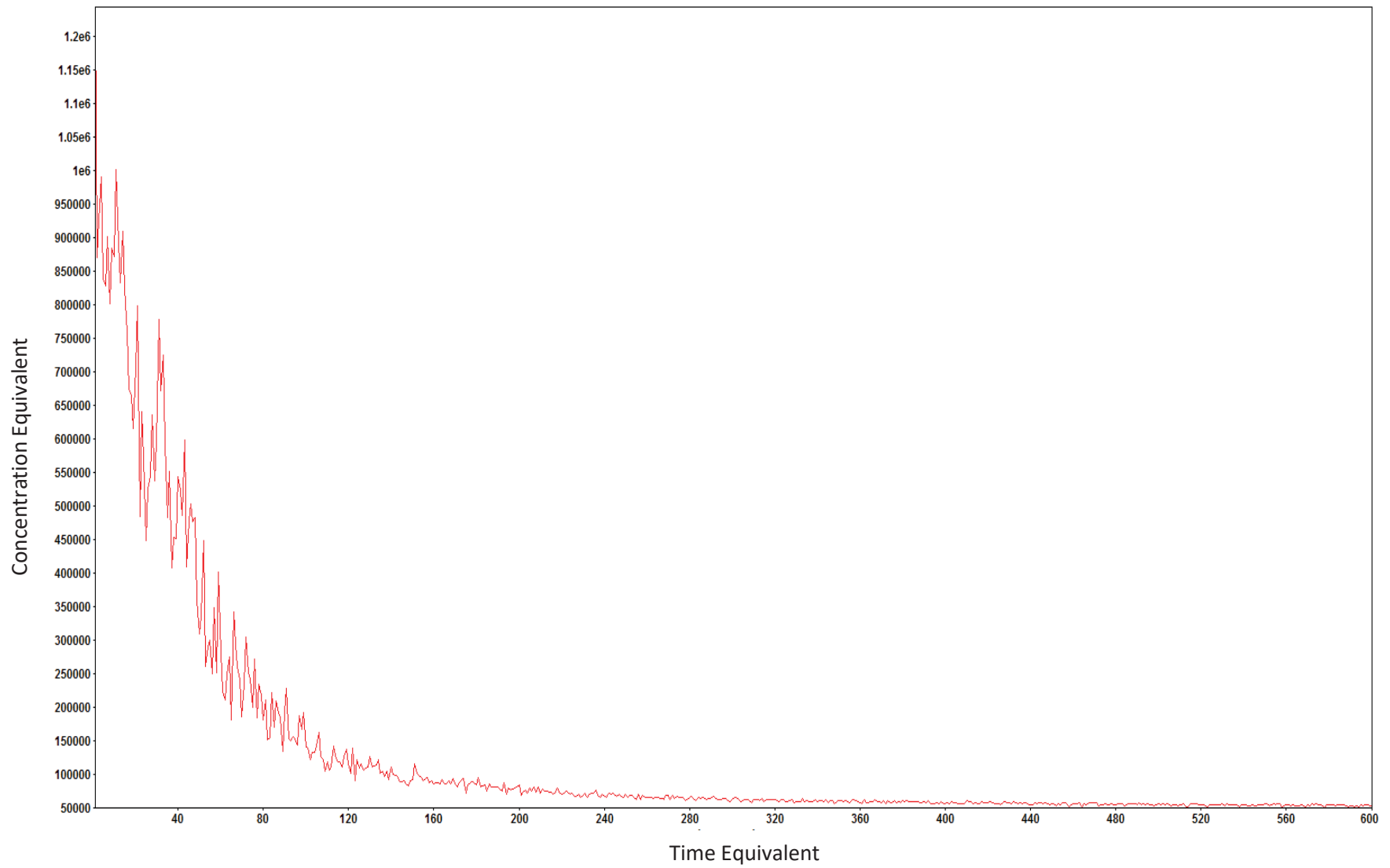


Figure 55: Experimental decay curve for TGCD case with $T_{RV} = 450^{\circ}\text{F}$ (Case 6)

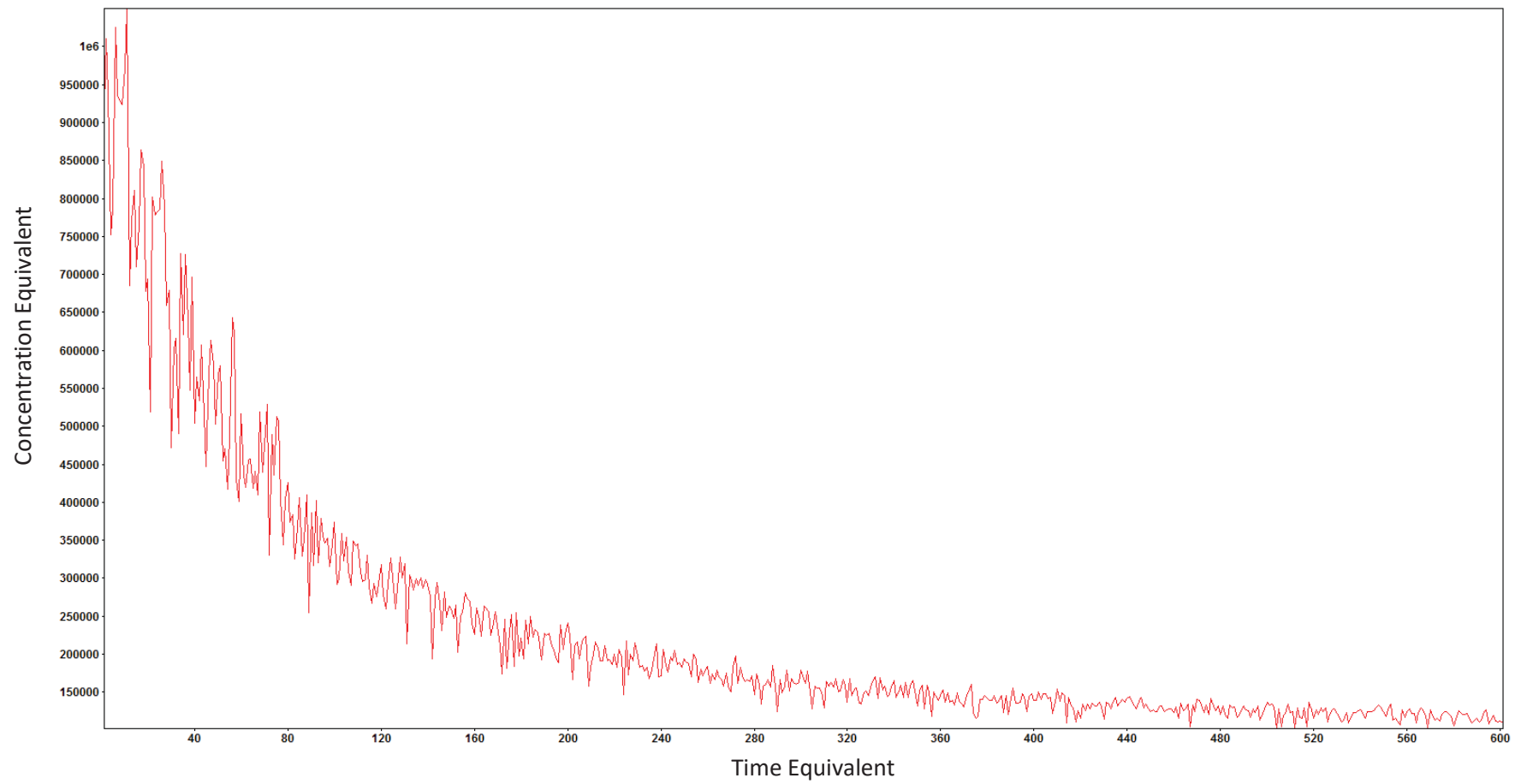


Figure 56: Experimental decay curve for TGCD case with $T_{RV} = 400^{\circ}\text{F}$ (Case 7)

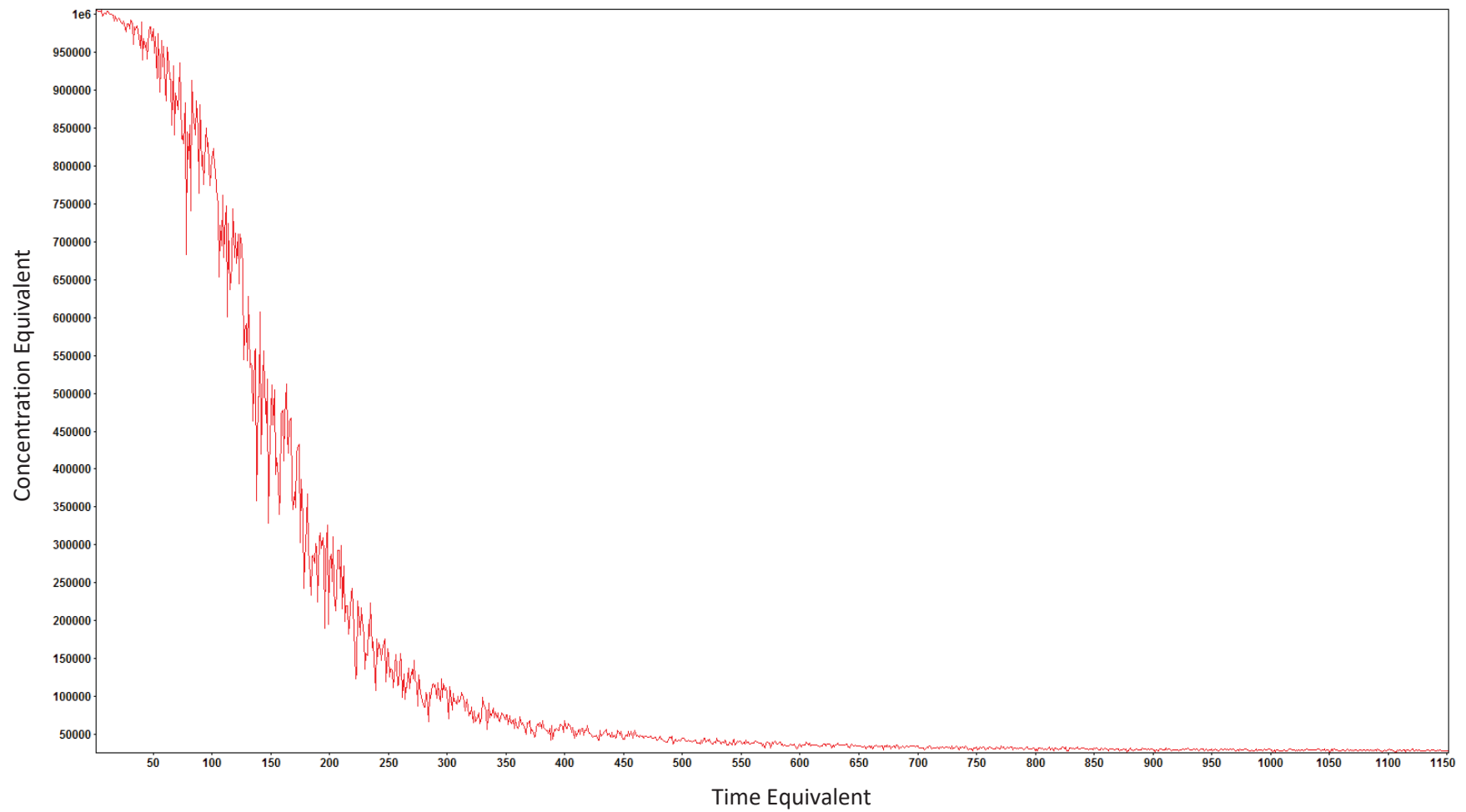


Figure 57: Experimental decay curve for TGC case with A/V ratio = 0.6 ft⁻¹ (Case 8)

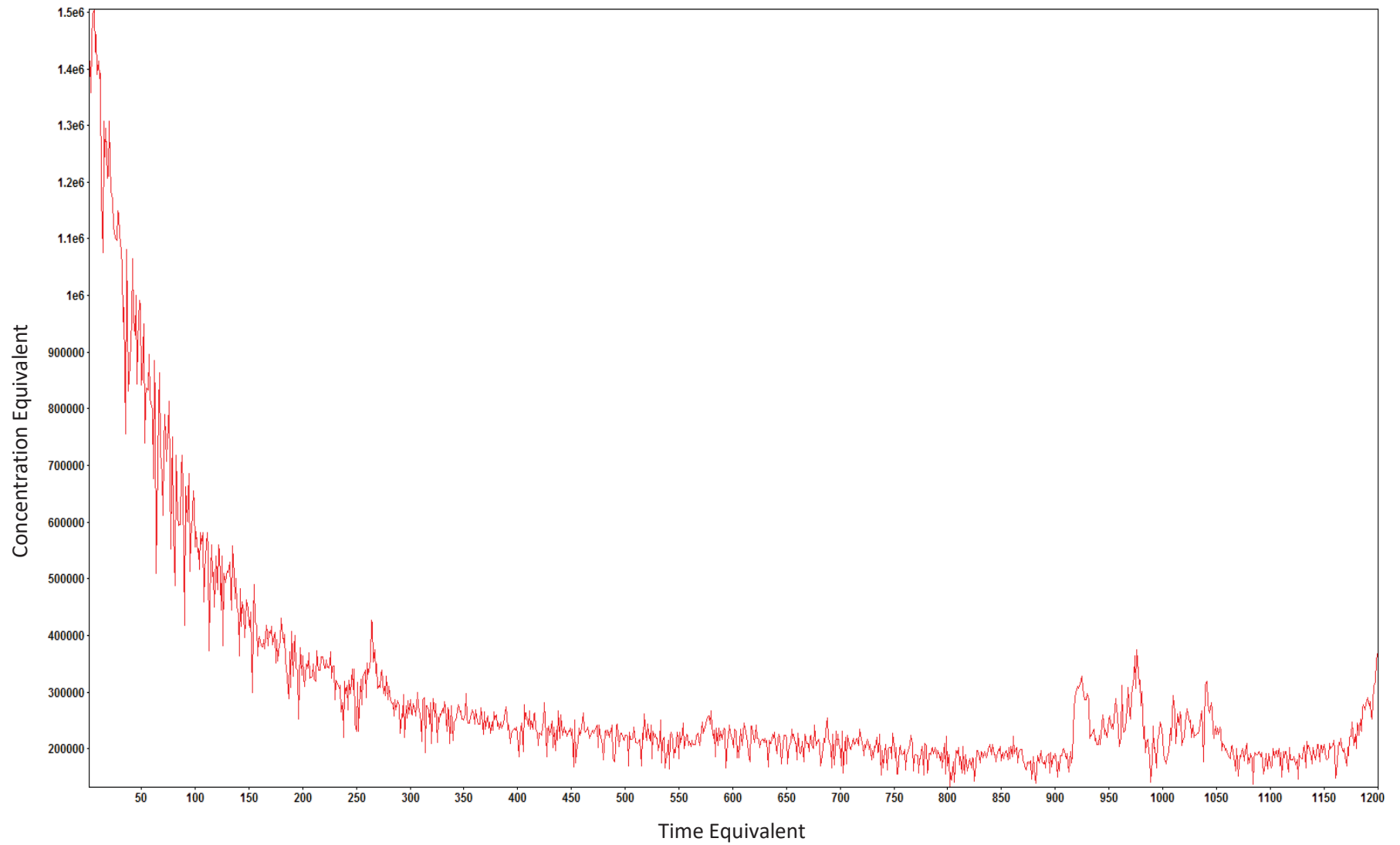


Figure 58: Experimental decay curve for TGC case with A/V ratio = 0.75 ft^{-1} (Case 9)

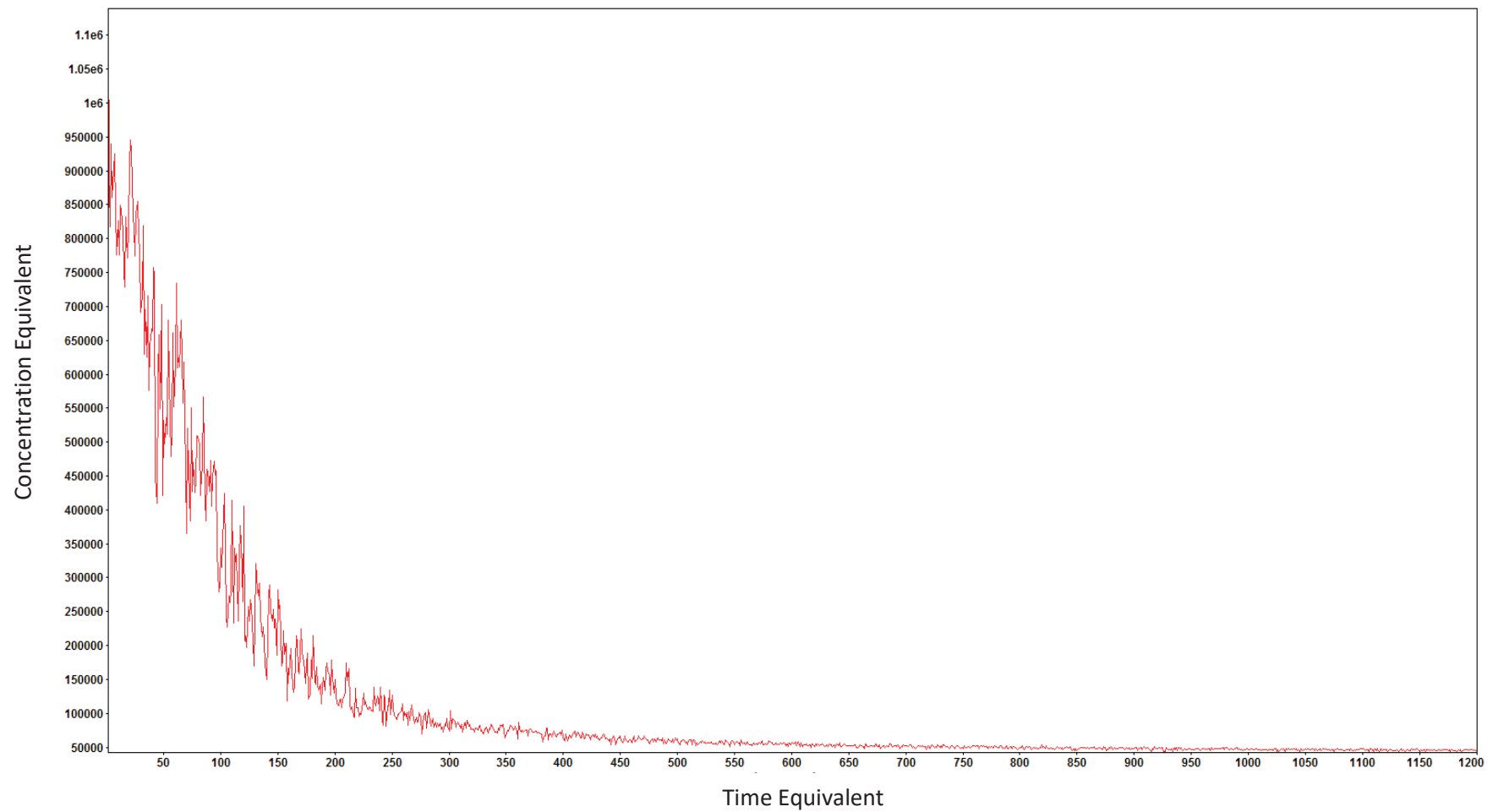


Figure 59: Experimental decay curve for TGCD case with A/V ratio = 0.6 ft^{-1} (Case 10)

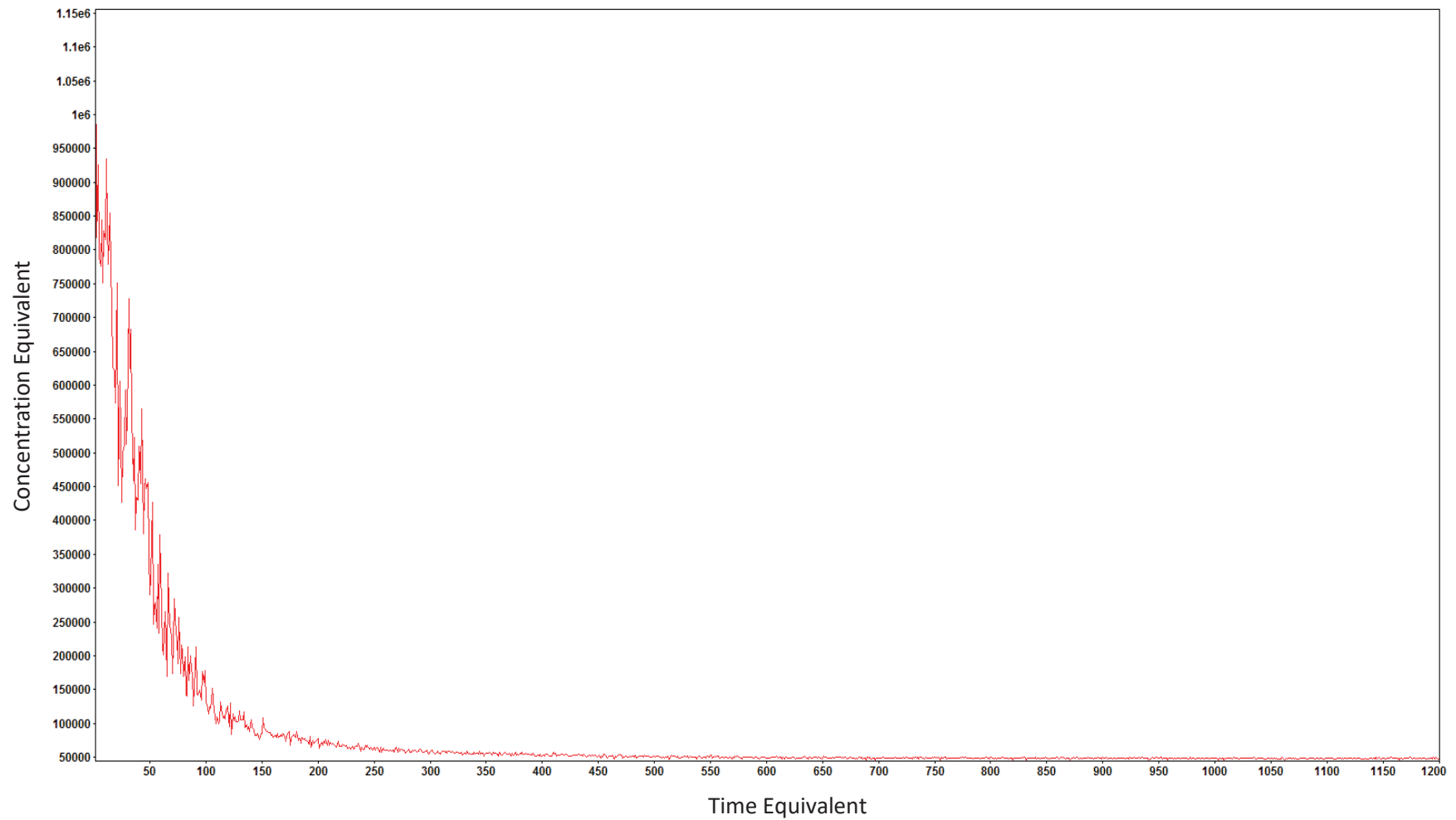


Figure 60: Experimental decay curve for TGCD case with A/V ratio = 0.75 ft^{-1} (Case 11)

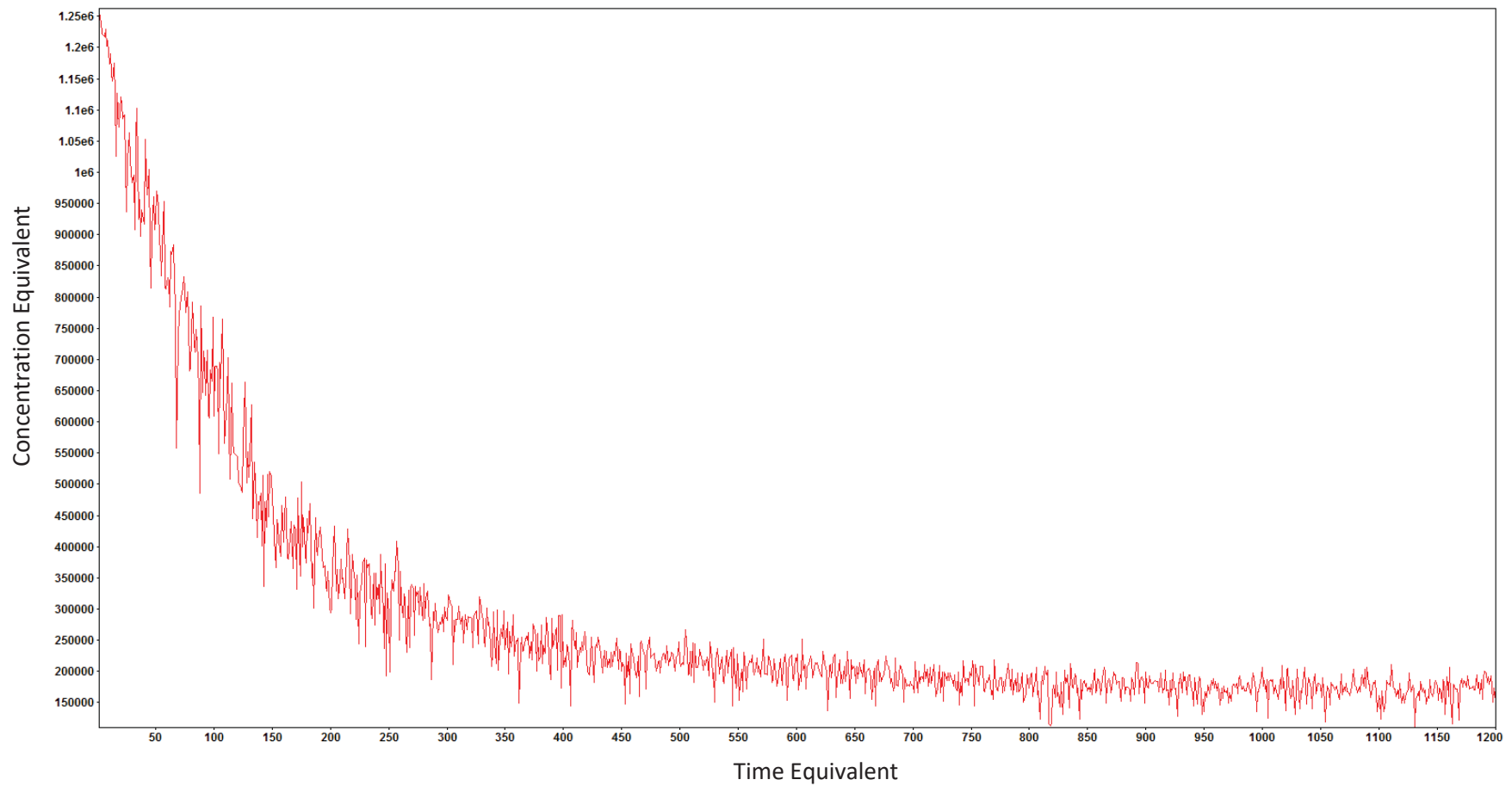


Figure 61: Experimental decay curve for TGC case with P = 65 psi (Case 12)

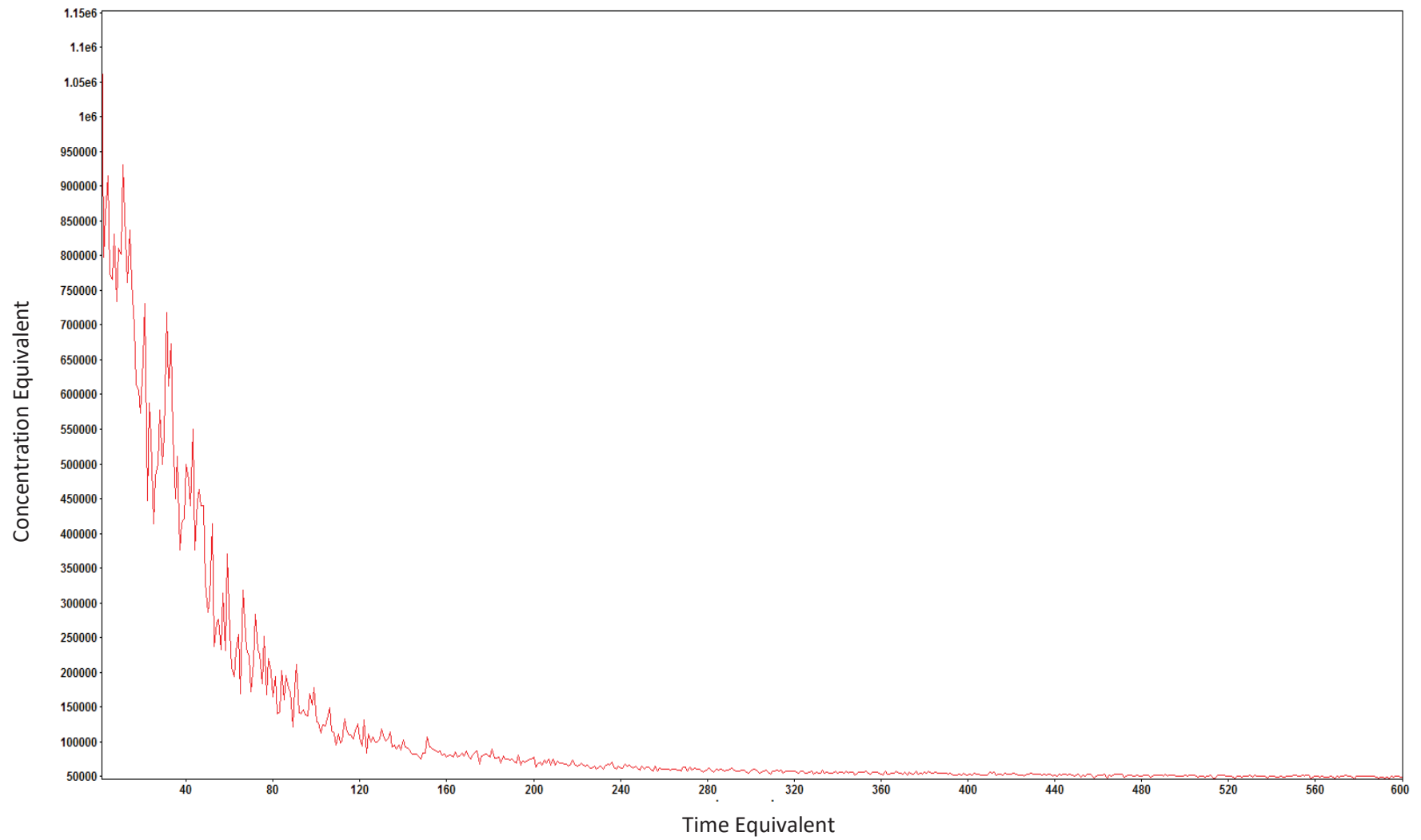


Figure 62: Experimental decay curve for TGCD case with P = 65 psi (Case 13)

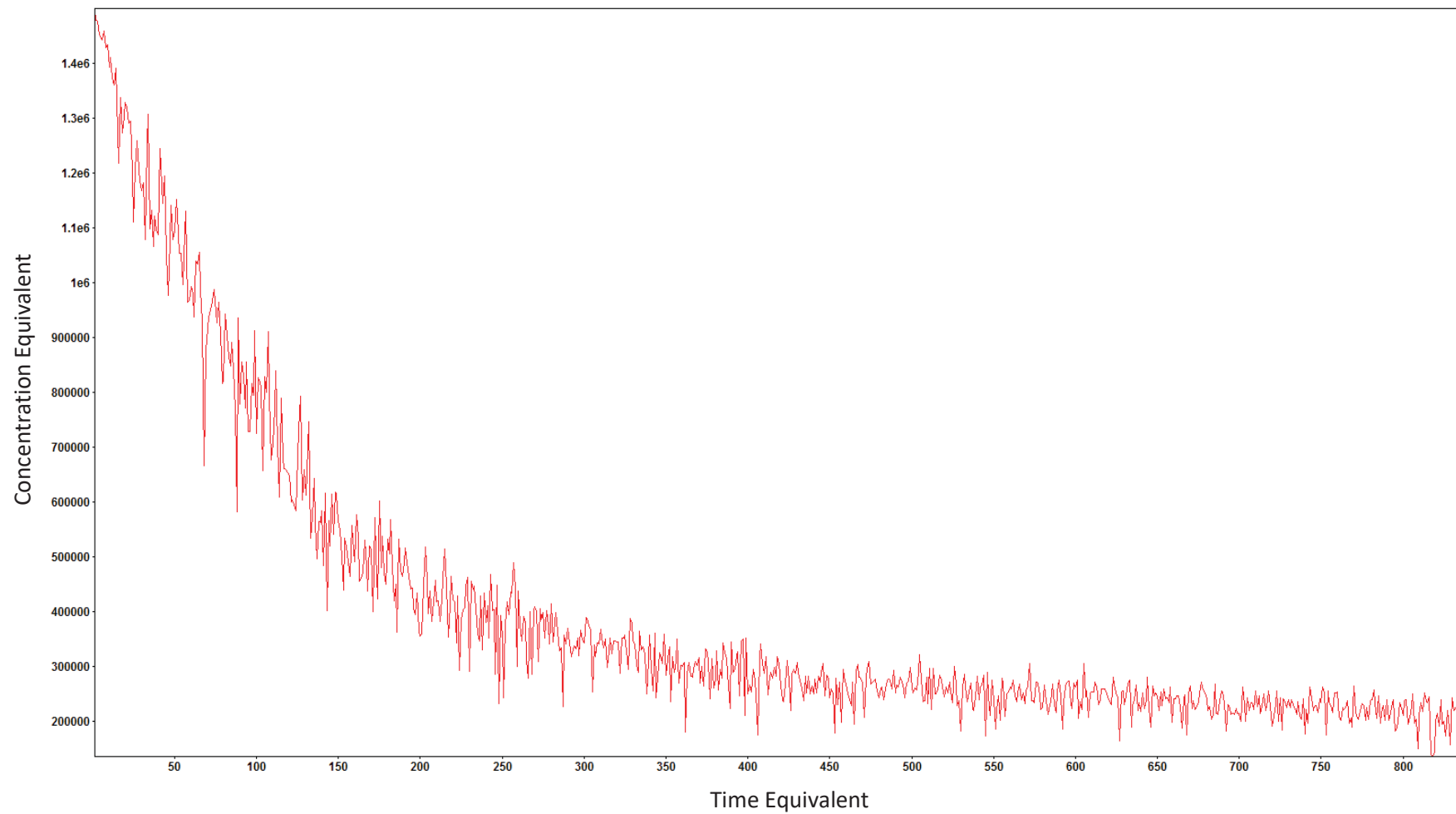


Figure 63: Experimental decay curve for TGC case with P = 20 psi (Case 14)

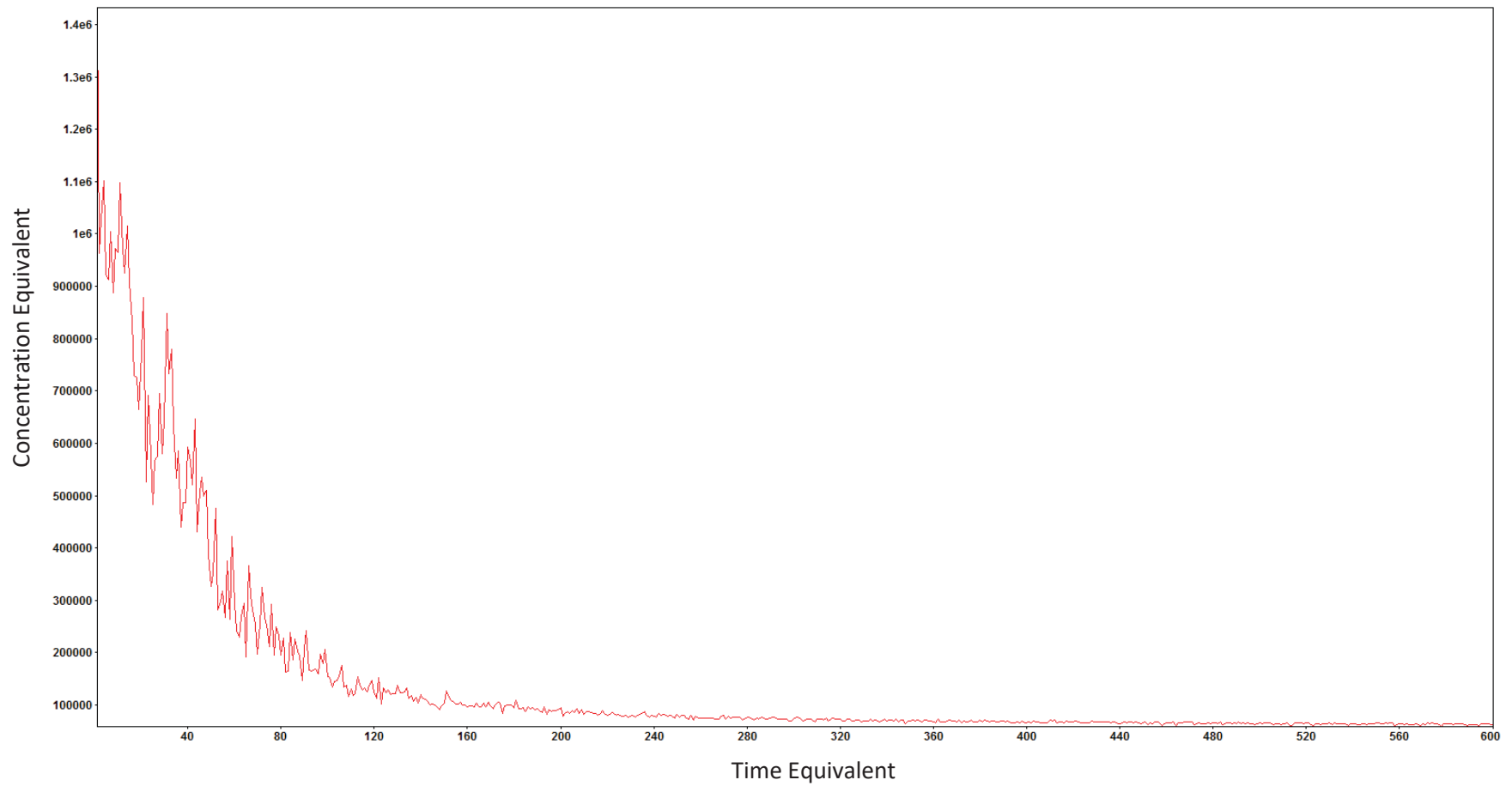


Figure 64: Experimental decay curve for TGCD case with P = 20 psi (Case 15)

Appendix D: Sensitivity study of experimental and CFD geometry

This section describes a sensitivity study performed to determine the potential difference in CFD results between simulations based on a simplified rectangular geometry and the actual experimental geometry which includes an upper and lower dome.

For the current study, the simplified geometry was used for the CFD simulations because the simplified geometry facilitates scaling of a simplified annular volume based on the A/V ratio.

A section of the CV using the actual experimental geometry as well as the simplified geometry is shown in Figure 65. As stated earlier, the sensitivity study is performed by running CFD simulations with the actual geometry, and comparing the results to simulations run with the simplified geometry.

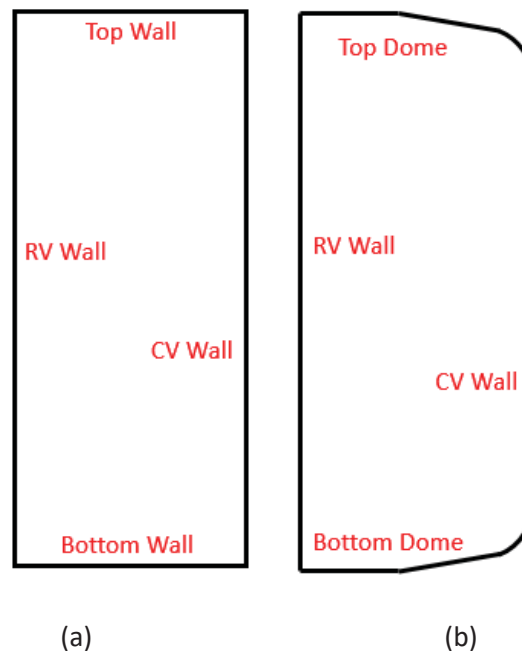


Figure 65: Cut-plane section for (a) Simplified Geometry and (b) Actual Geometry

Simulation Setup

Figure 66 shows the boundary conditions for the CFD simulations performed as part of the sensitivity analysis. The simulation case setup was identical to the baseline case with steam (case 5) to compare effects of all three particle deposition phenomena for different geometries. Table 10 summarizes the boundary and initial conditions, which are identical for both simulations.

Table 10: Boundary and Initial Conditions for both cases

Parameter	Value
Steam Mass Fraction (Y_s)	0.7
Mixture Temperature (T_g)	533 K (500°F)
Pressure (P_r)	1.379 MPa (200 psi)
Cold Wall Temperature (T_{cv})	377.4 K (220°F)
Reactor Wall Temperature (T_{rv})	533 K (500°F)

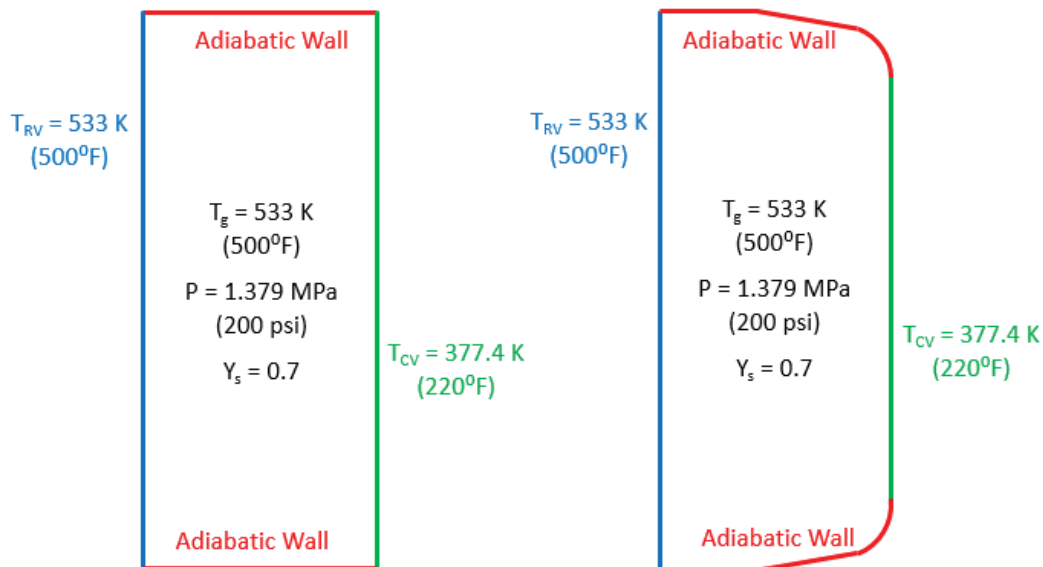


Figure 66: Simulation Setup for both cases

Results and Discussion

To assess the effect of different geometries, the parameters compared are the overall pressure and temperature traces, the velocity profiles and the normalized particle mass inside the system with respect to time, which represents particle deposition. Figure 67 and Figure 68 show the overall temperature and pressure traces respectively for both geometries. The differences between the cases are not significant.

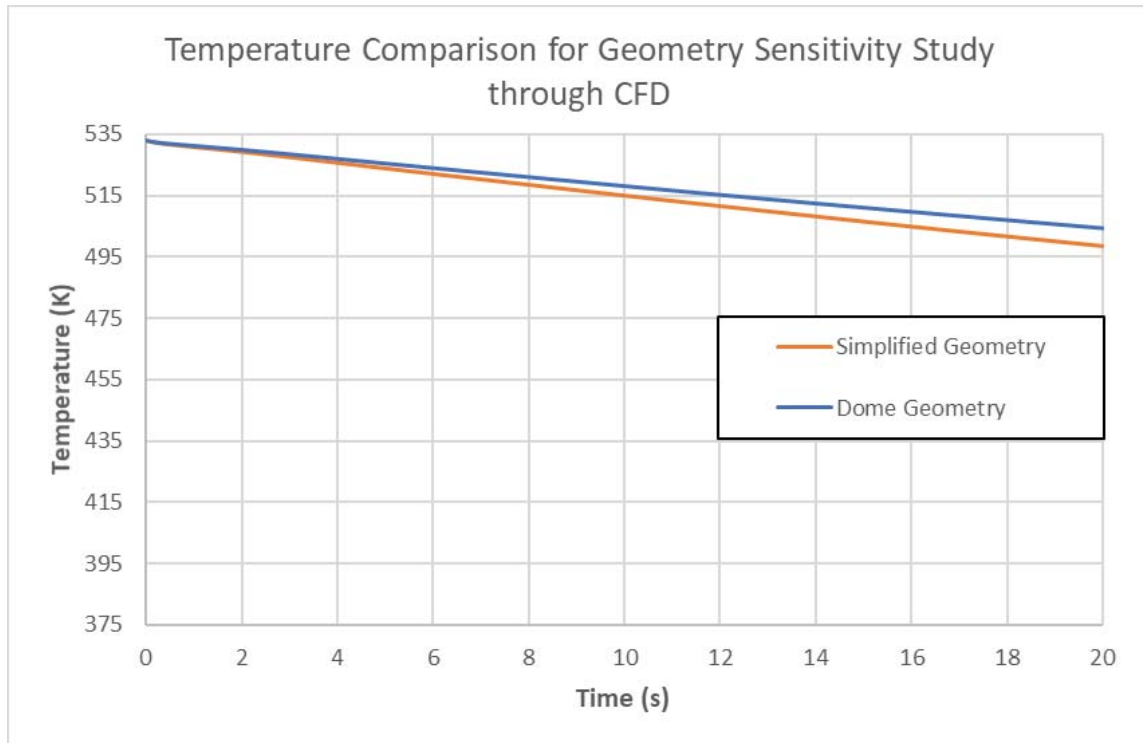


Figure 67: Temperature Comparison for Geometry Sensitivity Study

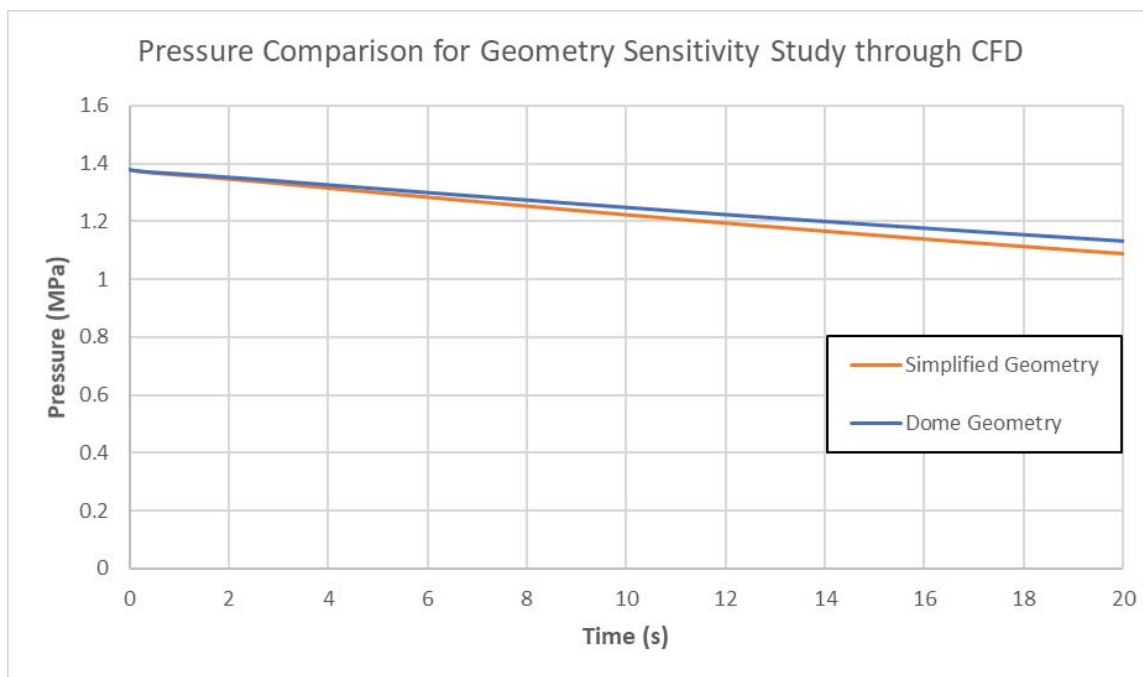


Figure 68: Pressure comparison for Geometry Sensitivity Study

Figure 69 shows the fluid velocity profiles for both geometries; it can be seen that while both geometries show similar overall convective flow, the fluid velocity is slightly higher for the dome geometry. This agrees

with the physical nature of the different geometries, whereby the dome creates less flow resistance due to the curvature.

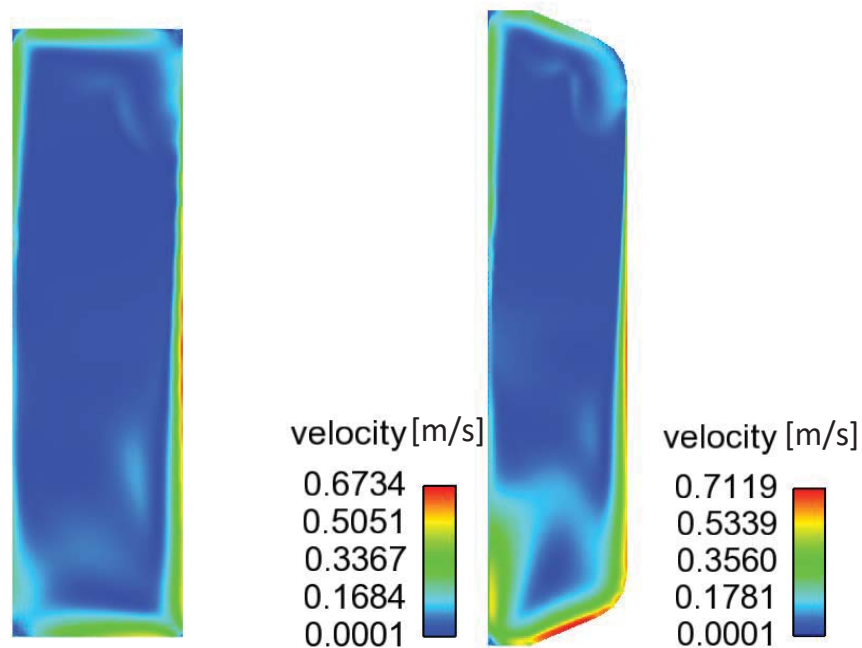


Figure 69: Velocity profiles for (a) Simplified Geometry and (b) Dome Geometry

Figure 70 compares the particle decontamination curves from both geometries. It can be seen that the normalized particle decontamination rate is slightly slower with the dome geometry, by about 0.2%/s. This difference may be a result of increased turbulence in the simplified geometry, resulting from flow hitting the CV vertical wall and floor at right angles as opposed to the obtuse angular approach with the dome geometry. The differences between particle deposition due to changes in geometry are not significant, indicating that the use of the simplified geometry is justified.

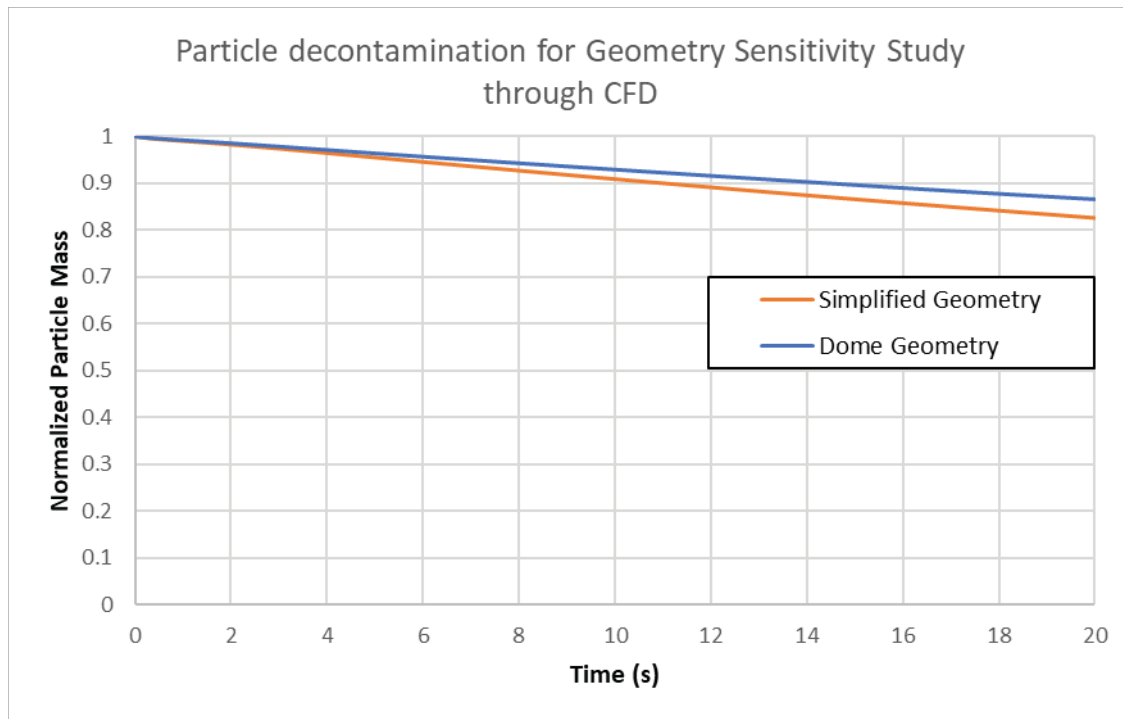


Figure 70: Sensitivity Study for actual and simplified experimental geometries

The differences between particle decontamination in both geometries can be addressed by calibration of the results from the simplified to the actual experimental data, as is done throughout the current study. This results in mitigation of the errors that arise due to differences in the two geometries.

Conclusions

The differences in particle deposition and thermal-hydraulic parameters are not significant for the simplified and the dome geometries, thereby justifying the use of the simplified CV geometry for predicting particle deposition through CFD simulations. The use of the simplified geometry facilitates scaling of the results and increases computational efficiency.

Appendix E: Application of Results – Supplemental Requirements for Aerosol Deposition Estimation Codes

The experimental and analytical CFD iPWR containment aerosol deposition work performed under this study can be directly applied to iPWR SMR designs in calculating aerosol decontamination factors. This section provides a summary of recommendations that could further improve aerosol deposition calculations in safety analysis codes based on the findings of this study. Note that this is not a comprehensive list; however, this section identifies additional practices to augment standard methods to further improve modeling accuracy. The requirements are based on insights developed over the course of this study, and specifically from the development of the CFD model. Hence, the CFD model development report (EPRI, 2017b) submitted as part of Phase 2a of this project, is used as a reference.

Particle Distribution Modeling

Requirements to improve particle distribution modeling in codes directly solving the transport equations include the following:

- **Apply the Eulerian approach to represent particle distribution.** Taking advantage of rapid achievement of steady state conditions in a iPWR environment, the Eulerian approach may be used to represent particle distribution rather than a Lagrangian approach. The Eulerian method treats the particle phase as a continuum and develops its conservation equations on a control volume basis and in a similar form as that for the fluid phase. The Lagrangian method considers particles as a discrete phase and tracks the pathway of each individual particle. In the iPWR environment, the particle phase behaves more like a continuum. The Eulerian approach needs less computing time than the Lagrangian method, because the latter tracks the development of each particle and the particle number needs to be sufficiently large to ensure statistical stability (Zhang & Chen, 2007).
- **Use discrete models for particle size distribution to account for particles of different diameters.** Separation of the particle diameters is accomplished by treating particle sizes as arrays or bins. This allows for rapid access to each array at deterministic time steps and increase calculation efficiency.
- **For each particle diameter, specify unique particle properties as part of model setup.** Particle properties include: (1) particle density and associated physical properties, (2) shape factors for non-spherical particles, (3) diffusion boundary layer thickness for smaller particles, (4) particle sticking coefficients to support agglomeration by gravitational settling, and (5) particle diameter. Detailed particle properties allow a wider range of deposition mechanisms to be activated, such as Brownian motion and turbulence.
- **Explicitly account for Cunningham Slip Correction Factor dependencies on Knudsen numbers and the particle diameter.** This enhances an understanding of deviations in continuum mechanisms from which the theoretical constructs for the depositional velocities are derived. This improves the accuracy of the deposition velocities for gravitational settling, thermophoresis and most importantly, diffusiophoresis mechanisms (NRC, 1996).

- **Perform direct calculation of deposition-related parameters.** CFD models demonstrated that results such as particle concentration and distribution for various particle diameters could be calculated simultaneously. Particle concentration is expressed as an array of multiple particle diameters, which may potentially eliminate the need for “averaging” measures for particle diameter characterization such as an AMMD (Aerosol Mass Median Diameter) and the geometric standard deviation (GSD).
- **Calculate the distribution of particle concentration within a specified volume.** Performing these calculations isolates locations inside the CV where particle concentration is high or low and compares the distribution of particles for various diameters. An illustration of implementing this requirement is shown in Figure 71. This visualization is particularly useful in understanding the influence of the particle size on the deposition and may be useful in refining the particle properties during model set up.

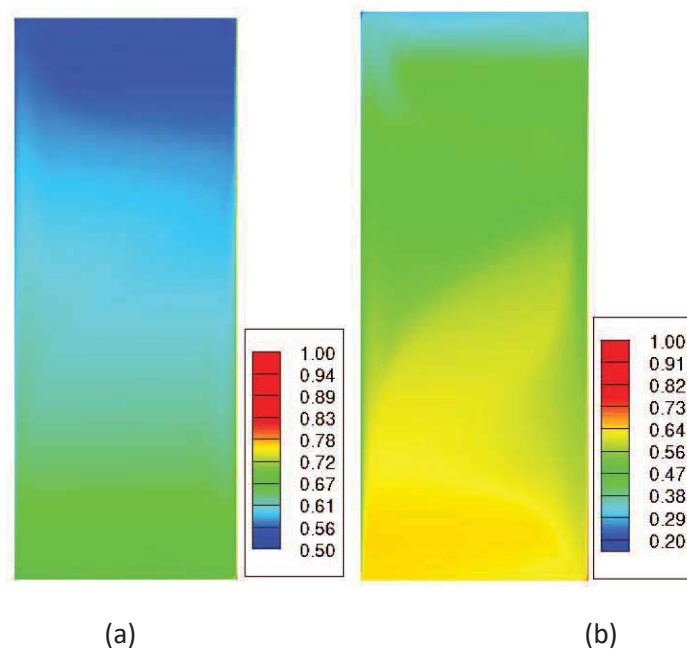


Figure 71: Distribution of particles inside the CV for (a) 1 μm and (b) 10 μm diameter particles (unitless, representing number density) (EPRI, 2017b)

Diffusiophoresis Deposition Models Using Stefan Flow and Slip Coefficient Correction Factor

Requirements to enhance diffusiophoresis deposition models are based on the conclusion that Stefan flow-based diffusiophoresis theoretical models provide greater accuracy and resolution of diffusiophoresis phenomena (CEC, 1988). Estimation of particle loss requires slip correction based on the Knudsen number, Kn . The Knudsen number has values that place the fluid in a slip flow regime.

Table 11 illustrates the rationale for this requirement. Knudsen number values are calculated for a range of particle diameters and gas conditions applicable to iPWR post-accident conditions; the aerosol particle diameters are between 1 μm and 10 μm and the gas temperature is between 293 K (68°F) and 575 K (575 °F). Figure 72 illustrates the range of Kn for the specific case of the gas temperature of 500°F at 200 psi for various particle diameters, d_p .

Table 11: Knudsen number values for particles 1-10 μm at different gas conditions

Gas Temperature [°F]	Gas Pressure [psi]	λ^* [μm]	d_p [μm]	Kn
68	14.5	0.0665	0.1	1.3306
			1	0.1330
			5	0.0266
			10	0.0133
250	29	0.0487	0.1	0.9740
			1	0.0974
			5	0.0195
			10	0.0097
500	200	0.0094	0.1	0.188
			1	0.0188
			5	0.00376
			10	0.00188
575	200	0.0110	0.1	0.2214
			1	0.0221
			5	0.0044
			10	0.0022

*Calculated with Aerosol Calculator by Paul Baron (2001)

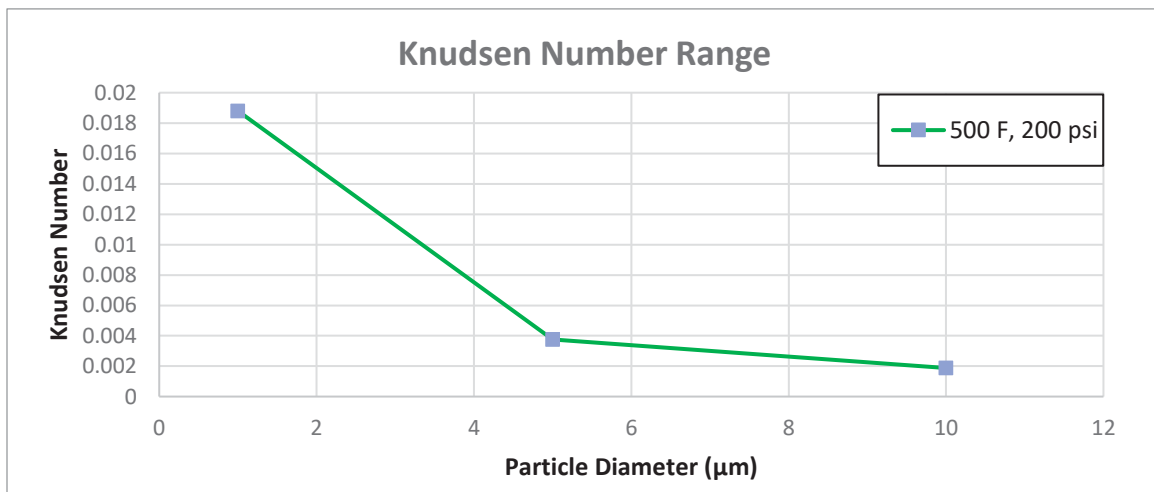


Figure 72: Knudsen Number Range for 1 – 10 μm particles

CFD modeling substantiated the requirement to include the Cunningham slip correction factor to account for the effects of particle diameter on diffusiophoresis. The Cunningham slip correction factor addresses the non-sphericity of particles and extends application of the diffusiophoresis velocity equation into the small particle regime. This is shown in the following equation for diffusiophoresis velocity (NRC, 1996):

$$V_d = -\frac{C_c}{\chi} \left[\frac{\chi}{C_c} + \sigma_{12} \left(1 - \frac{P(H_2O)}{P_T} \right) \right] \frac{D(H_2O)}{P_T - P(H_2O)} \nabla P(H_2O)$$

Where C_c is the Cunningham slip factor, χ is the dynamic shape factor, $D(H_2O)$ is the diffusion coefficient of water in air, $P(H_2O)$ is the partial pressure of water, P_T is the total pressure, and σ is the scattering kernel.

Gravitational Settling Calculations with Actual Particle Sizes

Requirements to enhance gravitational settling calculations are based on the experimental results which demonstrate that using an average particle size tends to overestimate the contribution of gravitational settling to overall particle deposition rates. The reason for this is that the Knudsen number for particle sizes from 1 to 10 μm decreases exponentially as sedimentation velocity increases by two orders of magnitude (Sher & Hobbins, 2011). Using actual particle sizes instead of average particle sizes shows a considerable decrease in decontamination rates for particles below 5 μm , as shown in Figure 73.

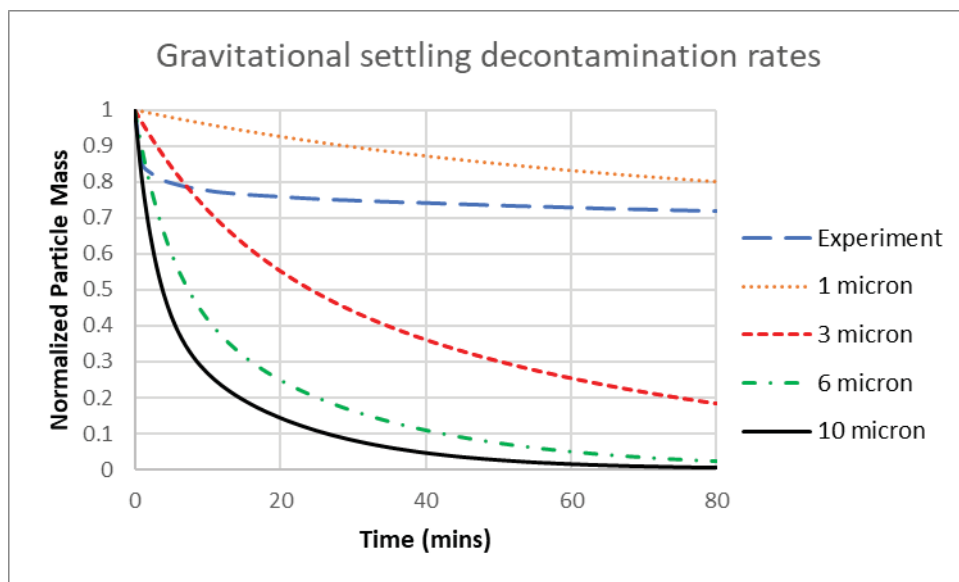


Figure 73: Gravitational settling decontamination rates for experimental and simulated cases

Modeling the Variations in the Thermal-hydraulic Environment and Accurate Calculations of Thermal-hydraulic Parameters

Requirements to enhance modeling of variations in the thermal-hydraulic environment and accurate calculations of thermal-hydraulic parameters are based on the following CFD modeling and experimental observations:

- **Stratification of the thermal-hydraulic environment into zones of influence.** Stratification of the CV fluid domain into three zones offers greater realism and modeling granularity. The zones are:

the superheated zone (containing superheated steam), the saturated zone (separated from the superheated zone by the dew point temperature plane and containing a steam concentration gradient) and the condensation zone (which includes the liquid-gas interface near the containment vessel wall). CFD modeling demonstrated this stratification. These stratified environments influence thermophoresis, diffusiophoresis and convective flows, both thermal-hydraulically and geometrically. A change in the containment geometry affects the size of these environments and hence the deposition efficiency of the various phenomena acting in the environments. For example, the ratio of the width of the superheated region relative to the saturated and condensation regions in large containment vessels is several orders of magnitude higher than small containment vessels. Hence the effectiveness of the transport mechanisms from the hot RV to the cold CV are significantly reduced as the containment vessel gets larger. The relevant transport mechanisms in the superheated zone include convective flow and to a lesser extent, thermophoresis, which both move the particles through the superheated to the saturated and condensation zones, where deposition mechanisms such as diffusiophoresis and inertial impaction further assist in surface deposition.

- **Calculation of local thermal-hydraulic parameters.** To provide accurate thermal-hydraulic values used for the calculation of deposition velocities, CFD modeling provides specific nodal values throughout the domain. While this may not be of much importance for the pressure values which hardly fluctuate, it is significant for temperature and steam concentration. Specific values allow more accurate calculation of local temperature and steam concentration gradients and thereby better predictions for thermophoresis and diffusiophoresis respectively. Figure 74 and Figure 75 show the distribution of temperature and steam concentration inside the vessel respectively.

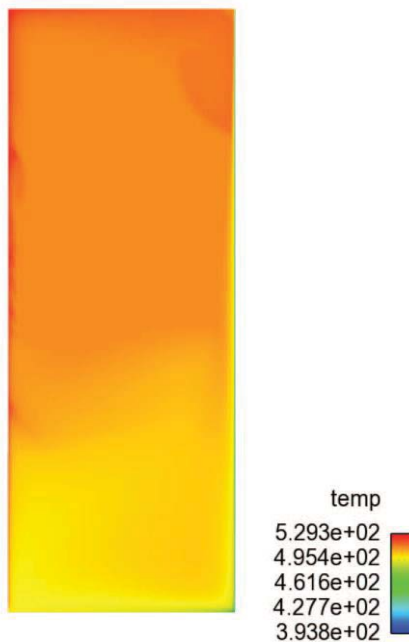


Figure 74: Temperature [K] distribution inside the CV (EPRI, 2017b)

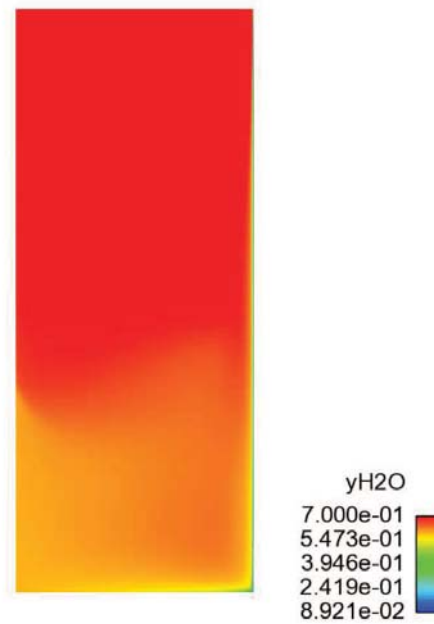


Figure 75: Steam concentration distribution inside the CV (EPRI, 2017b)

- Model particle velocities throughout the domain.** CFD modeling allows calculation of specific particle velocities throughout the fluid domain, and not just at boundary layers and depositional surfaces. This is achieved by implementation of a drift-flux model, which couples the effects of individual particle velocities due to thermophoresis, diffusiophoresis and gravitational settling, thereby providing a resultant particle velocity relative to the flow. The total particle velocity can thus be calculated from this relative particle velocity and the flow velocity, which allows the incorporation of the effects of convective flow. Particle velocities associated with specific thermal-hydraulically stratified zones can also be calculated.

Modeling Phenomena Fluctuations due to Changing Thermal-Hydraulic Parameters

Requirements to enhance modeling of phenomena fluctuations due to changing thermal-hydraulic parameters are needed to deal with fluctuations that affect thermal and steam concentration gradients and the effectiveness of the deposition phenomena. For instance, at low pressure, steam condensation may cease after a period due to unfavorable conditions for condensation (NEA, 2009). This process may stop diffusiophoresis, which slows down the decontamination process.

Modeling Convective Flow as a Particle Transport Mechanism

Based on the CFD simulations and the experiments, convective flow has been identified as a significant particle transport mechanism. The presence of the convective flow further substantiates the significance of a higher surface-area-to-volume ratio for increased deposition efficiency (EPRI, 2017b). Figure 76 shows CFD simulations of convective flow in the CV volume.

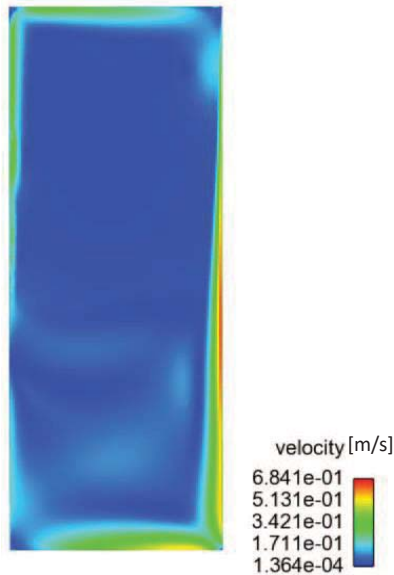


Figure 76: Convective flow shown by velocity field [m/s] inside the CV (EPRI, 2017b)

Convective flow facilitates decontamination by creating a turbulent environment due to the mixing that ensues. The scaling section of this document identifies correlations for aerosol removal rates due to turbulence and impaction to characterize the aerosol removal associated with the turbulent environment. It should be noted that these correlations had been identified by the NRC as potentially being applicable to reactors with relatively smaller containment vessels (NRC, 1996); however, these correlations were not applied in decontamination analysis of these reactors (Westinghouse Electric Co., 2008). The significance of convective flow-based turbulent deposition has also been identified in prior studies, as described in the following excerpt (NEA, 1990):

The primary system codes calculate the effects of carrier gas flow and inertia by using accepted models. (However, the treatment of bends and the deposition in turbulent flow have to be improved in most codes.) These effects are rarely considered in containment calculations, partly because they are not thought to be very important and partly because thermal-hydraulic codes for the containment do not supply the necessary information.

NRC NUREG/CR-6189 (NRC, 1996) further indicates the significance of turbulence driven by convective flow:

The QUEST study showed that turbulence of sufficient magnitude had a considerable effect on the rate of aerosol coagulation. Indeed, uncertainty studies by Helton et al. have shown that the turbulent energy dissipation rate is an important parameter in the prediction of aerosol behavior. Most large-scale tests of aerosol behavior in the reactor containment have not attempted to simulate the turbulence to be expected in the containment during a reactor accident. Turbulence could be of even greater importance in future generations of nuclear power plants employing passively cooled containments. It would seem, then, to be appropriate to include this effect.

The inclusion of convective flow as a particle transport mechanism for iPWR containment vessels has been shown to be significant. Specifically, the CFD code has the following capabilities with respect to convective flow, which should be considered for other aerosol deposition models:

- **Convective flow effects on particle transport by inclusion of buoyancy models:** Particles are transported to deposition surfaces by both phoretic and convective flow phenomena. Inclusion of convective flow as a transport mechanism to move particles to deposition surfaces is especially significant for smaller particles ($<5\ \mu\text{m}$) as these tend to stay suspended for significantly longer periods when sedimentation is the only active mechanism. This was observed in the current study by comparing adiabatic and non-thermal gradient experiments (G) with thermal gradient experiments (TGC), which drive convective flow.¹¹ Small particles especially are removed at a significantly faster rate, as can be observed by the difference between G and TGC experiments, which are presented in the results section of this report. Smaller particles stay suspended for longer in the vessel with G only. It should be noted that particle transport to deposition surfaces by convective flow does not equate to loss at the surfaces. This is based on measurement of wall deposition in dry conditions as compared to wet conditions. The measured particle deposition on the walls by coupons for wet conditions were approximately 6 times greater than dry conditions. This is attributable to both diffusiophoresis acting as a transport mechanism bringing more particles to the wall, and net horizontal forces at the boundary layer, which include turbulent inertial deposition, diffusiophoresis and to a lesser extent, thermophoresis.
- **Significance for low-pressure environments:** The effects of convective flow on particle transport are also significant in a low-pressure environment. Despite the presence of steam, condensation may stop after some time in a low-pressure environment (considering other external conditions as well). This low-pressure environment may be a limiting factor for SMR designs that are at a vacuum state during reactor operation, and which will subsequently have a lower CV pressure in the event of an accident. This limits steam condensation and prevents particle deposition through diffusiophoresis. However, particle deposition can proceed in the presence of steam, aided by convective flow, which serves to move the particles closer to deposition surfaces, where gravitational settling and thermophoresis are still available as deposition mechanisms. Thus, relatively high rates of decontamination can still take place in a wet, low-pressure environment without diffusiophoresis.
- **Considerations of effects of convective flow on re-entrainment and resuspension:** Convective flow could potentially create particle resuspension if the currents are strong enough to overcome surface tension and the weight of the particles. The effects of convective flow on

¹¹ Test cases are named by deposition mechanisms in effect, hence G is for gravitational, TGC is for Thermophoresis, gravitational and convective, while TGCD includes diffusiophoresis.

particle uplift should be further investigated and has been indicated as an area for further research.

Modeling of Turbulent Inertial Impaction

Enhanced modeling of convective flow-induced turbulence acting as a transport and deposition mechanism are needed. The transport effect can be characterized by adding turbulence aerosol removal coefficients to existing aerosol removal correlations, as described in the Scaling section (Section 5) of this report. Regarding particle deposition through impaction, for flow in the turbulent diffusion-eddy regime, turbulence drives the particles toward the wall and if the particle inertia is sufficiently large, it will penetrate the laminar boundary layer. However, if the flow is in the inertia-moderated regime, the particle inertia would be too high to be driven into the laminar boundary layer (Sher & Hobbins, 2011). Hence, this effect can also be characterized by inclusion of the inertial deposition aerosol removal rate described in the Scaling section (Section 5) of this report.

Appendix F: Additional Research Questions

To ensure applicability of research outcomes, this project elicited input from stakeholders including an independent reviewer, iPWR designers, the Department of Energy, and the Nuclear Regulatory Commission. A series of project review meetings were held, which resulted in improvements to the experimentation plan.

In addition to the experimentation-related modifications, the theoretical constructs for the deposition mechanisms were also revised. Specifically, an additional particle transport and deposition mechanism was included for convective flow-related inertial deposition. The effects of convective flow on particle transport were also incorporated into the CFD model through the drift-flux model (EPRI, 2017b). To address comments related to simulant selection, which include particle size, distribution, agglomeration and aerosol composition, the applicable references were reviewed to ascertain applicability, which also included confirmation of iPWR vendor inputs for simulant selection.

The following delineates research questions that were posed during meetings. Although meriting future consideration, these items were evaluated and determined not to detract from the applicability of the experimental data, correlations, and CFD analytical results that have been presented in Sections 3, 4, and 5 as well as Appendices A, B, C and D of this report.

- i. **Characterize the expectation for re-entrainment / resuspension (*recommended by NRC*):** This comment is applicable to floor-deposited particles due to convective flows. It has been stated that convective flow is a significant particle transport mechanism, which aids deposition. It would be useful to establish the potential for this transport mechanism to adversely affect deposition through particle uplift. It is recommended that this issue be further analyzed through experimentation and simulation. The CFD model may be used in future work to evaluate the net vertical force from gas molecule momentum due to convective flow (upward) and particle weight and surface tension (downward). The experimental loop and laser system can be applied to track specific tracer particles to determine potential for re-entrainment.
- ii. **Assess the significance of particle agglomeration / coagulation (*recommended by NRC*):** This comment is applicable to the pressurization phase of the accident transient, where smaller particles may agglomerate to larger sizes. It should be noted however, that the current study assumes no particle growth and that the accident transient is in the post pressurization aerosol depletion phase. This assumption is conservative because larger particles would settle at a faster rate.

The aerosol material was chosen partially to limit the amount of agglomeration or coagulation of particles. The standard assumption in nuclear aerosol codes is that when aerosol particles come into contact with other aerosol particles, they remain together. Particle growth by agglomeration changes the aerosol size distribution and will impact the gravitational settling rate. Agglomeration has the potential to be very significant at high particle concentrations. It is beneficial to assess the likelihood of agglomeration and coagulation. This is significant for validation of current assumptions around particle transport and application of the CFD drift flux model. Smaller particles may agglomerate with larger particles and settle faster.

- iii. **Characterize impaction at various locations (*recommended by NRC and iPWR vendor*):** The current study included an assessment of convective flow-related impaction in dry and wet conditions at one location. The selected location was at the upper quadrant of the CV volume, where convective flow impaction was expected to be highest. The NRC requested a further evaluation of impaction at other locations throughout the vessel. This will help to improve the CFD model by implementing location-specific adhesion and sticking coefficients. The iPWR vendor indicated that characterization of relative deposition quantities will help to develop post-accident clean-up strategies and plans. It should be noted that the current model is conservative because it is assumed that no particle sticking occurs. This is currently substantiated by an analysis of the impaction adhesion based on the Stokes number. Further assessments should include performing experiments to measure particle deposition at specific locations within the vessel.
- iv. **Assess the effects of non-uniform distribution of particles in the containment vessel (*recommended by NRC and iPWR vendor*):** Currently, particle concentrations are assumed to be uniformly distributed within the CV. This assumption significantly affects particle deposition efficiency. It is conceivable that the transient pressurization period may create an uneven distribution of particles. Current assumptions may be conservative, if this uneven distribution is such that the particle concentration is higher close to deposition surfaces. However, current assumptions may not be conservative, if the concentration is higher furthest from the deposition surfaces. Hence, an analysis of the sensitivity of the deposition rates to critical concentration scenarios will be beneficial. It should be noted that the current study assumes a homogenous concentration as required by the NRC guidelines.
- v. **Assess the effects of transient aerosol concentrations during pressurization (*recommended by iPWR vendor*):** This includes an analysis of the effects of various concentrations during the pressurization period. The effect of various pressurization rates is on the formation of aerosols, concentrations and particle size. This will allow application of the current study to a wider range of accident scenarios.
- vi. **Assess effects of vertical temperature gradients on the CV and RV walls (*recommendation by iPWR vendor*):** This is critical to identify potential limitations to the convective flow assumptions. Temperature variations along the RV and CV wall may affect convective flow velocities; however, in the current study, the wall temperatures had very little variation, thereby rendering its effects on convective flow to be uniform.
- vii. **Characterize the effects of a drop in containment vessel pressure (*recommendation by iPWR vendor*):** This may occur due to containment leakage, which may affect vessel pressure and assumptions around the performance of the deposition phenomena and the decontamination factors. This effort will also describe the significance of the regulatory requirement for assessment of containment leak rates in two time periods; before and after 24 hours.

- viii. **Characterize the effects of a sudden increase in pressure due to latent aerosol burst into the containment vessel (*recommendation by iPWR vendor*):** For the current study, it was assumed that aerosol deposition occurs after the pressurization period. Hence, for transients that have additional pressurization, this will affect the aerosol characteristics and may affect deposition rates. Specifically, it has been shown that pressure may affect the condensation rate and hence affect mechanisms such as diffusiophoresis.
- ix. **Assess the significance of an uninsulated vessel top relative to the experimental configuration and results (*recommendation by iPWR vendor*):** For iPWR designs that are uninsulated at the top of the vessel, what is the effect of this on current aerosol deposition assumptions?
- x. **Assess the effects of larger particles ($>10\text{ }\mu\text{m}$) on deposition rates (*recommendation by iPWR vendor*):** Establish if the presence of larger particles (even though they are beyond the respirable range) affects the deposition velocities and decontamination factors associated with the particles in the range of interest ($1\text{-}10\text{ }\mu\text{m}$). As an example, collisions between the larger and smaller particles may affect the assumptions associated with the assessment of the phenomena. This may include formation of kernels, agglomeration or applicability of the Knudsen number (particle size relative to free molecular path). It may also affect the Cunningham slip coefficient. The net effect may be that the particles act as though they are at a higher concentration. This is significant for validation of current assumptions around particle transport and application of the CFD drift-flux model. Smaller particles may agglomerate with larger particles and settle and may also slow down due to their interaction with larger particles, and hence be suspended for longer than assumed with the current CFD model. To address these questions, experiments should be conducted to determine particle size changes due to agglomeration and verification of assumptions around simulant behavior.

The Electric Power Research Institute, Inc. (EPRI, www.epri.com) conducts research and development relating to the generation, delivery and use of electricity for the benefit of the public. An independent, nonprofit organization, EPRI brings together its scientists and engineers as well as experts from academia and industry to help address challenges in electricity, including reliability, efficiency, affordability, health, safety and the environment. EPRI members represent 90% of the electric utility revenue in the United States with international participation in 35 countries. EPRI's principal offices and laboratories are located in Palo Alto, Calif.; Charlotte, N.C.; Knoxville, Tenn.; and Lenox, Mass.

Together...Shaping the Future of Electricity

Program:

Advanced Nuclear Technology

© 2018 Electric Power Research Institute (EPRI), Inc. All rights reserved. Electric Power Research Institute, EPRI, and TOGETHER...SHAPING THE FUTURE OF ELECTRICITY are registered service marks of the Electric Power Research Institute, Inc.

3002013032

Electric Power Research Institute

3420 Hillview Avenue, Palo Alto, California 94304-1338 • PO Box 10412, Palo Alto, California 94303-0813 USA
800.313.3774 • 650.855.2121 • askepri@epri.com • www.epri.com